University of Alberta

Abrasive Wear of Shovel Teeth in Oil Sand

by

Zhihan Lin

A thesis submitted to the Faculty of Graduate Studies and Research
in partial fulfillment of the requirements for the degree of

Master of Science

in

Mining Engineering

Department of Civil and Environmental Engineering

Spring 2014
Edmonton, Alberta

Abstract

In the oil sands industry alone a single ultra-class shovel tip can lose more than 35 kg of steel mass in one operating day. When the downtime to change a set of GET on a shovel is performed frequently, it can add up to significant loss in shovel availability, not to mention the loss of tip, adapter and shroud steel chunks that reappear in damaging crushers.

This work has developed a mean to predict the performance of shovel teeth based on the field data by the introduction of specific energy (*Es*) which is defined as the friction energy required to cause a unit volume loss of material (Nm/m^3). Results show that it is possible to predict the performance of shovel teeth through *Es*. It is also found that *Es* can be an index to quantify the resistance of metallic materials to abrasion in a specific abrasive condition.

Acknowledgements

I would like to extend my deep gratitude to Prof. Tim Grain Joseph, my supervisor, who has provided me with a research opportunity and given me patient guidance and great support. I would like to thank Prof. Joseph Szymanski for his help on my research.

I am grateful to have worked with every member of AEGIS research group who give me encouragement, assistance, and suggestions during the course of my research.

I acknowledge the University of Alberta and the Faculty of Civil and Environmental Engineering which provides me with the research assistantship as well as the financial support.

Finally thanks to my families who give me love and support.

Contents

List of Figures

List of Tables

List of Symbols

A	Particle size coefficient
A'	Availability
B	Specific energy coefficient
E	Friction energy
E_S	Specific energy
E_C	Friction energy per digging cycle per shovel tooth
F	Normal force
F_h	Hoist force
G_h	Weight of handle
G_b	Total eight of bucket and excavated ore
v	Velocity
v_t	Friction velocity
v_h	Hoist velocity
v_c	Crowd velocity
H	Hardness
L_f	Arm of hoist force
L_r	Arm of resistance
L_b	Arm of total weight of bucket and excavated ores
L_h	Arm of weight of handle
T_C	Duty cycle time
U	Utilization
V	Volume loss of materials
V/t	Volume loss rate
R	Total digging resistance

R_n	Normal resistance applied on blade
R_n'	Normal resistance applied on teeth surfaces
2θ	Angle of particle
μ	Friction coefficient
σ	Normal stress
τ	Shear stress
d_h	Horizontal displacement
ε_v	Volumetric strain
l_{Crowd}	Crowd length
l_{Hoist}	Hoist length
l_{Boom}	Boom length
ΔOPA	Insider triangle of dipper system
ψ	An inner angle of triangle ΔOPA
λ	An inner angle of triangle ΔOPA
ε	An inner angle of triangle ΔOPA
α	Pitch angle or attack angle
β	Handle angle
β_1	Digging angle
ε_1	Boom angle
ξ	Blade direction
δ	Lift angle
η	Hoist angle
λ_1	Cable angle
τ	Bucket angle
ψ_1	Angle between handle direction and axis of saddle

1 Introduction

1.1 Significance of Problem

Electric cable shovels are the most commonly used ultra-class scale earthmoving equipment in mining industry. In the Athabasca oil sand region of Northern Alberta, Canada, the application of cable shovels has been proven very successful. However, severe wear damage caused by interactions between shovel teeth and abrasive media leads to significant expense in equipment maintenance and a huge production loss. The study on abrasion is of a major interest for the mining industry; however most research concentrates on the theoretical analysis and establishment of micro-scale models which are difficult to validate for engineering purposes. Some research aims to improve wear resistance of materials by means of chemical technologies, which is time consuming and cost intensive. A simple but practical method to facilitate selection of materials to match actual abrasive conditions encountered in the field may result in greater performance improvements of ground engaging tools with little investment.

1.2 Objectives

The goal of this thesis is to study the abrasive wear of ground engaging tools, predict performance of shovel teeth, and make it possible to facilitate selection of materials to match actual abrasive conditions. In reaching this goal, following approaches were targeted involved:

1. Develop an understanding of abrasive mechanisms.
2. Develop a methodology to calculate digging resistance and digging velocities based on field data;
3. Design a scaled abrasion test to measure specific energy of materials.

4. Link digging resistance and digging velocities to volume loss of shovel teeth through specific energy.

2 Literature Review

2.1 An Overview of Cable Shovels

2.1.1 Introduction

The electric cable shovel is one of the most commonly used earthmoving machines with high production but low unit cost. Its production capacity is in the range of 54 to 110 tonnes, much higher than other excavators such as hydraulic shovels or large-wheel loaders (Hrebar, 1997). Compared to other excavation systems, the combination of cable shovels and truck haulers has been extensively employed in oil sand due to its high flexibility and reliability.

2.1.2 Mechanical feature of cable shovels

The P&H 4100 Boss cable shovel is specifically designed to operate in oil sand environment, and it is the case study of abrasive wear on shovel teeth in this thesis. Figure 2-1 shows the schematics of P&H 4100 Boss cable shovel and its terminology is given in Table 2-1.

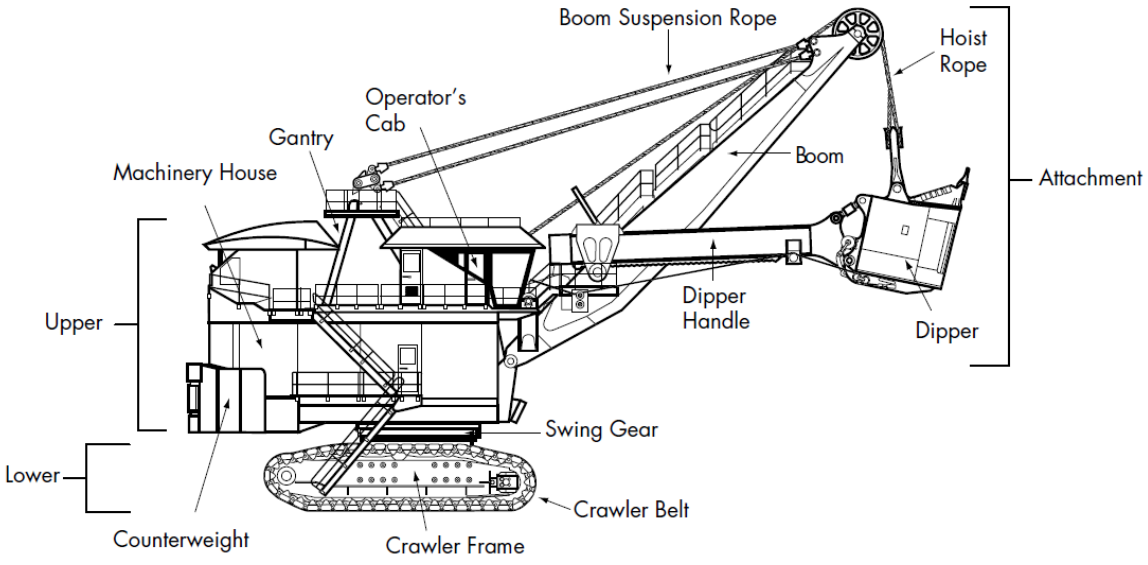

Figure 2-1: Schematics of P&H 4100 Boss cable shovel (after Darling, 2011)

Table 2-1: Components of a cable shovel

Assemble	Component	Function
Lower	Crawler Frame and Crawler Belt	Bolt or weld to carbody and used for propelling.
	Swing Gears	Transmit power for swinging.
Upper	Machinery House	Equipped with electric drive motors to provide power.
	Counterweight	Balance the weight of attachment assembles
	Gantry and Suspension Rope	Hold the boom in position
Attachment	Boom	Remain stationary to support dipper and handle
	Hoist Cable	Lift or lower dipper
	Dipper Handle	Retract or extend the dipper to dig
	Dipper	Load or dump

2.1.3 Operation of cable shovels

The primary motions of a cable shovel include: propel, hoist, crowd, and swing, which is summarized as follows:

- Propel motion: to drive the cable shovel forward or backward until an appropriate distance from digging face.

- Hoist motion: to provide sufficient power to pull up the dipper through the digging face.

- Crowd motion: to position the dipper into the bank.

- Swing motion: to drive the upper works, revolving the dipper position for dumping or digging.

A typical duty cycle for a cable shovels involves digging, swinging, dumping, and returning, where the dig cycle includes positioning the digging tools in the face, penetrating, cutting, and then lifting to clear the bank (Frimpong, 2005).

2.1.4 Performance monitoring of cable shovels

The performance of a cable shovel is a primary concern in the understanding of its reliability, productivity, and effectiveness. The study on shovel performance monitoring has been carried out. Yin *et al* (2007) who measured the in-situ strains and displacements

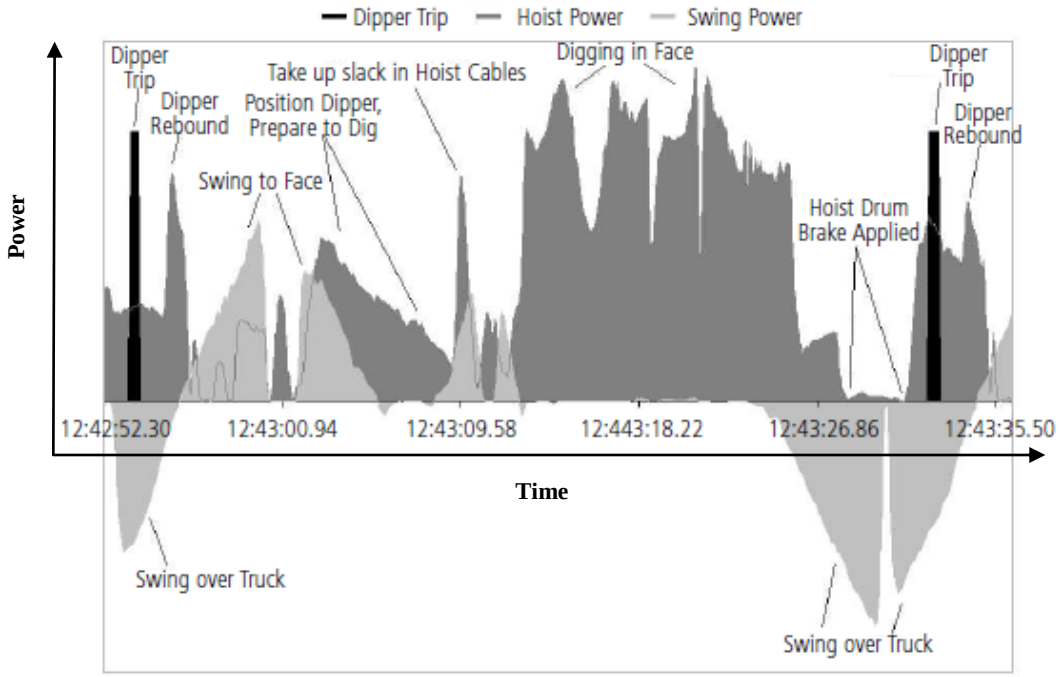

Figure 2-2: Cable shovel single duty cycle (after Joseph and Hansen, 2002)

of a boom to predict its fatigue life. Patnayak and Tannant (2005) collected current and voltage data from hoist, crowd, and swing motors of P&H 4100 series cable shovels, and they found that ground diggability could be assessed by average hoist power; and the shovel operators rather than arbitrary temperature on the digging medium had significant influence on hoist power consumption and shovel performance. Through analysis of variation of swing and hoist power consumption, Joseph and Hansen (2002) determined and explained a single duty cycle, aslo introduced the phenomena of dipper rebound (Figure 2-2). The dipper rebound is caused by face resistance release of the dipper on exiting from the dipper cycle.

2.1.5 Force analysis of cable shovels

The force required to complete an excavation is of major interest for the design and performance of cable shovels. Joseph and Shi (2012) have given a general dipper-handle force analysis (Figure 2-3).

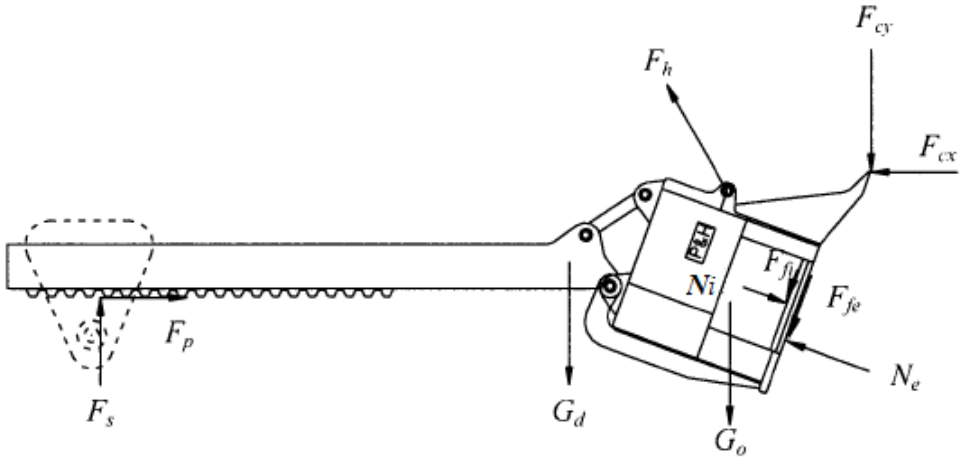

Figure 2-3: Dipper-hander free body diagram (after Joseph and Shi, 2012)

There are ten forces considered here: the support force for dipper (F_s); the crowd force generated from crowd motor (F_p); the gravity of the whole dipper comprised of handle

and bucket (G_d); the weight of materials excavated in bucket (G_o); the hoist force generated by hoist motor for lifting the bucket (F_h); the components of the cutting resistance in the x and y directions (F_{cx} and F_{cy}); the normal force (N_i) and its friction (F_{fi}) caused by materials moving above the internal dipper wall, and the normal force applying on the external front dipper wall (N_e) and its frictional force (F_{fe}).

Of these forces, F_{cx}, F_{cy}, N_e, and F_{fe} are the components of total digging resistance (R) which is equivalent to the digging effort, while N_i and F_{fi} are caused by excavated material moving against the inside of dipper front wall. The digging resistance (R) is reasonably considered to act on the tooth surface since the variation of the point of action is small. The magnitude of N_i and F_{fi} are much less than that of digging resistance and they can be zero if the bucket does not directly push into the materials or there is no compacting action (Hemami, 1994). The simplified dipper-handle force analysis is shown in Figure 2-4.

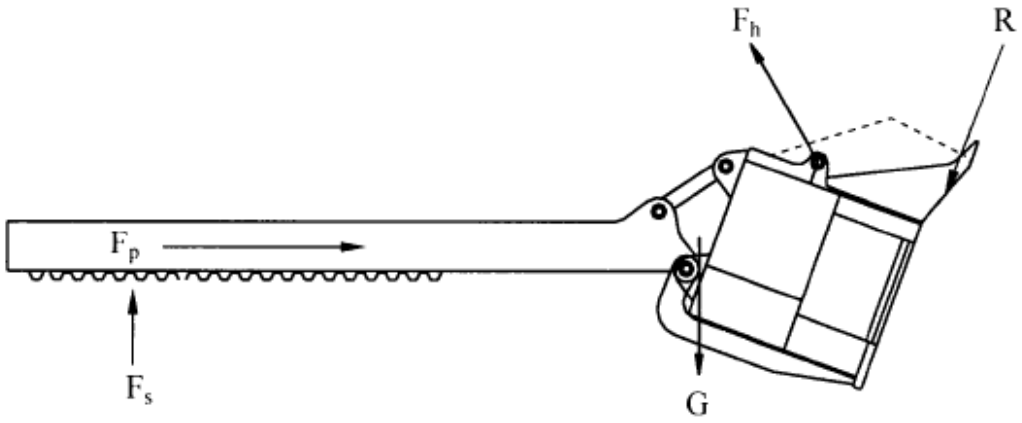

Figure 2-4: Simplified dipper-handle free body diagram (after Joseph and Shi, 2012)

The digging resistive force is a result of the interaction between ground engaging tools (shovel teeth) and the ground. It is this huge digging resistance with the same order of magnitude as the hoist force that gives rise to severe wear damages on the shovel teeth or

even the dipper. To ensure the reliable operation of cable shovels, the shovel teeth have to be replaced at intervals. However, until now there is not yet an effective method to schedule or predict replacement of ground engaging tools which results in unplanned downtime of the cable shovel and reduction of its availability.

2.2 Ground Engaging Tools

2.2.1 Introduction

Ground engaging tools refer to components of equipment directly interacting with ground. They are designed as sacrificial items which are installed on the front of buckets so as to prevent the other more expensive structural components from wear failure. Shovel teeth are typical ground engaging tools. The design of shovel teeth not only improves dipper maintenance but also allows buckets easily to penetrate, cut, and excavate overburden or minerals.

2.2.2 Shovel teeth

A shovel tooth system is shown in Figure 2-5.

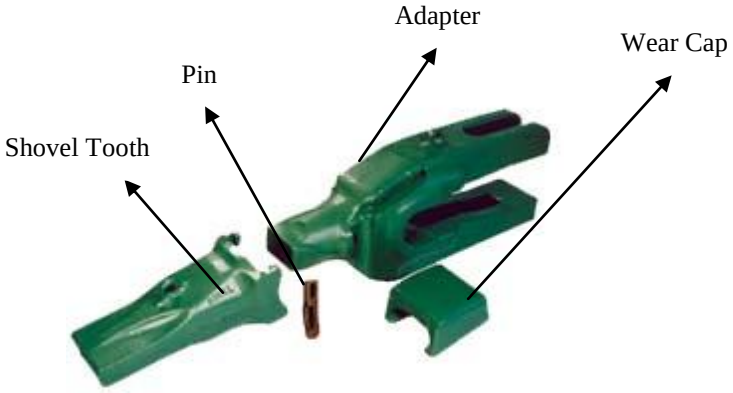

Figure 2-5: Shovel tooth system for cable shovels (Esco Corporation, 2013)

The nomenclature of shovel teeth systems are summarized in Table 2-2.

Table 2-2: Nomenclature of shovel tooth system

Parts	Function
Shovel Teeth	Interacting with ground and protecting of other expensive components
Adapter	Connecting shovel teeth and lip systems
Pin	Fixing connection between adapter and shovel teeth
Wear Cap	Protecting adapters and pins

2.2.3 Tooth-ground interaction

2.2.3.1 Earthmoving action

The earthmoving process of a cable shovel consists of continuous interaction between a shovel tooth and the working environment. Generally it can be divided into three actions: penetration, cutting, and excavation (Figure 2-6).

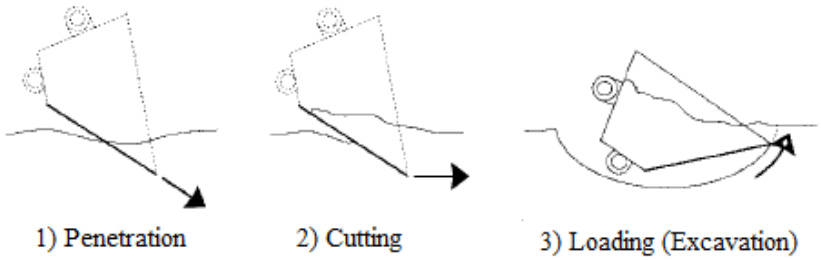

Figure 2-6: Fundamental earthmoving actions (after Blouin, 2001)

Penetration is the action of pushing a single solid blade into a medium with a fixed orientation. Cutting is defined as a lateral motion made by an inclined blade at a constant rake angle. Although penetration and cutting are distinct actions, the resistive force observed during cutting are the same nature as those encountered while in penetration (Zelenin *et al.*, 1985). Therefore the cutting resistance in practice can be measured by a

penetrating device. In terms of excavation, as an example, it may be defined as the loading task for a broken medium, and it can be considered as a combination of penetration and cutting (Stephane *et al*, 2001).

2.2.3.2 Models for tooth-ground interactions

The study of interaction between ground engaging tools and ground material has been extensively carried out major interest in estimating the cutting force required to cause ground excavation. Even though digging is a dynamic process, most of models are established based on a static analysis due to the effect of large retaining walls making the influence of acceleration forces too small to ignore (Stephane *et al.*, 2001). The failure surface caused by a digging force is usually considered as a logarithmic shape. However, for the sake of simplicity the flat shape is commonly adopted to approximate the logarithmic shape (Figure 2-7), where a trial wedge theory based on the flat failure plane has been established.

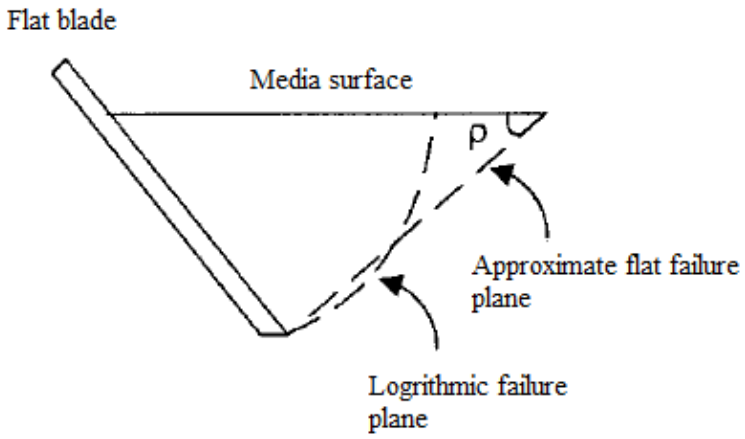

Figure 2-7: Cutting failure planes (after Osman, 1964)

A static equilibrium model is given by McKyes (1985) with advantages of versatility and robustness (Figure 2-8).

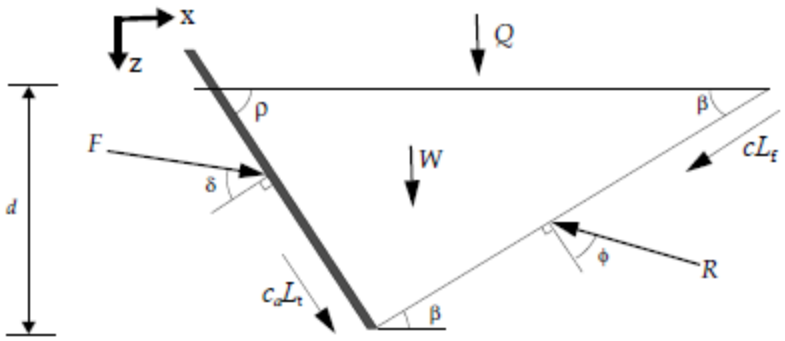

Figure 2-8: Static equilibrium model (after McKyes, 1985)

Parameters shown in Figure 2-8 are summarized as follows: *w*-blade width; *d*-the depth of penetration; ρ-cutting angle; β-shear plane angle; δ-external friction angle; ϕ-internal friction angle; *C*-cohesion; *Ca*-adhesion; *F*-digging force; *W*-weight; *Q*-surcharge; *Lt*-blade length penetrating the ground; *Lf* -ground failure surface length. The cutting force in this model is expressed as:

$$F = w(rgd^2 N_r + cdN_c + C_a dN_{ca} + qdN_q + rv^2 dN_a) \quad \textbf{(2-1)}$$

In equation (2-1) *r*,*g*, and *v* are density, gravity, and velocity; whereas N_r,,N_a, N_q, N_{ca}, and N_c stand for the coefficients of weight, inertia, surcharge, adhesion, and cohesion respectively. There coefficients are given from equations (2-2) to (2-6):

$$N_r = \frac{\cot\rho + \cot\beta}{2((\cos(\rho+\delta) + \sin(\rho+\delta)\cot(\rho+\phi))} \quad \textbf{(2-2)}$$

$$N_a = \frac{\tan\beta + \cot(\beta+\phi)}{(\cos(\rho+\delta) + \sin(\rho+\delta)\cot(\beta+\phi))\cdot(1+\tan\beta\cot\rho)} \quad \textbf{(2-3)}$$

$$N_q = \frac{\cot\beta + \cot\rho}{\cos(\rho+\delta) + \sin(\rho+\delta)\cot(\beta+\phi)} \quad \textbf{(2-4)}$$

$$N_{ca} = \frac{1 - \cot(\beta+\phi)\cot\rho}{\cos(\rho+\delta) + \sin(\rho+\delta)\cot(\beta+\phi)} \quad \textbf{(2-5)}$$

$$N_c = \frac{1+\cot(\beta+\phi)\cot\beta}{\cos(\rho+\delta)+\sin(\rho+\delta)\cot(\beta+\phi)} \qquad \textbf{(2-6)}$$

Frimpong and Hu (2004) have reformulated this model to simulate shovel-oil sands interaction during excavation. The simulation results show that a change in frictional angle and digging depth can influent the shovel performance significantly, while the bucket velocity has a negligible effect.

Even though a static equilibrium model is a universal earth-moving model, it is not always valid for surface mining because it is based on the assumption that the media profile is horizontal and a surcharge pressure exists all the time. Joseph and Shi (2012) revised this model by introducing a ground failure slope (χ) and blade direction (ξ), making it possible to calculate the cutting force as well as resistance appied on teeth for each bucket sweeping step (Figure 2-9).

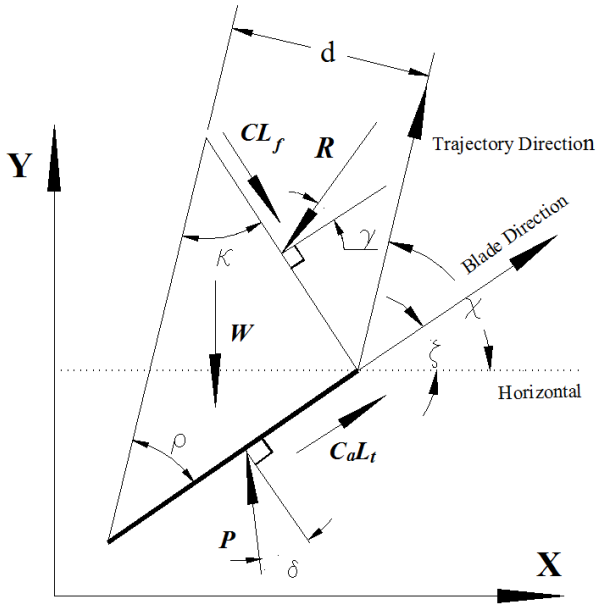

Figure 2-9: Modified static equilibrium approach as an approximation for the failure surface (after Joseph and Shi, 2012)

The force equilibrium equations for a blade of unit width can be written by:

$$\sum f_x = 0$$
$$P\sin(\rho+\delta-\chi)+C_aL_t\cos(\rho-\kappa)-R_f\sin(\kappa+\varphi+\chi)-CL_f\cos(\kappa+\chi)=0 \quad \textbf{(2-7)}$$

$$\sum f_y = 0$$
$$P\cos(\rho+\delta-\chi)-C_aL_t\sin(\rho-\kappa)-R_f\cos(\kappa+\varphi+\chi)-CL_f\sin(\kappa+\chi)=0 \quad \textbf{(2-8)}$$

Solving for digging effort *P* for the blade with width *w:*

$$P=\frac{w\cdot[W+(1)+(2)]}{\cos(\rho+\delta-\chi)+\sin(\rho+\delta-\chi)\cdot\cot(\kappa+\varphi+\chi)} \quad \textbf{(2-9)}$$

Where:

$$(1)=\frac{Cd[\sin(\kappa+\chi)+\cos(\kappa+\chi)\cdot\cot(\kappa+\chi+\varphi)]}{\sin\kappa} \quad \textbf{(2-10)}$$

$$(2)=\frac{C_ad[\sin(\rho+\chi)-\cos(\rho-\chi)\cdot\cot(\kappa+\chi+\varphi)]}{\sin\rho} \quad \textbf{(2-11)}$$

The total digging effort *P* is equivalent to the total digging resistance *R*:

$$R=-P \quad \textbf{(2-12)}$$

When the digging effort *P* is predicted through (2-9), the digging effort is also obtained. Compared to the static equilibrium model, the revised model is more applicable for simulation of force constrains while a cable shovel is excavating.

2.3 Oil Sand

Oil sands are complicated mixtures of quartz, bitumen, and water. 99% of quartz grains in oil sand are watered, where the bitumen occupied the interstitial space and allow a water

phase forming a film around the grains. These quartz sands are dense with large contacts between each other. The physcial preperties of oil sand are given in Table 2-3. It is interesting that oil sand displays high shear strength but minor cohesion, which means there is no adhesion damage on ground engaging tools. Particles of quartz account for 80% to 98% of the total solids in oil sands and they are the predominant abrasive and erosive media (Llewellyn, 1997). These particles are hard with various size and shape. In the case of cable shovels working on oil sands, their ground engaging tools are mainly subjected to severe abrasvie wear damages caused by these hard quartz particles.

Table 2-3: Physical properties of oil sands (after Dusseault and Morgenstern, 1978)

In situ density	2.09 – 2.42 t/m^3
Mineralogy (For arenaceous strata)	90-98% quartz; 1-5% feldspar; 0-3% muscovite; 0-4% clay minerals; <1% accessory minerals
Grain shapes	coarse- and medium-grained sands; well-rounded to sub-angular fine-grained sands and silts;
Approximate bitumen content ranges	0-1% in clay shale and clayey silts; 0-10% in sandy silts and silty sands; 8-16% in fine- to medium-grained sands; 12-16% coarse-grained sands;
Oil sands cohesion	0
Oil sands- GET adhesion	0
Internal friction angle	22^o – 40^o

2.4 Wear

2.4.1 Introduction

Wear is defined as a mass-loss process occurring on the surface of materials that has been a serious problem in the surface mining industry. It results from the interaction between

materials and excavated environments in the form of physical separation, chemical dissolution, or melting at the contact interface. Wear damages will destroy material properties, reduce operating efficiency, and increase maintenance expense (Eyre, 1976). Jeffery and Wilson (2001) state that the cost of corrosion and failure of materials is equal to about 4% of a country's gross national product (GNP). When the equipment is subjected to severe wear, it cannot be maintained in a timely fashion, and it is most likely to cause potential engineering risks inducing safety of personnel.

2.4.2 Wear in the mining industry

The mining industry spends billions of dollars each year on maintenance of mining equipment and invests more each year in research on wear protection to extend the life of such components or machines. Wear in mining operations are caused by severe interactions between the surface of equipment and minerals, or wastes, which result in a large cost for maintenance incurred through repair or replacement of damaged components. According to a National Research Council Canada Report published in 1986, it was conservatively estimated that cost of wear damage and friction in the Canadian mining industry is around $940 M (Llewellyn, 1996), where this cost is now approximately $3.5B. Wear attacks can be categorized into four modes: abrasion, metal-to-metal wear (adhesion), erosion, and corrosion (McKee, 1997; Hawk and Wilson, 2000). These wear modes do not occur singly or independently, by contrast they act synergistically with each other and sometimes change from one to another.

- Abrasion

Abrasion is the predominant wear mode existing in earthmoving, mining, and mineral processing. It occurs when hard particles deform or penetrate soft material surfaces and then via sliding a distance over the surface under a level of stress. Belt, conveyors,

crushers, and feeder breakers are subjected to severe abrasion. This thesis focuses on the abrasive wear that occurs on shovel teeth, such that the more specific knowledge of abrasion will be discussed in section 2.4.3.

- Metal-metal wear (adhesion)

Metal-metal wear is also seen as adhesion. When a contact stress exceeds a certain threshold value, metal surfaces will be bonded to each other, viz a viz cold welds. These bonded parts are broken by a sufficient tangential force, creating mass loss of materials.

- Erosion

Erosion is caused when either a dense concentration of solid particles carried in a flowing fluids or liquid droplets repeatedly impacts and slides against a material surface at high velocity (Llewellyn. 1997). Low-angle particles are most likely to slide on the surface, whereas high-angle probably creates impacts. Erosion exists in aqueous slurry transportation, centrifuges used for mineral separation, and systems handling streams in upgrading operations.

- Corrosion

Corrosion results from chemical reactions happened on the exposure of fresh metal surfaces under the high pressure or flash temperatures (Murray, 1988). In the mining and processing industry, there exist many types: crevice corrosion, galvanic corrosion, pitting, oxidation, sulphidation, hydrogen embrittlement, and so forth (McKee, 1997).

Apart from these four commonly encountered wear modes, fatigue and fretting also cause significant reduction in material properties or even catastrophic failure.

- Fatigue

Fatigue is encountered in materials subjected to the cyclic oscillating stresses which result in initiation and propagation of sub-surface fractures. Heavy mining equipment suffers from the chronic fatigues.

- Fretting

Fretting is a special type of fatigue wear caused by cyclic reciprocating slips of small amplitude between surfaces. Owing to fretting wear, debris will be created, trapped into contact areas, and dam lubricant follow, leading to severe abrasion or fatigue (Murray, 1988).

2.4.3 Abrasive wear

Abrasion is the most common forms of wear attack in earthmoving, mining, and mineral processing equipment. In terms of cable shovels, the ground engaging tools are subjected to severe abrasion caused by interaction between shovel teeth and ground.

2.4.3.1 Abrasive mode

Abrasion is a physical process and it is defined as removal of materials from the abraded material surface. In detail, when hard particles contact with the soft materials, hard particles will penetrate the soft material surfaces under the pressure, leading to the plastic deformation. This deformation, coupled with sliding motion, will make the particles cut the soft surface and result in material removal. Abrasion can be classified as being low-stress abrasion, high-stress abrasion, and gouging abrasion according to the degree of severity as illustrated in Figure 2-10 (Olson and Cross, 1992; Norman, 1980; Hawk and Wilson, 2000).

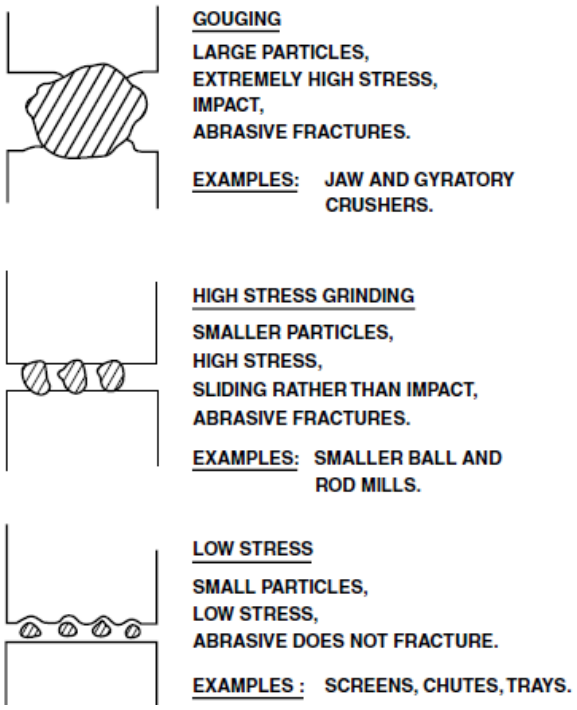

Figure 2-10: Schematic representation of abrasive wear classification (after Hawk and Wilson, 2000)

- Low-stress abrasion

Low-stress abrasion is also referred to as scratching abrasion. It occurs when abrasive particles pass over a surface with relatively low contact stress, during which particles always remain substantially intact. Materials are generally removed from the wearing surface by micro-cutting action. Low-stress abrasion is not accompanied by significant impacts.

- High-stress abrasion

High stress abrasion is also called as grinding abraison. It occurs when abrasive particles are trapped and crushed between two hard solid materials. High contact pressures leads to the fragmentation and pulverization of abrasive particles as well as deformation and spalling of the wearing surface.

- Gouging abrasion

Gouging abrasion is encountered under conditions where abrasive lumps are driven into a surface under high stress level and then ploughing out material surfaces in the form of plastic flows. Gouging abrasion involves two failure types: cutting and tearing. In either cutting or tearing, the motion of the sharp points of rocks or other hard abrasive lumps will remove chips of metal from the wearing surface under considerable pressure, which is similar to the machining process (Hawk and Wilson, 2000). Such high pressure also breaks abrasive lumps. Toughness is the primary requirement for gouging-resistance materials.

These three forms of abrasion are all encountered on ground engaging tools. Generally, shovel teeth are subjected to low-stress abrasion in soft and unblasted materials like oil sands, whereas high-stress or gouging abrasion may be also present for hard and blasted minerals.

2.4.3.2 Abrasive mechanism

The introduction of abrasive mechanisms is helpful to illustrate the interactive nature of force between abrasives and materials. Zum (1988) divided abrasive mechanisms into four types: microploughing, microcutting, microcracking, and microfatigue (Figure 2-11).

- Microploughing and microfatigue

Microploughing is characterized by formation of grooves. Materials will be displaced to the sides, which forms closed ridges to the sides of grooves, rather than be directly removed from the wearing surface. Microploughing is caused by a single passage of one abrasive particle without detachments of materials. When particles repeatedly plough surfaces, materials may break off by mircrofatigue.

- Microcutting

Microcutting is characterized by direct removal of material in the form of debris or chips without formation of ridges on the sides of grooves. In ideal cases, the volume loss by chips or debris is equivalent to the volume of the grooves. This mechanism is similar to conventional machining and always occurs on medium-soft materials.

- Microcracking

Microcracking is characterized by occurrence of cracks formation and propagation in brittle materials. When highly localized stresses are applied on brittle surfaces through the action of abrasive particles, fractures will occur and then propagate until large debris have spalled from worn surfaces.

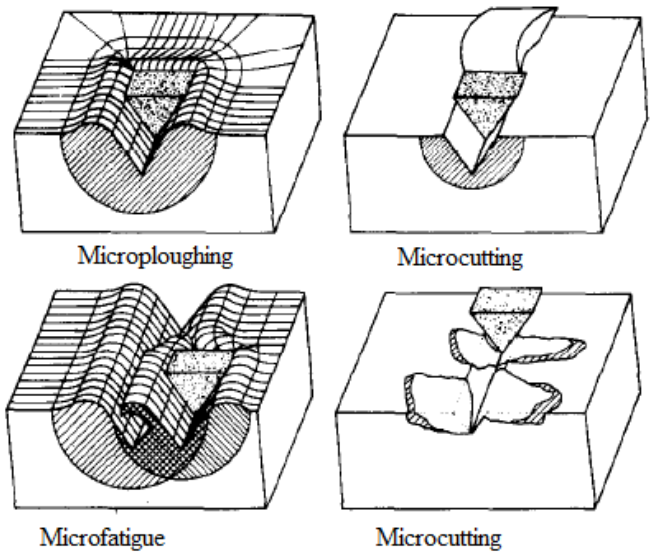

Figure 2-11: Physical interactions between abrasive particles and material surfaces (after Zum, 1988)

Summarily, microploghing, microfatigue, and microcutting are commonly encountered in soft but ductile materials like metals, while microcracking usually happens on hard but brittle ceramics or concretes.

2.4.4 Abrasive control

Abrasive wear is not only related to chemical and physical properties of materials but also to the particle-material tribosystem. The abrasion coefficient K_{ab} used for description of wear rates is not constant and it can vary between 10^{-4} to 10^{-1} depending on the tribosystem and material parameters (Rabinowicz, 1980). Generally there are three factors determining the degree of abrasion: material hardness, particle characteristics, and contact stress.

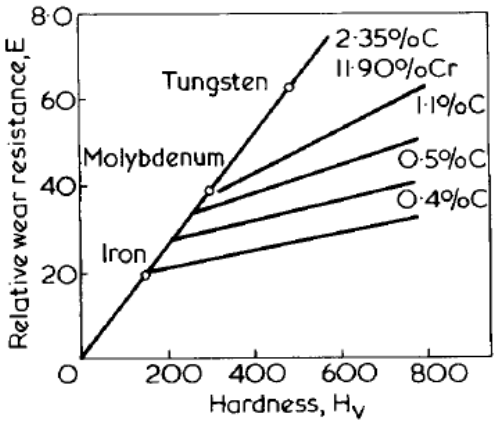

Figure 2-12: Resistance to abrasive wear is a function of hardness (after Eyre, 1976)

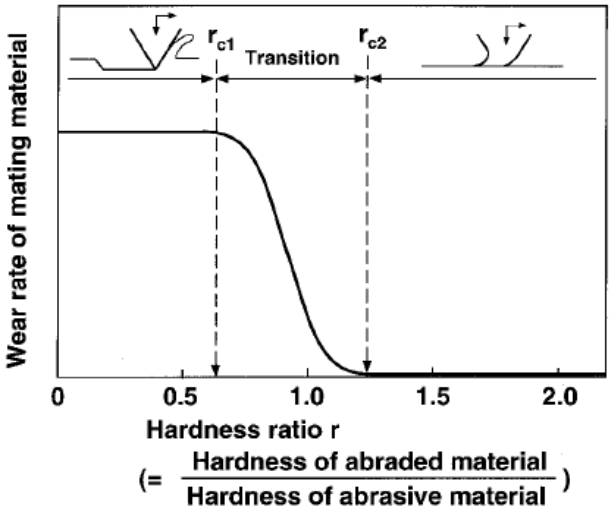

Figure 2-13: Schematic diagram of effect of hardness ratio on wear rate of abrade material against abrasives (after Kato and Adachi, 2000)

- Hardness

Material hardness is the most critical factor determining the degree of wear damage. Eyre (1976) indicated that the relative wear resistance of metals or metallic compounds was roughly proportional to their own hardness (Figure 2-12). Kato and Adachi (2000) have studied the influence of hardness ratio of materials to abrasives on wear rates of abraded material against abrasives (Figure 2-13).

From Figure 2-13, it can be seen that the hardness ratio, r, has significant influence on wear rates. When the ratio is less than a certain critical value of r_{c1}, there exist severe wear damages on mating materials. However with the increase in hardness, the ratio wear rate will decrease sharply, and finally reach to the lowest level or even no observation of abrasive wear when r is beyond the upper critical value r_{c2}. Eyre (1976) indicated that it was unnecessary to increase hardness of materials when the value of r_{c2} is over 1.3 since no remarkable improvement of abrasive resistance. The wear-hardness behaviour is attributed to transitions of contact mechanisms related to hardness ratio. When material hardness is larger than the abrasive, the deformation of materials prefers to the elastic rather than plastic, thereby reducing wear rates. By contrast the plastic deformation is more likely to occur when materials are softer than abrasives. This relationship between hardness and wear confirms that metal-matrix-composites consisted of very hard second-phase matters that give superior wear resistance performance compared to nominally pure metals (Gore and Gates, 1997). Currently, the main method to control abrasive wear is to improve hardness of materials through surface modification or altering microstructure.

- Abrasive particle characteristics

Abrasive particles are characterized by shape and size. Changes on either particle shape or size will result in different wear rates of materials. In terms of particle size, small

abrasives create elastic deformation, while large abrasives create plastic deformation, since large contact forces can be applied on surfaces through large abrasives. Additionally large particles are supposed to slide longer distances over abraded surfaces than small ones. Typically, most abrasive wear is caused by particles with size from 5 μm and 500 μm (Thakare and Wharton, 2012). Misra and Finnie (1981) illustrated that wear volumes go up sharply with an increase in abrasive size up to 100 μm, after which wear losses still rise but at slower rates.

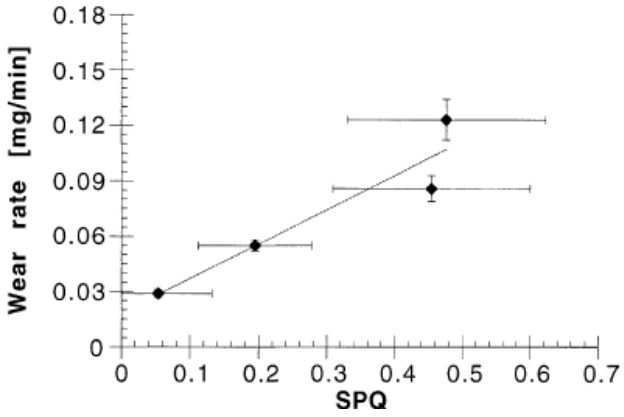

Figure 2-14: Average wear rates of mild steels vs. average SPQ values of abrasive particles (after Stachowiak and Stachowiak, 2001).

Particle shapes can be described as round, semi-round, semi-angular, and angular. It is obvious that abrasives of high angularity can indent or penetrate into materials deeper, resulting in larger removal of materials from the wearing surface. Stachowiak and Stachowiak (2001) quantified particle angularities by introducing a parameter *SPQ* (spike parameter quadratic fit) and gave the relationship between wear rates and abrasive angularities (Figure 2-14). The principle of *SPQ* is to use a set of triangles constructed at different scales to represent spikes protruding outside the circle centred on the abrasive particle's centroid. The higher the *SPQ* value is, the sharper the abrasive is. Clearly the wear rate increases with the growth of particle angularities.

- Contact stress

The high contact stress leads to severe abrasive wear through increasing the penetration depth in material surfaces. With the increase in contact stress, there exists a rising tendency for fragmentation of abrasives, generating new particles with fresh and sharp cutting edges (Gate and Gore, 2007). Additionally particles are most likely to slide rather than rotate over material surfaces under high levels of contact stress.

Summarily, abrasive wear is a complicated physical process influenced by the hardness ratio of materials to abrasive particles, abrasive particle shape, abrasive particle size, and contact stress. The abrasive control can be achieved by the means of not only increasing material hardness but also improving the contact conditions between materials and abrasives.

2.4.5 Abrasive failure of shovel teeth

In the mining industry, ground engaging tools are subjected to heavy abrasive damages due to the severe interactions between teeth and ground. The occurrence of abrasive wear on shovel teeth not only reduces a shovel's operating efficiency, but also leads to significant production loss due to unplanned maintenance. Knights (2009) showed that a set of nine teeth was only worth US$ 2700, but the average production lost caused by an unplanned change-out of a tooth set was US$ 38,368, nearly fifteenth times the cost of the teeth.

Generally, teeth failure can be classified into three types: broken failure, surface failure, and bottom failure (Olson and Cross, 1992). Failure types are related to the hardfacing area of the shovel teeth. When hardfacing areas are located on both top and bottom faces of the tooth, broken is most likely to occur (Figure 2-15(a)). Surface failure is commonly

encountered in a condition where only bottom of a tooth is covered by hardfacing deposits (Figure 2-15(b)). These two failure types are unacceptable in practice and they are not recommended in practice. By contrast the appropriate hardfacing area is considered on the top of a tooth, which would result in a self-sharp effect when the bottom failure occurs (Figure 2-15(c)).

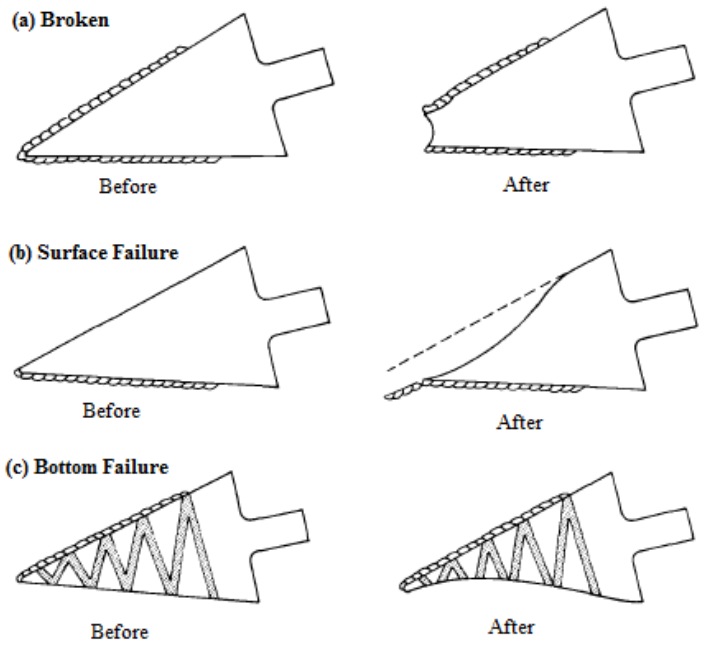

Figure 2-15: Schematic representation of the three teeth failure classification (after Olson, 1992)

2.4.6 Protection for shovel teeth

Even though properties of materials such as toughness, ease of fabrication, and weldability have influence on the performance of ground engaging tools, hardness is the most significant factors to be considered (Llewellyn, 1997). In an effort to increase abrasive resistance of shovel teeth, martensitic steel castings are suggested as the substrate materials, while hardfacing deposits are employed as protective system coatings on the substrate surfaces.

- Substrate materials

Martensitic steel castings have a unique combination of relative high hardness, good toughness, and ease of fabrication; thereby providing an appropriate substrate material for a shovel tooth. Martensitic steels belong to the medium carbon material class of steels with up to 4% alloy (Llewellyn, 1996). Depending on digging situation, various combinations of toughness, hardness, weldability, and strength of martensitic steels can be achieved through metallurgical techniques such as alloying and heat treatment. Hardness falls in the range of 243 HV to 560 HV, which is however much lower than quartz at 850 -900 HV. Since quartz sands are the dominant abrasive constituents in oil sands, hardfacing would be applied to enhance wear resistance, and to meet the hardness requirement in practice.

Another substrate material is martensitic steel forgings, whose surface has been hardened through quenching, tempering, or other metallurgical techniques, with hardness ranges from 363 HV to 577 HV. Hardfacing may be applied based on actual requirements of hardness, although in GET practice this is unlikely as most operations do not know what hardness material is required.

- Surface modification

Surface modification is a metallurgical process to deposit extremely wear-resistance material which cannot be reliably cast or forged on the substrate but have good toughness and low hardness. With regard to shovel teeth, one of the most widely used techniques is hardfacing welding deposition (Figure 2-15). Hardfacing has many advantages; including a wide ranges of welding consumables, in-situ repairs, and coatings with corrosion resistance. However, its major drawbacks include the possible occurrence of cracking

especially on thick deposits, and influence of high welding temperatures on the microstructure of substrates (Murray, 1988).

The hardness of welding deposits ranges between 513 and 800 HV. Chromium carbide or chrome white irons are the most common hardfacing welding consumables (Olson and Cross, 1992; Llewellyn, 1996). Another new consumable are tungsten carbide-based materials, which contain up 75% tungsten carbide particles. Tungsten carbides have extreme hardness (1900 HV), and can provide extreme abrasion resistance for shovel teeth.

2.5 Abrasion Modeling and Tests

2.5.1 Introduction

Abrasive prediction attracts a wide industrial interest, since it can be helpful to improve equipment reliability by selection of suitable materials for specific wear conditions; and to decrease production losses through planning and scheduling replacement of worn components. The study of wear prediction involves two major aspects: abrasion modeling and abrasion tests. Currently, there are many models proposed to simulate friction and abrasive wear, such as slip line theory, upper-bond methods, micro-scale dynamic models, analytical approaches, and so forth. This chapter discusses the micro-scale dynamic model as it has been recently developed for the gap in micro-scale abrasion model. In terms of abrasion tests, the jaw-crush test and dry sand rubber-wheel abrasion test are used since such results are easily measured for abrasive wear of shovel teeth.

2.5.2 Micro-scale Dynamic Model

The micro-scale dynamic model is a computational approach developed by Li *et al* (1999) to simulate wear processes as well as to predict material performance.

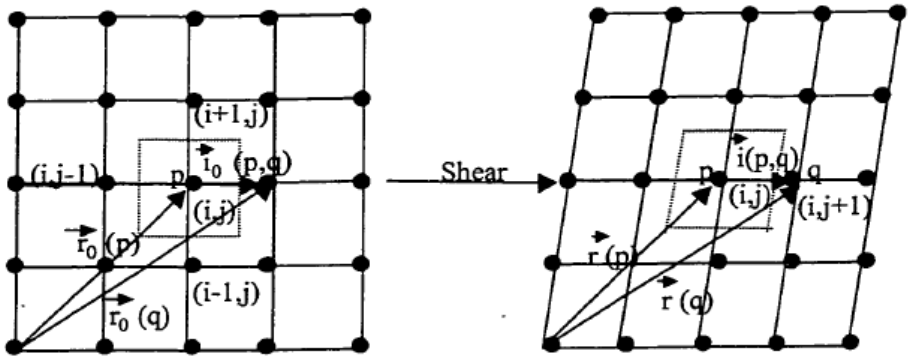

Figure 2-16: Illustration of the micro-scale dynamic model (after Li *et al.*, 1999).

The model is established in two-dimensional space (Figure 2-16). A given material is discretized using a square lattice, and each site represents a small volume of the material. When the material is subjected to abrasive wear under an external force, each lattice site may move. This movement is decided by the interaction between each pair of adjacent sites which is dependent on the mechanical properties of materials such as elastic modulus, yield strength, and tensile strength. In other words, the metallic material is imagined to be a set of semi-infinite micro-scale lattices, and the wear processes are the resultant of interaction between adjacent lattice sites and their corresponding movements.

The interaction between adjacent lattice sites under application of an external force is given by:

$$\begin{cases} \vec{F}_p = \sum_{q}^{n} k\Delta\vec{l}(p,q) + \vec{f}_p \\ \Delta\vec{l}(p,q) = \vec{l}(p,q) - \vec{l}_0(p,q) = [\vec{r}(q) - \vec{r}(p)] - \vec{l}_0(p,q) \end{cases} \quad \textbf{(2-13)}$$

$\vec{F}_p$ is the sum of the forces, which leads to deformations of bonds between the site *p* and its all adjacent sites. The deformation of each lattice is noted by $\Delta\vec{l}(p,q)$, and the

magnitude of each force is proportional to $\Delta \vec{l}(p,q)$ via a coefficient *k*. When the site *p* is on the surface, the external force $\vec{f}_p$ is taken into consideration. The movement of a lattice site under interaction between the site and its adjacent sites is expressed as:

$$\begin{cases} \vec{V}_{t+\Delta t}(p) = \vec{V}_t(p) + \dfrac{1}{m}\vec{F}_t(p) \bullet \Delta t \\ \vec{r}_{t+\Delta t}(p) = \vec{r}_t(p) + \dfrac{1}{2}[\vec{V}_{t+\Delta t}(p) + \vec{V}_t(p)] \bullet \Delta t \end{cases} \quad \textbf{(2-14)}$$

$\vec{V}_t(p)$ and $\vec{V}_{t+\Delta t}(p)$ represent velocities of site *p* at time *t* and time $t+\Delta t$ respectively, while $\vec{r}_t$ and $\vec{r}_{t+\Delta t}$ are positions of site p at time t and time $t+\Delta t$ individually. In such a way, the position of any lattice sit could be determined at any time. When the deformation of a bond is over a critical strain value, the bond is broken. If all bonds between one site and its adjacent sites are broken, this site will be worn away. Finally, the wear loss can be estimated by counting the total number of worn out site. However, as this research will focus on a scaled G65 test, this dynamic models will not be used here.

2.5.3 Jaw Crusher Gouging Abrasion Test

The jaw crushing gouging abrasion test is a recently developed test to simulate the gouging abrasion characterized by significant removals of wear material caused by abrasive lumps which also suffers breakage or fragmentation under considerable contact pressure. Jaw crushing gouging abrasion test is considered to give the closest correlation to the abrasion encountered on earth-penetrating equipment such as excavator teeth, grader blades, as well as real jaw crusher wear (Hawk, 2000).

According to ASTM-G8, the Standard Test Method for Jaw Crusher Gouging Abrasion Test, a typical jaw crusher layout is shown in Figure 2-17. The main components involve: test plates, reference plates, a cheek plate, a toggle plate, two jaws, a flywheel, and an eccentric shaft. One test plate and one reference plate are fixed on the movable jaw frame which moves against the material being crushed, and the other test plate and reference plate are installed on the stationary jaw frame that directly contact with crushing materials. Cheek plates are wear liners and used to protect crushers' sides, whereas toggle plates are designed to hold the movable jaw.

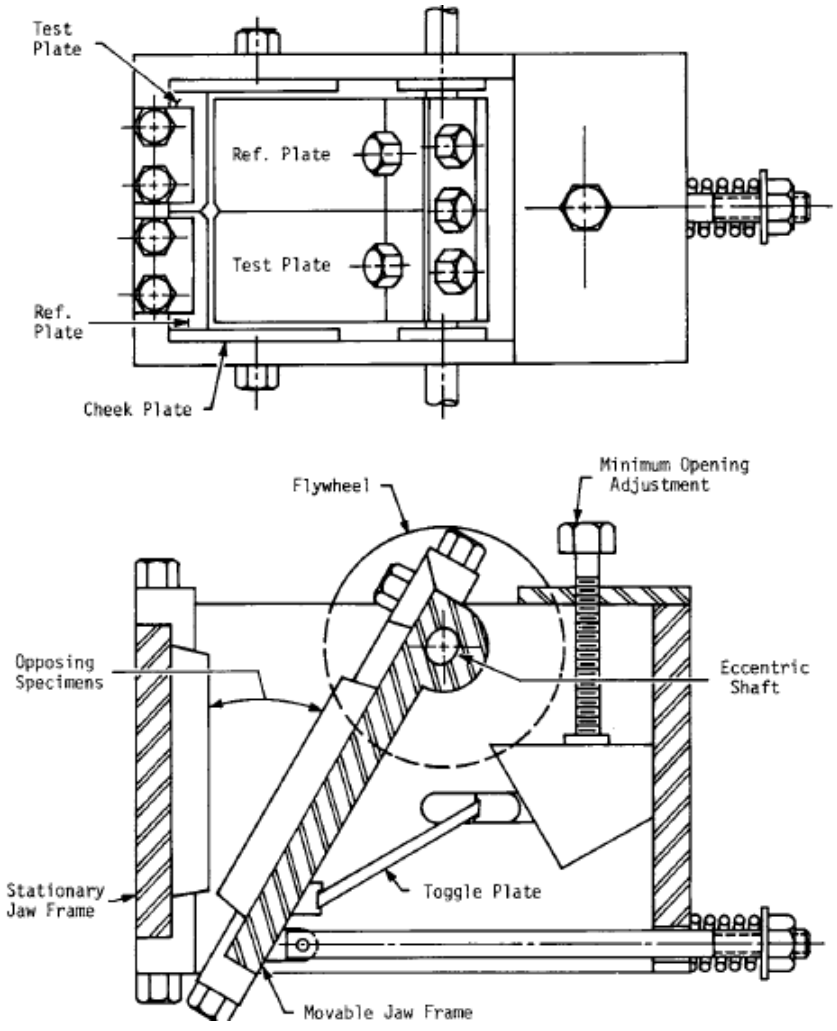

Figure 2-17: Typical crusher construction and layout (ASTM G81)

Gouging abrasion of materials can be estimated via:

$$F = \frac{Xs/Rs + Xm/Rm}{2} \quad \textbf{(2-15)}$$

Where, *Xs* and *Xm* represent the volume loss from stationary and movable test plates, while *Rs* and *Rm* means the volume loss from stationary and movable reference plates. *F* is the final wear ratio. The smaller the wear ratio value, the better the wear resistance of the tested materials. As for high wear resistance tests, the amount of rock should be 1800 kg (4000 lbs) or more. The jaw crusher gouging abrasion test is recommended in the case of cable shovels excavating hard minerals like quarrying since the ground engaging tools are supposed to undergo gouging abrasion. As thus research has focused on oil sands interactions; this jaw test will not be used here.

2.5.4 Dry Sand Rubber Wheel Abrasion Test

Another commonly used abrasion test is the ASTM-G65 (Dry Sand/Rubber Wheel Test) whose apparatus is shown in Figure 2-18. The test specimen is held against a rotating wheel comprised a specified hardness of a layer of chlorobutyl rubber coated on the rim. The required pressure between the specimen and the rubber wheel can be achieved by means of a lever arm. During the test, standard Ottawa quartz sand are followed through the specimen-wheel gap to cause abrasive wear on the specimen surface.

The standard dimension of the rubber wheel is 228 mm diameter with 12.7 mm width, and the specimen is manufactured as a rectangle, 25.4 mm wide $\times$ 75.2 mm long $\times$ 2.54 mm-12.7mm thick. The rate of sand flow is controlled from 300 to 400 g/min. The standard Ottawa sand are rounded sands with moisture content below 0.5 weight %. The general procedure contains following stages: cleaning and weighting specimen; fixing the

specimen in the holder and loading proper force between the specimen and the rubber wheel; setting the revolution counter and adjusting the sand flow; starting the wheel rotation; stopping drive motor after running desired number of wheel revolution; and removing and reweighting specimen.

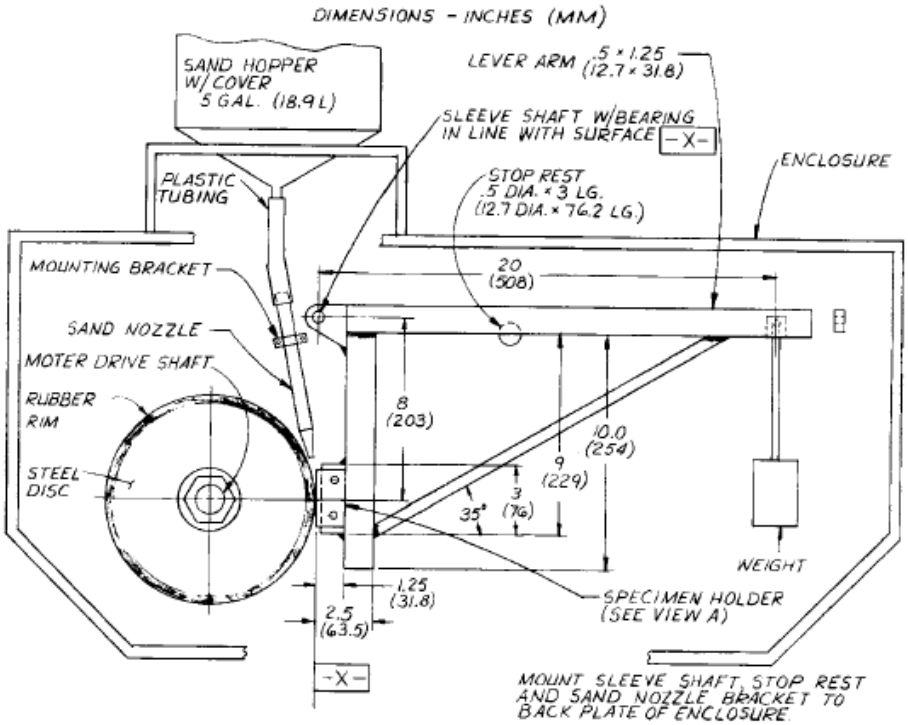

Figure 2-18: Dry sand/rubber wheel abrasion apparatus (ASTM G65)

There are five procedures recommend by ASTM G65 designed for different degrees of wear resistance defined by the sliding distance and the load between the specimen and the rubber wheel (Table 2-4). Generally, Procedure A is a severe test that is used to rank medium- and extreme abrasive-resistance materials. Procedure B and Procedure E are both short-time variations of Procedure A with distinct test durations, which are used to simulate low and medium abrasion. Procedure C characterized by the shortest time is

suitable for thin coatings, while Procedure D with lighter loads is useful for ranking materials of low abrasion resistance.

Table 2-4: Five standard test procedures

ASTM Procedure	Force on Specimen (N)	Wheel Revolution	Sliding Distance (m)
A	130	6000	4,309
B	130	2,000	1,436
C	130	100	71.8
D	45	6,000	4,309
E	130	1,000	718

The dry sand/rubber wheel test should be only used for wear ranking, not for specifying absolute wear values. Therefore, depending on real circumstances, variants of standard procedures have to be made to obtain wear information required for engineering purpose. Aside from changes in the loading weight and sliding distance, the feeding rate of sand flows, abrasive characteristics, and test duration could be reconfigured. Researches have shown that approximately 200 wheel revolutions are enough to create a steady wear rate. Multiple shorter tests could be run instead of a single long test to protect the rubber wheel (Hawk 2000).

In summary, studies on abrasion prediction are based on modeling and tests. Application of abrasion models can predict abrasive wear in shorter time with lesser cost, but lack of accuracy, since wear is a complicated process and any changes will influence wear results. By contrast, abrasion tests can give more real information about abrasive wear, however they are costly and time intensive. As for the two commonly used abrasion tests introduced above, the jaw crusher gouging abrasion test is a method to study wear of

ground engaging tools interacting with hard and large abrasives like quarry and metallic minerals. However, for the case of fine abrasives such as oil sands, the dry sand rubber wheel test is more suitable than the jaw crusher test because there is little occurrence of breakage during excavation in soft abrasive medium like oil sands.

2.6 Summary

In this chapter, the cable shovel and its related wear attacks have been reviewed. The shovel teeth or ground engaging tool are mainly subjected to abrasive wear due to the severe interaction between the tool and the grounds caused by high digging resistance which is applied to the shovel teeth surface. The solid oil sand quartz particles consisted of quartz sand in oil sand are the predominant abrasive which lead to severe abrasion on ground engaging tools. Abrasion tests conducted during the course of this research seem to closer correlate the abrasive wear experienced by shovel teeth than through modeling.

3 Relationship between Abrasion and Energy

3.1 Abrasive Cone Model

In order to understand the principle of abrasive wear a typical model of abrasive wear caused by a conical particle is shown in Figure 3-1 (Kato *et al*., 2000; Ramsey and Rahnejat, 2012).

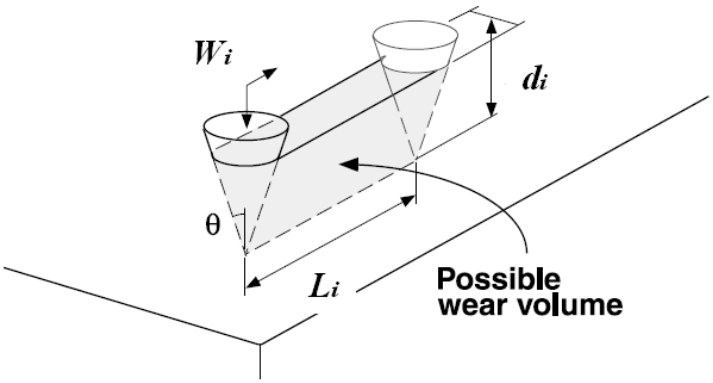

Figure 3-1: A typical model of abrasive wear by a conical particle (after Kato *et al*., 2000).

The abrasive wear is quantified as a volume loss generated by a hard particle. The possible wear volume V_i cut out by a single conical particle over a sliding distance L_i is given by:

$$V_i = d_i^2 \cdot \tan\theta \cdot L_i \qquad \textbf{(3-1)}$$

The real contact area is $\pi(d_i \cdot \tan\theta)^2/2$. Hardness H is defined as the mean normal pressure placing material in fully plasic deformation. The normal force W_i is expressed by:

$$W_i = H \cdot \pi(d_i \cdot \tan\theta)^2/2 \qquad \textbf{(3-2)}$$

Putting equation (3-2) into equation (3-1), thus penetration depth d_i^2 cancels and the possible volume loss is given by:

$$V_i = \frac{2}{\pi \cdot \tan\theta} \cdot \frac{W_i L_i}{H} \tag{3-3}$$

Equation (3-3) is a typical abrasion function. Therefore $K_{ab} = 2/\pi \cdot \tan\theta$ is called the wear coefficient and is dependent on the ductility of the material, interfacial shear strength, and particle shape. In terms of the metal abrasive wear, K_{ab} is expected to be in the range 10^{-4} to 10^{-1} (Rabinowicz, 1980).

In order to use friction energy to study abrasive wear, the friction μW_i is introduced via equation (3-3) which can be written as:

$$V_i = \frac{2}{\pi \cdot \tan\theta \cdot \mu} \cdot \frac{\mu W_i L_i}{H} \tag{3-4}$$

In adopting SI units the possible volume loss caused by friction energy then given by:

$$V_i = \frac{2}{\pi \cdot \tan\theta \cdot \mu} \cdot \frac{A E_i}{H} \tag{3-5}$$

In equation (3-5) the parameter A is related to the order of magnitude of sliding distance. For example, when the sliding distance L_i is 1 cm the value of A should be 10^{-2} so that the units of friction energy $\mu W_i L_i$ will be N•m. The determination of the *A-value* is shown in table 3-1. Actually, the sliding distance, to some extent, depends on particle size. For example, when a particle size is around 1 mm, its sliding distance should be in the range

of 0.1 cm to 1 cm , while a particle with size of 1 cm is more like to slide from 1 cm to 10 cm. Therefore parameter *A* can be considered as a particle size coefficient.

Table 3-1: Determination of *A*-value

Magnitude Order of Sliding Distance	***A* Value**
μm	10^{-6}
mm	10^{-3}
cm	10^{-2}
dm	10^{-1}
m	1

When numerous particles abrade material surfaces the total volume loss *V* may be expressed as:

$$V = \sum_{i=1}^{n} V_i = \sum_{i=1}^{n} \frac{2A}{\pi\mu \tan\theta \cdot H} E_i = \frac{2A}{\pi\mu \tan\theta \cdot H} \cdot E \qquad \textbf{(3-6)}$$

Equation (3-6) gives the relationship between abrasion (*V*), friction energy (*E*), material hardness (*H*), and the abrasive conditions characterized by the friction coefficient (μ), particle angularity (θ), and particle size (*A*). This relationship may be used to explain how material hardness, particle characteristics, contact condition, and normal force influence abrasive wear.

In specific abrasion conditions (where $2A/\mu\pi \tan\theta$ may be determined), the volume loss *V* of material with hardness *H* will be a function of the friction energy *E*. In other words abrasion by nature results from friction energy caused by the interaction between the

material and particles. Therefore it is possible to employ friction energy as a simple but effective method to quantify and predict abrasive wear.

3.2 Specific Energy

Specific energy ($E_S = E/V$) is defined as the friction energy required to cause a unit volume loss of material (J/m^3 or Pa) and it has been widely used as a measure of energy efficiency in the machining industry (Marinescu *et al*., 2013). In term of abrasive wear, according to equation (3-6), the specific energy E_S is given by:

$$E_S = \frac{E}{V} = \frac{\mu \pi H \tan\theta}{2A} \tag{3-7}$$

From equation (3-7) it can be seen that specific energy is determined by considering material hardness (H), contact condition (μ), particle angularity (θ), and particle size (A); suggesting that specific energy E_S may be an index of the abrasion conditions, upon which the resistance performance of materials to abrasive wear may be ranked. When friction energy (E) is known, the degree of abrasion (V) may be estimated through specific energy (Es). In this thesis, the principle of specific energy will be applied to the study of abrasive wear for shovel teeth in the oil sand mining industry.

According to the definition of specific energy ($E_S = E/V = \mu F v t / V$), a measure for specific energy may be:

$$\frac{V}{t} = \frac{1}{E_S} \mu F v \tag{3-8}$$

Where, V/t, F, v, and μ are volume loss rate, normal force, velocity, and friction coefficient respectively. When all parameters are known, specific energy may be obtained.

In order to apply specific energy to shovel teeth, the determination of a normal force F and velocity v is based on real field data is required. An interfacial shear test and a modified abrasion test have been designed to measure the friction coefficient and specific energy respectively.

4 Evaluation of Digging Resistance and Velocity

4.1 Introduction

Digging resistance is the leading cause for severe abrasion that occurs on ground-engaging tools. Most studies on digging resistance concentrate on the establishment of models due to versatility. However, model-based results are not always in good agreement with actual resistance expressed, since the geology and depositional environment have significant influence. Therefore, this chapter introduces a calculation methodology based on geometric analysis, making it possible to obtain digging resistance and velocity from field data generalized from an operating shovel in an oil sand mining operation.

4.2 Dipper System and Field Data

Figure 4-1 is a diagram of a dipper system, which involves five main components: (1) bucket, (2) handle, (3) boom, (4) hoist cable, and (5) saddle or swivel shaft. Field data associated with handle extension, hoist extension, velocity, armature current and voltage were recorded at 10 Hz seconds interval (Table 4-1). Some additional information can be provided through field data (Patnayak *et al.*, 2005), where positive and negative voltages imply direction of rotation of the hoist and crowd motors. For a hoist motor, its positive voltage defines the upward motion of the shovel dipper, while a negative defines the downward action. For the crowd motor, the dipper handle will extend when the crowd voltage is positive, and be in retraction when the voltage is negative. After dumping in a truck and swinging back to the mining face, the empty dipper moves downwards to position for the next excavation where both voltages and currents are negative. Before the dipper completely touches the ground, the operator would reverse the motion of dipper, changing the current measured at the hoist motor immediately from negative to positive

in advanced of the change of the voltages to stop the dipper downward motion. Similar phenomena can be seen in the data for crowd motion. Changes in length of the handle and hoist cables also imply the motion of the shovel dipper. When the dipper is moving upwards, the length of hoist cables decrease with negative velocities and vice versa.

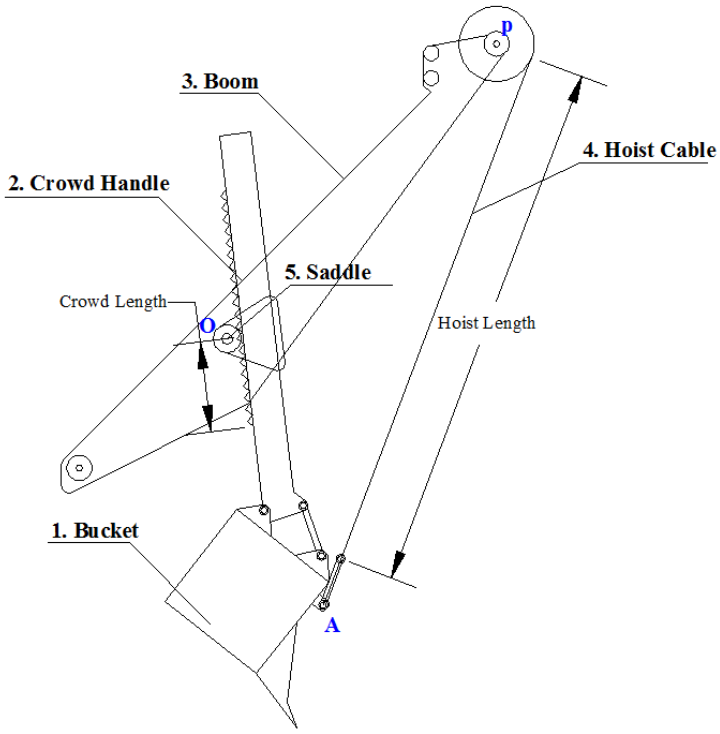

Figure 4-1: Diagram of dipper system

Crowd force and hoist force can be calculated as follows:

$$F_{Crowd} = \frac{U_{Crowd} \cdot I_{Crowd}}{v_{Crowd}} \quad \textbf{(4-1)}$$

$$F_{Hoist=} \frac{2 \cdot U_{Hoist} \cdot I_{Hoist}}{v_{Hoist}} \cdot \eta_{Hoist} \quad \textbf{(4-2)}$$

In equation (4-1) and (4-2), *U, I, and v* represent voltage, current, and velocity for one hoist motor. The efficiency η_{Hoist} represents the hoist power efficiency where this value is

0.865 for a case of P&H 4100 Boss cable shovel. The number 2 in equation (4-2) refers to the shovel has identical current and voltage values for both motors providing hoist power.

Table 4-1: Example of cable shovel field data

Time	Length		Velocity		Armature Voltage		Armature Current	
(s)	Hoist (m)	Crowd (m)	Hoist (m/s)	Crowd (m/s)	Hoist (V)	Crowd (V)	Hoist (A)	Crowd (A)
0.000	3.9886	5.5444	0	0.012991	-4	12	865.00	-46
0.101	3.9886	5.5444	0	0.012991	0	11	864.00	-102
0.202	3.9886	5.5457	0	0.012991	0	9	858.00	-52
…	…	…	…	…	…	…	…	…
12.019	18.186	0.59226	0.72102	0.48066	-454	449	2018.00	440
12.120	18.186	0.59226	0.56651	0.53262	-454	449	2018.00	440
12.221	18.258	0.64014	0.36051	0.48066	-377	482	2377.00	-105
12.322	18.314	0.69449	0.36051	0.49365	-245	493	2562.00	-354
12.423	18.35	0.74754	0.103	0.53262	-145	498	2457.00	-530
12.524	18.36	0.79413	0.051501	0.53262	-45	503	2222.00	-700
12.625	18.355	0.8433	-0.18025	0.51963	89	507	1833.00	-883
12.726	18.332	0.89894	-0.18025	0.51963	138	504	664.00	-933
12.827	18.294	0.97917	-0.18025	0.5586	136	499	-123.00	-1010
…	…	…	…	…	…	…	…	…

4.3 Digging Kinematics

4.3.1 Kinematic model

A kinematic model based on geometric analysis has been developed based on the model of Shi (2007) (Figure 4-2 (a)). The swivel shaft or saddle block center *O*, boom sheave center *P*, and bucket hinge *A* form an triangle ΔOPA. Dash lines OO_1 and OA_3 are the rotating vertical and horizontal axes of the saddle respectively. Since the bucket and saddle are rotating simultaneously, the distance l_{OO_1} is constant. Both $l_{O_1A_2}$ and l_{OA_3} are equal to l_{Crowd}, while $l_{A_1A_4}$ is equivalent to l_{Hoist}. l_{PA_4} is the radius of sheave, and l_{AA_2} and l_{AA_1} are fixed distances. In the triangle ΔOPA one side *OP* is equivalent to the boom

length, and the other two sides *OA* and *AP* are determined by equation (4-3) and equation (4-4).

$$l_{OA} = \sqrt{(l_{O_1A_2} + l_{A_2A})^2 + l_{OO_1}^2} \quad \textbf{(4-3)}$$

$$l_{PA} = \sqrt{(l_{AA_1} + l_{A_1A_4})^2 + l_{PA_4}^2} \quad \textbf{(4-4)}$$

Where $l_{O_1A_2} = l_{OA_3} = l_{Crowd}$ and $l_{A_1A_4} = l_{Hoist}$. The values of l_{Hoist} and l_{Crowd} are provided from field data. l_{A_2A}, l_{AA_1}, l_{PA_4}, l_{OO_1}, and l_{OP} are fixed distances and their values are given in Table 4-2.

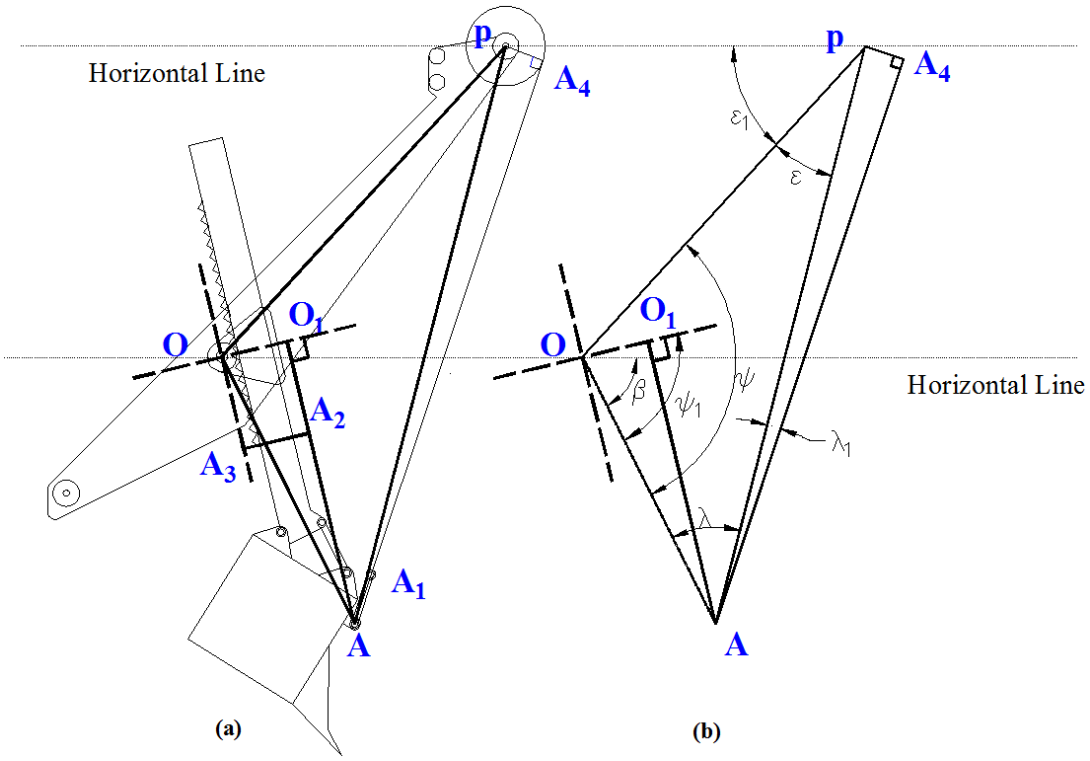

Figure 4-2: Kinematic diagram of dipper system (after Shi, 2007)

Figure 4-2 (b) is a free body diagram of the dipper system which shows all angles of motion. In triangle ΔOPA, these three angles ψ, λ, and ε are calculated through equations (4-5), (4-6) and (4-7).

$$\psi = \arccos\sqrt{\frac{l_{OA}^2 + l_{OP}^2 - l_{AP}^2}{2l_{OA}l_{OP}}} \quad \textbf{(4-5)}$$

$$\varepsilon = \arccos\sqrt{\frac{l_{PA}^2 + l_{OP}^2 - l_{OA}^2}{2l_{PA}l_{OP}}} \quad \textbf{(4-6)}$$

$$\lambda = 180^0 - \psi - \varepsilon \quad \textbf{(4-7)}$$

Other angles are determined through equation (4-8) to equation (4-10).

$$\beta = (90^0 - \psi_1) + (\psi - \varepsilon_1) \quad \textbf{(4-8)}$$

$$\psi_1 = \arctan(\frac{l_{O_1A}}{l_{OO_1}}) \quad \textbf{(4-9)}$$

$$\lambda_1 = \arctan(\frac{l_{PA_4}}{l_{AA_4}}) \quad \textbf{(4-10)}$$

Where:

ε_1 Boom angle; constant and its value is about 42^o

λ_1 Cable angle between the triangle side *PA* and hoist cable

ψ_1 Angle between the handle direction *OA* and vertical axis of saddle OO_1

β Handle angle between the triangle side *OA* and horizontal line. In this thesis, β is designated positive when the handle is below horizontal line and vice versa

Table 4-2 provides with values of fixed distances which are necessary to calculate lengths and angles in this model. These lengths and angles are basic parameters of the kinematic

model, upon which the digging trajectory, digging resistance, and velocity may be obtained.

Table 4-2: Values of fixed distance

Line	Name	Dimension (m)
l_{AA_2}	Crowd linkage	6.67
l_{AA_1}	Hoist linkage	2.11
l_{PA_4}	Sheave radius	1.22
$l_{OP} = l_{Boom}$	Boom length	15.33
l_{CA_2}	Fixed distance	10.22
l_{B_2B}	Fixed distance	6.22
$l_{A_3A_5}$	Fixed distance	2.67
l_{AC}	Distance between the hinge and tooth tip	3.29
l_{OO_1}	Distance between the saddle block and hinge	1.78
l_{OO_2}	Distance between the saddle block and tooth tip	1.56
l_{OO_3}	Distance between the saddle block and point of action of handle weight	0.89
l_{OO_4}	Distance between saddle block and point of action of bucket weight	0.29

4.3.2 Digging trajectory

The digging trajectory is determined by the motion of the shovel teeth. A 2-D geometric analysis of digging trajectory is shown in Figure 4-3 (a), in which the saddle block center

O, boom sheave center *P*, and tooth tip *C* form a triangle ΔOPC associated with motion of the shovel teeth. Two dash lines OO_2 and OA_3 are the horizontal and vertical axes of the saddle block center. Since the teeth and saddle are rotating simultaneously, the distance l_{OO_2} should keep constant. Both l_{AC} and l_{CA_2} are fixed distances. Lines OA_3 and O_2A_2 are the crowd extension. Resolving the distance relative to the tooth tip referencing lengths *X* and *Y*, the digging trajectory may be determined through equation (4-11) and (4-12):

$$X = \sum(\Delta l_{OC} \cdot \cos\beta_1 + \Delta l_{CP} \cdot \cos\eta) \quad \textbf{(4-11)}$$

$$Y = \sum(\Delta l_{OC} \cdot \sin\beta_1 + \Delta l_{CP} \cdot \sin\eta) \quad \textbf{(4-12)}$$

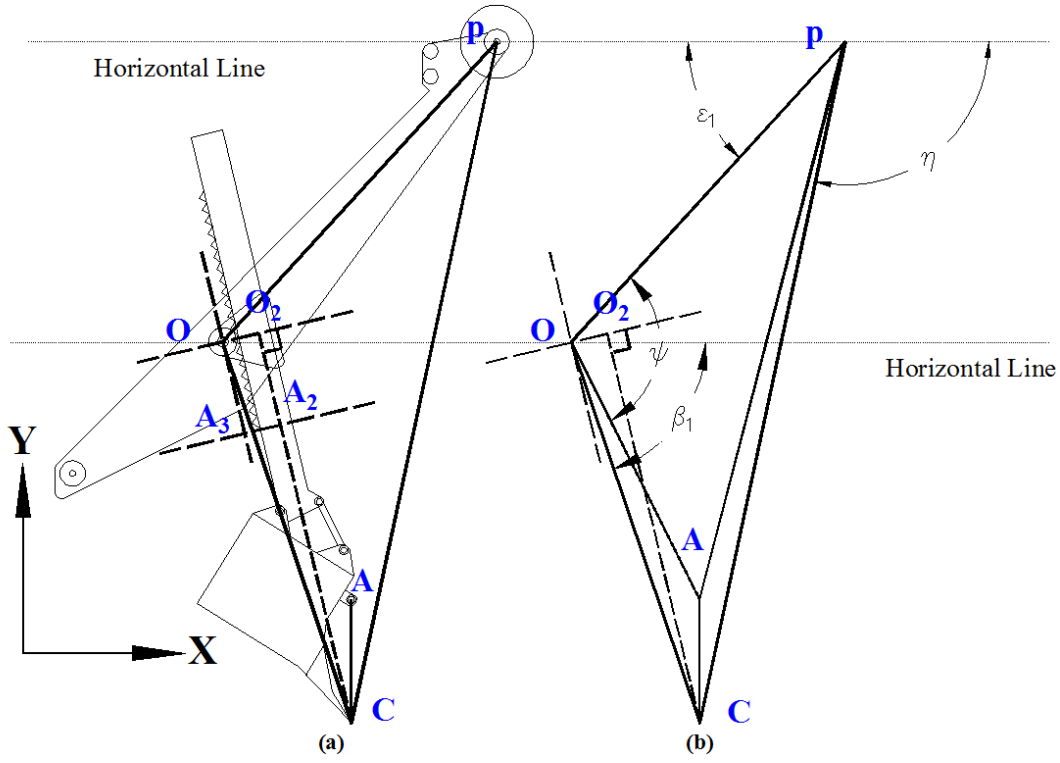

Figure 4-3: 2-D Digging trajectory analysis

From the free body diagram (Figure 4-3 (b)) the hoist angle η, digging angle β_1, l_{OC}, and l_{PC} may be obtained via equations from (4-13) to (4-16):

$$\beta_1 = \psi - \varepsilon_1 + \angle COA \quad \textbf{(4-13)}$$

$$\eta = \pi - (\varepsilon_1 + \angle OPC) \quad \textbf{(4-14)}$$

$$l_{OC} = \sqrt{l_{O_2C}^2 + l_{OO_2}^2} \quad \textbf{(4-15)}$$

$$l_{PC} = \sqrt{l_{OP}^2 + l_{OC}^2 - 2l_{OP} \cdot l_{OC} \cdot \cos(\psi + \angle COA)} \quad \textbf{(4-16)}$$

Referencing ψ, ε_1, and l_{OA} as discussed in section 4.3.1, and the value of constant space l_{OO_2} is given in Table 4-2. These three parameters l_{OC}, $\angle COA$, and $\angle OPC$ may be given by equations (4-17) to (4-19):

$$l_{O_2C} = l_{O_2A_2} + l_{A_2C} \quad \textbf{(4-17)}$$

$$\angle COA = \arccos\left(\frac{{l_{OA}}^2 + {l_{OC}}^2 - {l_{AC}}^2}{2l_{OA} \cdot l_{OC}}\right) \quad \textbf{(4-18)}$$

$$\angle OPC = \arccos\left(\frac{{l_{OP}}^2 + {l_{CP}}^2 - l_{OC}^2}{2l_{OP} \cdot l_{CP}}\right) \quad \textbf{(4-19)}$$

Where l_{AC} and l_{A_2C} are fixed distances whose values are shown in Table 4-2. $l_{O_2A_2}$ and l_{OP} are equal to the l_{Crowd} and l_{Boom} lengths respectively.

The actual digging trajectory is shown in Figure 4-4 for three digging cycles compared together from the same field data. Cycle one is now used as an example to illustrate a single digging cycle. Initially, the dipper is positioned towards the face where penetration has not yet occurred (section *OA*). Next, the dipper commences penetration (section *AB*) of the face and then raking up the face (section *BD*) until the dipper is full (point *D*). The

change of the digging curve at point *C* is due to harder toe mineral deposits. Finally the dipper retracts and prepares for swinging and dumping (section *DE*). It should be noted that although three digging cycles are shown in the same graph, it does not necessarily mean that the trajectory of cycle one becomes the next digging face for cycle two (the same as cycle two and cycle three). In actual practice, the next digging face is almost impossible to predict from the previous digging profile, as minerals will fall down and mask the previous digging face between cycles.

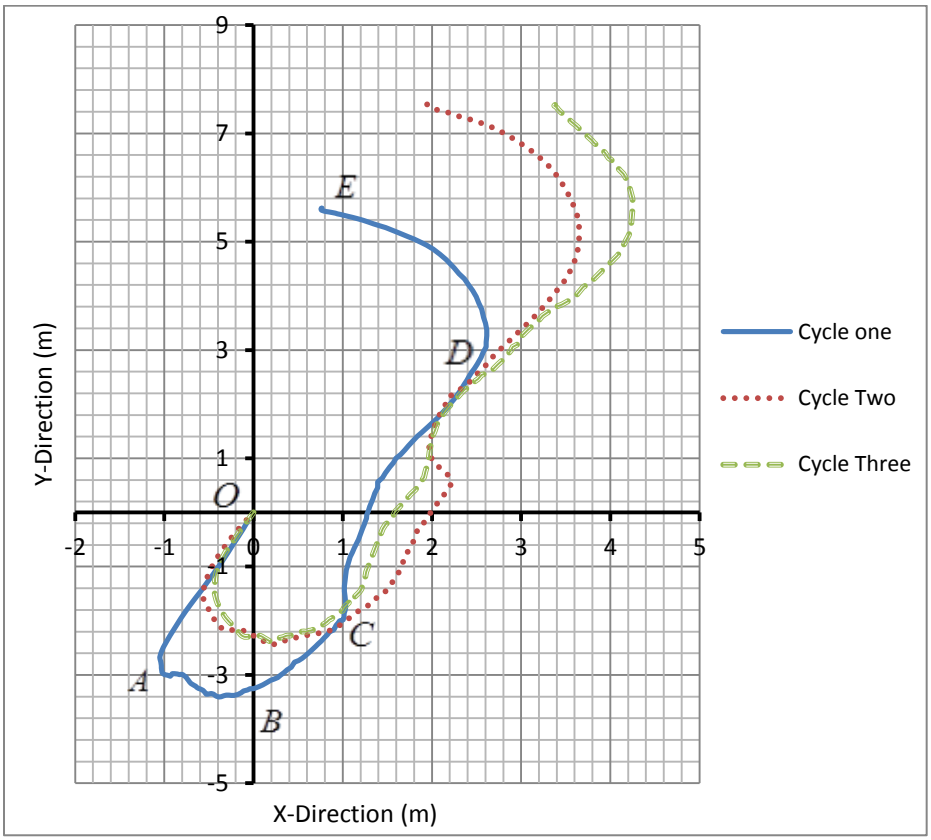

Figure 4-4: Actual field digging trajectories of 3 different digging cycles

4.3.3 Digging velocity

Digging velocity has a significant influence on abrasive wear for shovel teeth. In Figure 4-5, v_h is the hoist velocity which is positive when the dipper moves upwards, while v_c is

the crowd velocity which is positive when the dipper moves forwards. v_t is defined as the digging velocity at the teeth-ground contact, which is the result of velocities v_h and v_c in via equation (4-20).

$$v_t = v_c \cdot \cos[\beta_1 - (\alpha + \xi)] - v_h \cdot \cos[\eta - (\alpha + \xi)] \quad \textbf{(4-20)}$$

Where α and ξ are the pitch and blade angles respectively (Figure 4-12) which will be discussed in section 4.4.4. The determination of v_c and v_h may be expressed as:

$$v_c = \frac{dl_{CO}}{dt} \quad \textbf{(4-21)}$$

$$v_h = \frac{dl_{CP}}{dt} \quad \textbf{(4-22)}$$

The rate of change of l_{CO} and l_{CP} may be calculated based on the field data.

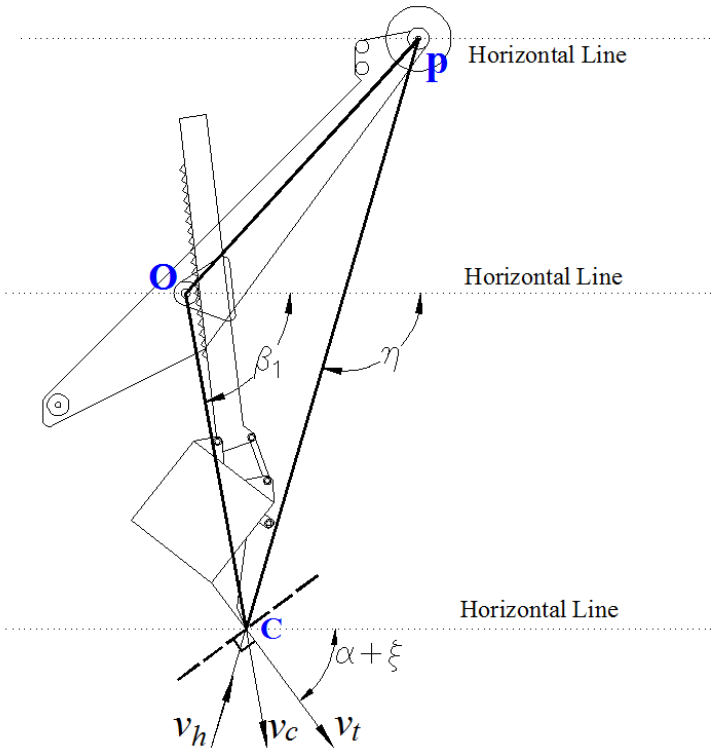

Figure 4-5: Schematics of digging velocities

Figure 4-6 shows the actual digging velocity at the teeth-ground contact regardless of direction of motion. It can be seen that v_t tends to increase all the time with a stall occurrence in the middle of digging cycle. This behaviour matches the digging trajectory where the excavation process halts due to stalling when encountering a harder mineral deposit (point *C* in Figure 4-4 and Figure 4-6). The velocity range is from 0 to 1.09 m/s. This actual velocity was used to design the abrasion test (section 5.3.2).

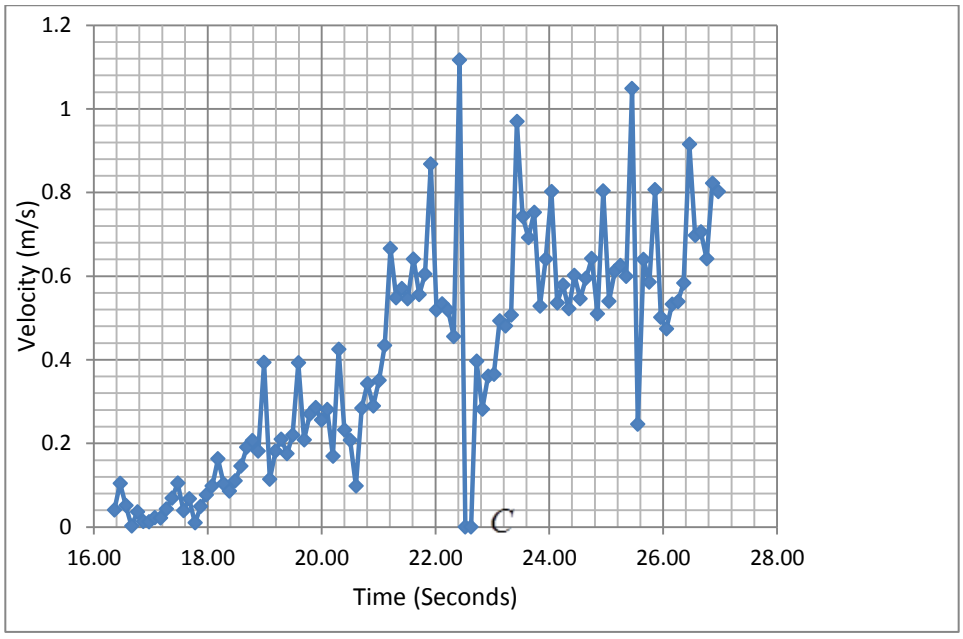

Figure 4-6: Actual digging velocity at the teeth-ground contact

4.4 Digging Resistance

4.4.1 Static equilibrium for a dipper system

The static analysis has been based on the existing passive theory widely employed to study digging motions of earthmoving machines with retaining walls aspect of the dipper structure (Stephane *et al*., 2001). In this thesis this static analysis for the dipper system has been adopted for the sake of simplicity (Figure 4-7).

Seven key forces: (1) hoist force, F_h; (2) crowd force, F_c; (3) weight of handle, G_h; (4) total weight of bucket and excavated ore, G_b; (5) digging resistance R, which is a resultant force of the penetration-cutting resistance and friction between the bucket and oil sand; (6) x-direction constraining force reflected at the saddle F_{Ox}; (7) y-direction constraining force reflected at the saddle F_{Oy}. Of these forces, the first four F_h , F_c, G_h, and G_b are active, while the latter three R, F_{Ox}, and F_{Oy} are passive forces only generated as reactions during excavation. In terms of points of action, G_h is considered to act at the center of extended handle. The point of action of G_b is regarded as the centroid of the bucket even though it varies during the excavated process. The influence caused by changes of the action of G_b are minor within the overall scale of the force equilibrium. R analysis is deemed to apply on the surface of the teeth with minor variations to the point of application (Joseph and Shi, 2012). The saddle block center O has been selected as the pivot point and the free body diagram of the dipper system is then shown in Figure 4-7(b).

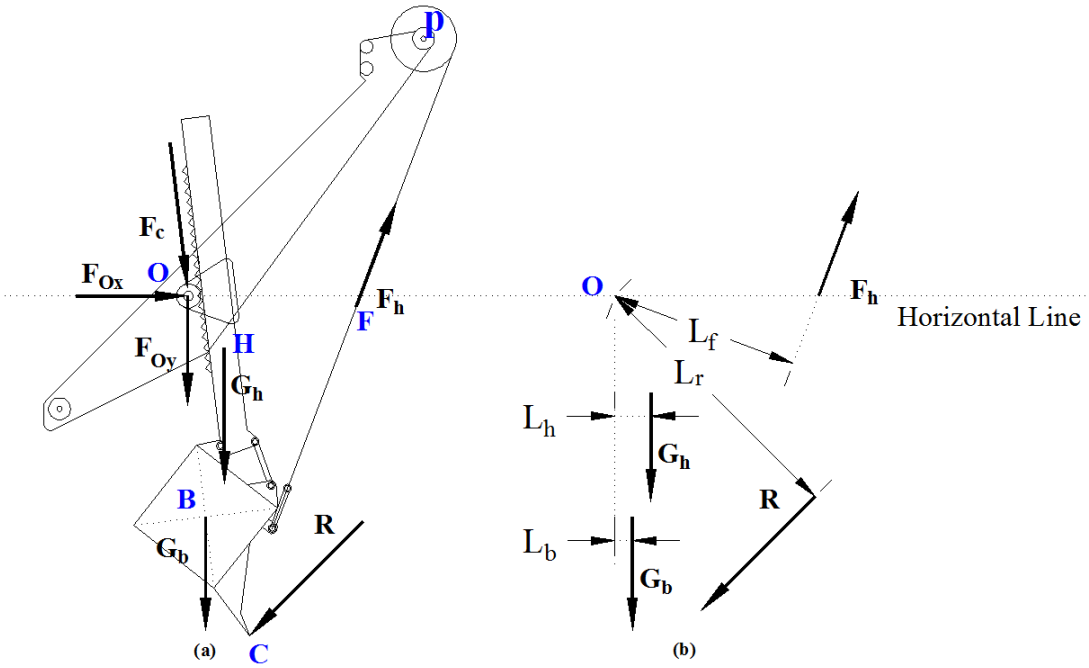

Figure 4-7: Static equilibrium for a dipper system

Since F_{Ox} and F_{Oy} apply at the pivot (point O), both moments about that point will be zero. The magnitude of the moment arm of the crowd force is much smaller than that of any of the other forces and it can also be neglected. This is also justified as the crowd force is at least 2 order's magnitude smaller than the hoist force and only comes into play for initial positioning of the shovel dipper at the toe of the face. Finally the equilibrium equation is shown below:

$$R = \frac{F_h L_f - G_h L_h - G_b L_b}{L_r} \tag{4-23}$$

If forces F_h, G_h ,G_b and moment arms L_h, L_b, L_f, L_r are known, then the digging resistance R may be obtained.

4.4.2 Hoist Force and Handle Weight

Figure 4-8(a) shows that geometic analysis for the hoist force (F_h) and the handle weight (G_h).

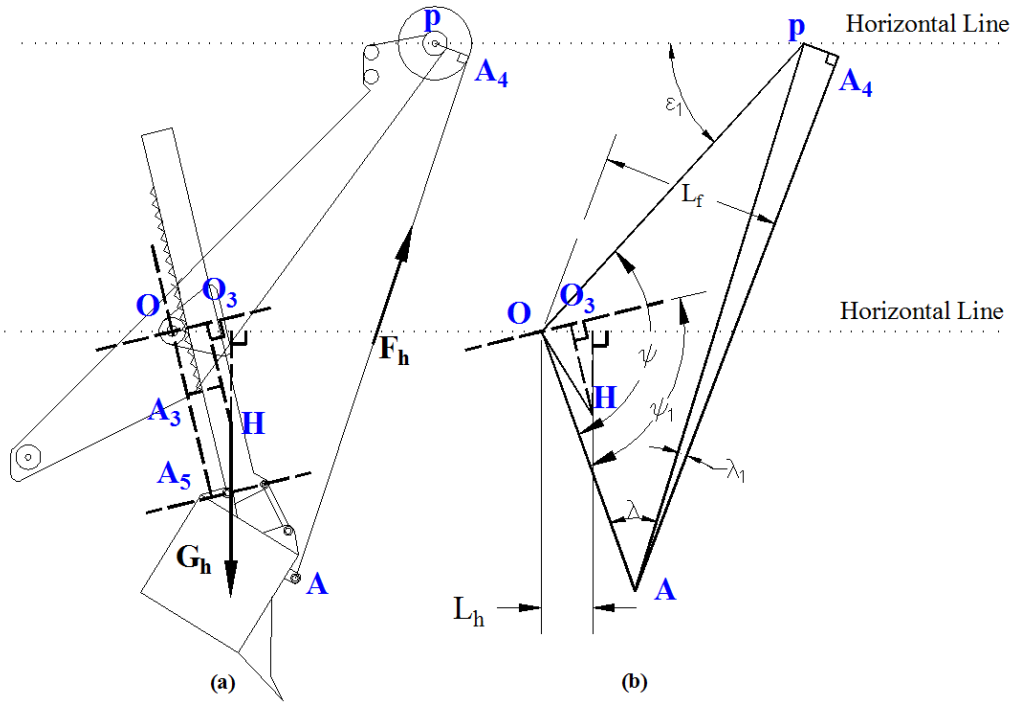

Figure 4-8: Schematic of hoist force and weight of handle

In Figure 4-8(a), F_h is the tension of the hoist cable. G_h is considered applied at the center of the extended handle (point *H*), so that line O_3H is half the length of the extended handle. Since the handle and saddle rotate simultaneously, the distance l_{OO_3} should remain unchanged. Line OA_3 is equal to the crowd length and line A_3A_5 is constant.

Figure 4-8 (b) is the free body diagram. The value of hoist force (F_h) is discussed from field data (equation (4-1)) and its moment arm is given by:

$$L_f = \sin(\lambda + \lambda_1) \cdot l_{OA} \tag{4-24}$$

Calculation of parameters λ, λ_1, and l_{OA}, were discussed in the kinematic model (section 4.3.1). The value of G_h and its moment arm distance L_h are shown in equations (4-25) and (4-26).

$$G_h = l_{Extend} \cdot \frac{G_{Handle}}{L_{Handle}} \tag{4-25}$$

$$L_h = l_{OH} \cdot \cos[(\psi - \varepsilon_1) - (\psi_1 - \angle HOO_3)] \tag{4-26}$$

G_{Handle}/L_{Handle} is defined as the weight density of handle. Values of G_{Handle} and L_{Handle} are provided in Table 4-3. Angles ψ and ε_1 were discussed in section 4.3.1. l_{Extend} is the sum of the crowd length (l_{OA_3}) and fixed distance ($l_{A_3A_5}$). Angle $\angle HOO_3$ is equal to the arc tangent of l_{OH}/l_{OO_3}, in which l_{OO_3} is constant with a value of 0.89 m (Table 4-2). l_{OH} may be found via equation (4-27).

$$l_{OH} = \sqrt{l_{OO_3}^2 + l_{O_3H}^2} \tag{4-27}$$

In equation (4-27) the length of l_{O_3H} is as half that of l_{Extend} .

Table 4-3: Parameter of a dipper system

Parameter	Value
Handle Wength	12.44 m
Handle Weight	380.79 kN
Weight Density of Handle	30.6 kN/m
Bucket Weight	792.76 kN

4.4.3 Total weight of bucket and excavated ore

Figure 4-9 (a) shows a geometic analysis for the total weight of the bucket and excavated ore (G_b).

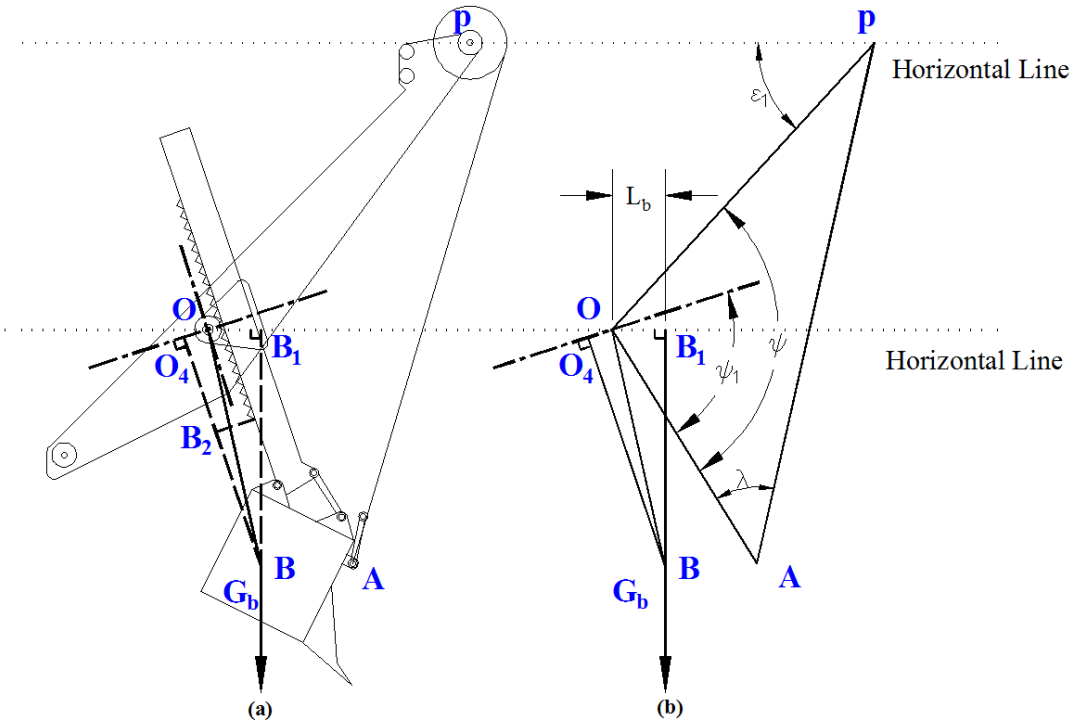

Figure 4-9: Schematic of weight of bucket and excavated ore

The centroid of the bucket (Point *B*) is the action point of G_b. Since the bucket and saddle rotates simultaneously, the distance l_{OO_4} is fixed. Line O_4B_2 is the crowd length and line B_2B remains constant. From the free body diagram (Figure 4-9 (b)), L_b may be expressed as equation (4-28):

$$L_b = l_{OB} \cdot \sin(\angle OBB_1) \tag{4-28}$$

Where parameters l_{OB} and $\angle OBB_1$ may be obtained via equations (4-29) and (4-30):

$$l_{OB} = \sqrt{(l_{O_4B_2} + l_{B_2B})^2 + l_{OO_4}^2} \tag{4-29}$$

$$\angle OBB_1 = \frac{\pi}{2} - \{(\psi - \varepsilon_1) + [\pi - (\psi_1 + \angle O_4OB)]\} \tag{4-30}$$

In equation (4-30), $\angle O_4OB$ is equivalent to the arc tangent of l_{BO_4} / l_{OO_4} and $l_{O_4B_2}$ is equal to l_{Crowd}; where l_{B_2B} and l_{OO_4} are constant, and their values are shown in Table 4-2. Angles ψ, ψ_1, and ε_1 were previously discussed in section 4.3.1.

The total weight of bucket and excvavted ore(G_b) is shown by equation (4-31).

$$G_b = G_{Bucket} + G_{Ore} \tag{4-31}$$

The value of G_{Bucket} is known from the manufactures' dada (Table 4-3), but G_{Ore} changes within excavation processes and is estimated here. Based on the fact that G_{Ore} is dependent on the digging motion, it is possible to estimate G_{Ore} via the digging trajectory (Figure 4-10).

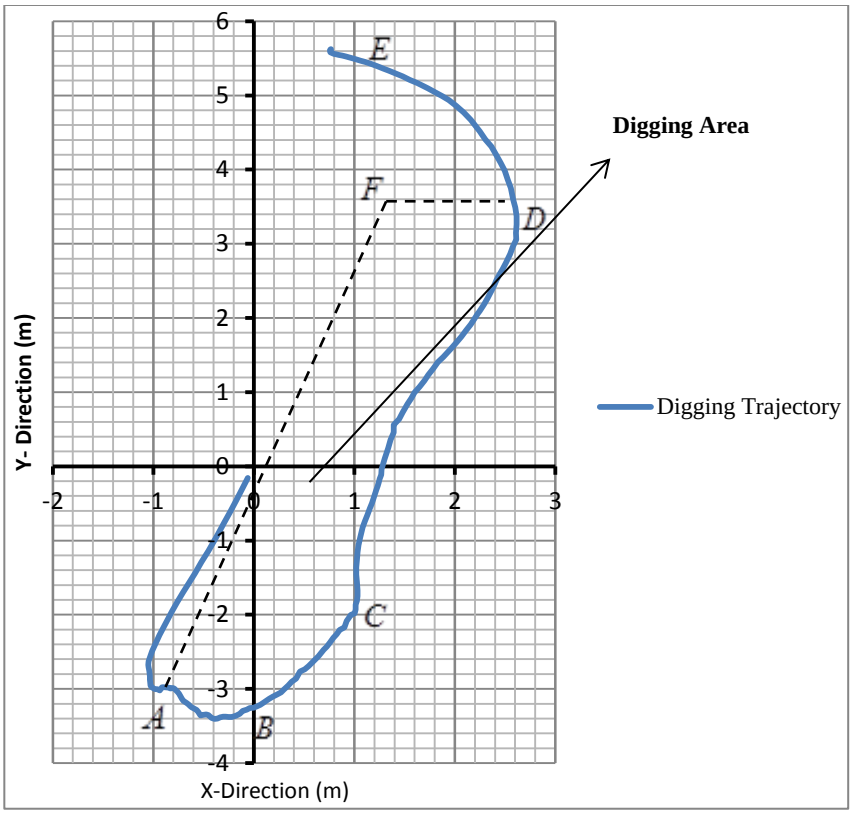

Figure 4-10: Estimation of ore excavated during digging cycle

The area ABCDF formed by oil sand slope (line *AF*) and digging trajectory (curve *ABCD*) can be taken as the excavated area. From the field data, 65° is selected as the slope, which is in the natural range of oil sand (Dusseault and Morgenstern, 1978). Therefore G_{Ore} may be determined by:

$$G_{Ore} = \sum_{i=1}^{n} \Delta G_{Ore(i)} = \sum_{i=1}^{n} A_i \cdot W \cdot \rho \cdot S \qquad \textbf{(4-32)}$$

Whereas

W	Width of bucket (3.51 m for P&H 4100 Boss cable shovel)
ρ	Oil sand density (1.65 x 10^3 t/m^3)
S	Swell factor (1.3)
A_i	Digging area of the i^{th} segment

$\Delta G_{Ore(i)}$ The amount of ore excavated in the i^{th} segment

Substituting for G_{Ore} from equation (4-32) into equation (4-23), the i^{th} digging resistance (R_i) is shown as:

$$R_i = \frac{F_h L_f - (G_h L_h + G_{Bucket} L_b + \sum \Delta G_{Ore(i-1)} L_b + \Delta G_{Ore(i)} L_b)}{L_r} \quad \textbf{(4-33)}$$

R results show that the order of $F_h L_f$, $G_h L_h$, RL_r and $G_{Bucket} L_b$ are 10^7, much higher than that of $\Delta G_{Ore(i)} L_b$ which is only 10^4. In other words the influence caused by estimation errors for $\Delta G_{Ore(i)} L_b$ can be ignored due to the much smaller order of magnitude of $\Delta G_{Ore(i)}$ compared with any of other forces. Therefore this estimation method based on digging trajectory is reasonable.

4.4.4 Resistance

Figure 4-11(a) shows the geometric analysis for resistance R. Figure 4-11(b) is the free body diagram. The resistance arm L_r is given by equation (4-34).

$$L_r = l_{OC} \cdot \sin(\varepsilon_1 + \angle OPC + \angle OCP - \gamma) \quad \textbf{(4-34)}$$

In equation (4-34), the calculation for l_{OC} has been discussed in section 4.4.2. The determination of resistance angle γ is given by Joseph and Shi (2012) in equation (4-35).

$$\gamma = \xi + \delta + \alpha \quad \textbf{(4-35)}$$

Figure 4-12 shows the interaction between the lip (blade), teeth, and ground, in which the determination of δ and ξ can be obtained via equations (4-36) and (4-37).

$$\xi = \beta - \tau \tag{4-36}$$

$$\delta = \frac{\pi}{2} - \{(\lambda_1 + \lambda) + [\tau + (\frac{\pi}{2} - \psi_1)]\} \tag{4-37}$$

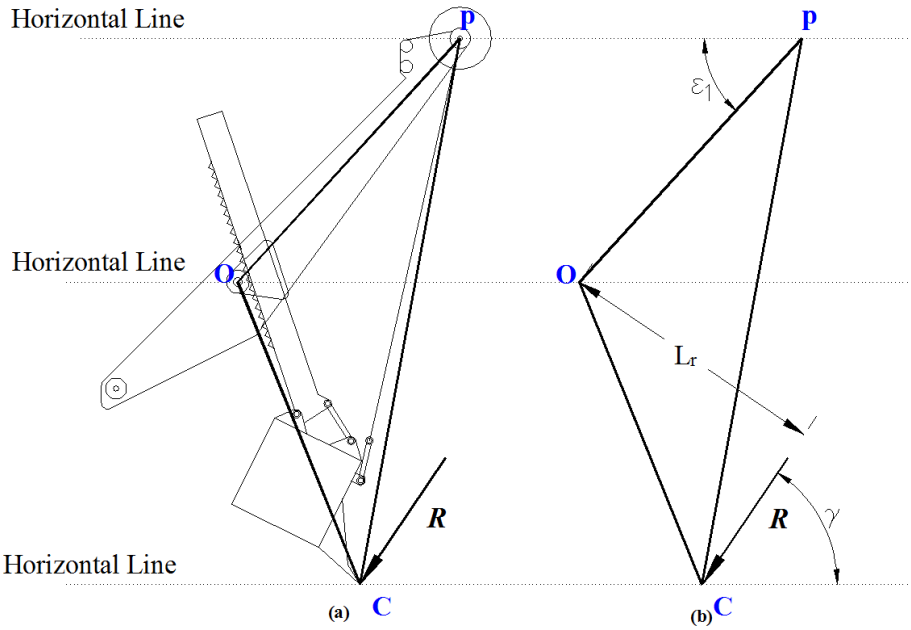

Figure 4-11: Schematic of resistance

In equations (4-36) and (4-37), λ_1, λ, β, and ψ_1 have been discussed in section 4.3.1. Other angles α, ξ, τ, and δ are declaimed as:

- α Pitch angle between blade direction and teeth direction.
- ξ Lip (blade) angle between blade direction and horizontal, which is negative when it is below the horizontal datum and vice versa.
- τ Bucket angle between blade direction and vertical axis of the saddle block has a value of 57^o.

δ Lift angle between the cable direction and the perpendicular line relative to the blade direction.

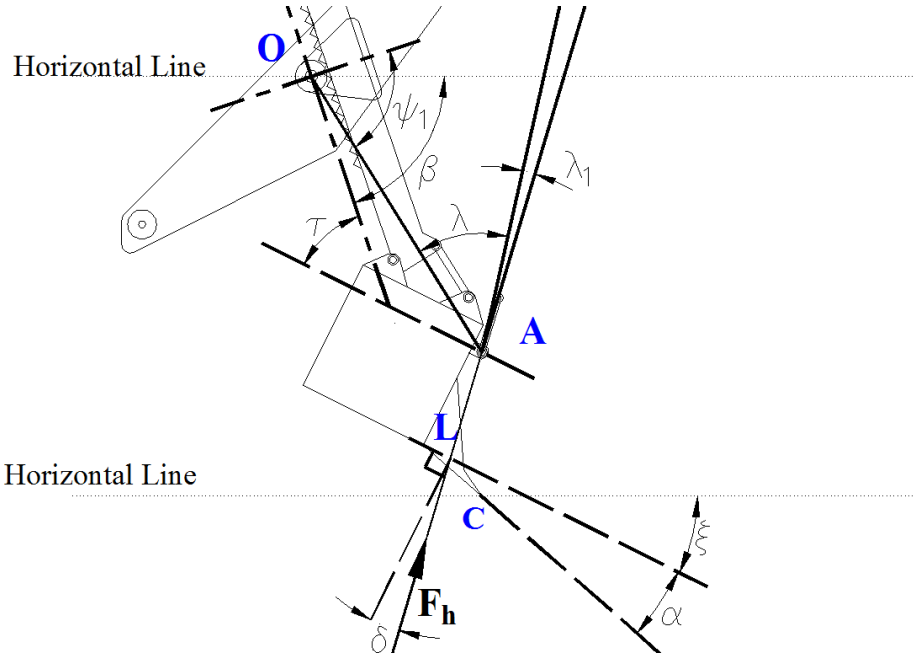

Figure 4-12: Interaction between the lip (blade), teeth, and ground

4.5 Normal Resistance

The nature of abrasive wear for shovel teeth operating in oil sands results primarily from friction; such that a digging resistance should be modified to a normal resistance so as to obtain friction value. From Figure 4-13 the normal resistance applied on the lip (blade) and teeth surface are given by equations (4-38) and (4-39) respectively.

$$R_n = R \cdot \cos(\frac{\pi}{2} + \xi - \gamma) \tag{4-38}$$

$$R_n^{'} = R \cdot \cos[(\frac{\pi}{2} + \xi - \gamma) + \alpha] \tag{4-39}$$

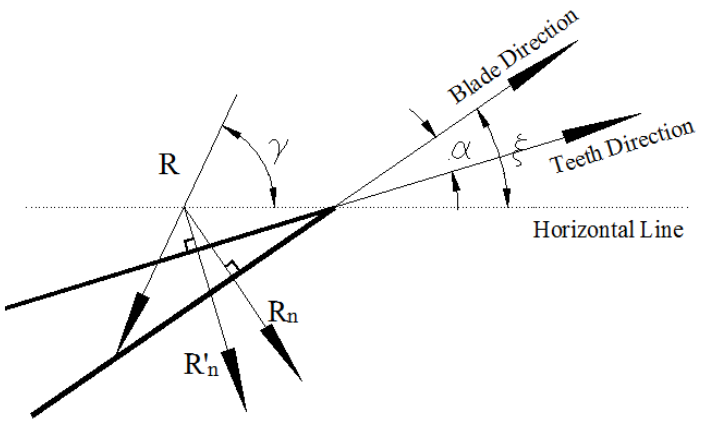

Figure 4-13: Schematic of normal resistance

The actual normal resistance applied on the teeth surfaces is shown in Figure 4-14. It can be seen here that $R_n^{'}$ increases at first and then remains relatively stable around 1350 kN, but finally it drops below 200 kN. Generally normal resistances applied to teeth surfaces range from 400 kN to 1600 kN with an average of 970 kN. The actual normal resistance will be used to design the abrasion test (section 5.3.2).

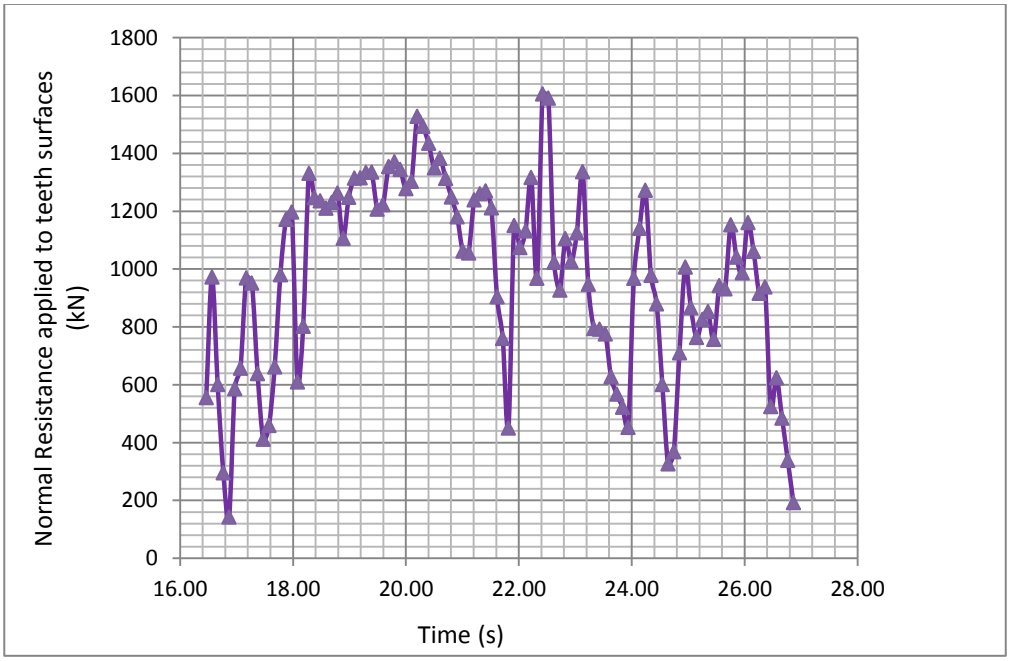

Figure 4-14: Actual normal resistance applied to teeth surfaces

5 Abrasion Test

5.1 Introduction

In order to measure specific energy a modified rubber-wheel abrasion test (MRWAT) has been designed based on the standard dry sand/rubber wheel abrasion test (ASTM-G65) with the main advantage of mimicking actual abrasive conditions. This chapter will describe the MRWAT apparatus, selection of materials, and application of the scaled factor.

5.2 Abrasion Test Apparatus

A schematic diagram and a photograph of the experimental setups of the MRWAT test are shown in Figure 5-1 and Figure 5-2.

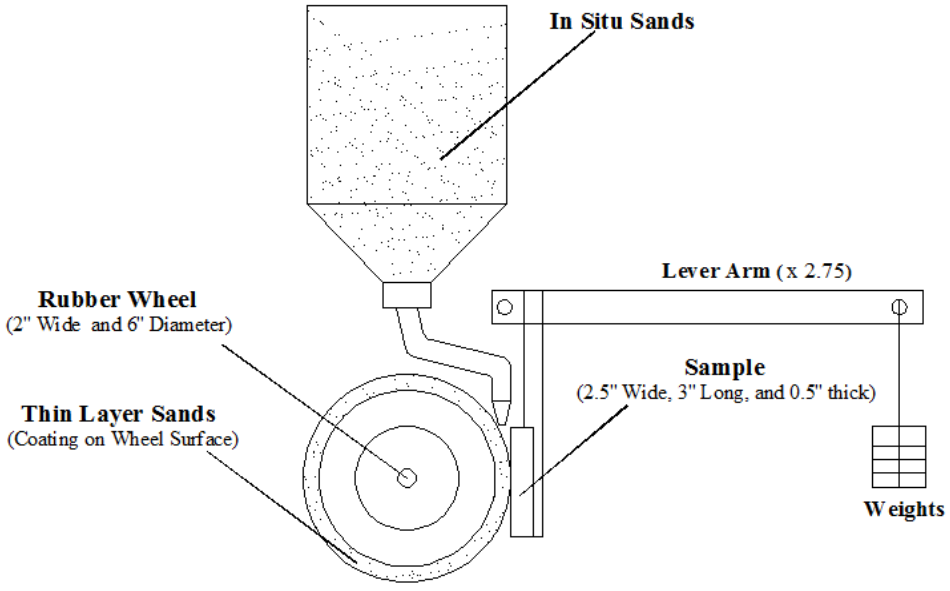

Figure 5-1: Schematic diagram of the MRWAT apparatus

This apparatus is similar to the standard ASTM-G65 setup but there are two major differences: the abrasive medium used and the wheel. Oil sand has zero cohesion but high

friction angle (Morgenstern and Scott, 1997). The quartz particles in oil sand vary in shapes involving angular, semi-angular, semi-rounded, and rounded, and all described generally as being sub-angular. Therefore in-situ quartz sand was instead of the standard AFS 50/70 test sand, consisting of rounded quartz grains generally used in the ASTM G65 as abrasives. The ASTM G65 specifies a rubber wheel with 9'' diameter and 0.5'' wide, while the MRWAT use a 6'' diameter rubber wheel 2'' wide. This new wheel was coated with a thin layer of oil sands with advantage of (i) protecting rubber wheel from severe abrasive damage; (ii) ensuring full contact between sand and materials; (iii) decreasing in the change of contact area at different levels of load.

Figure 5-2: Photograph of the MRWAT apparatus

The MRWAT test has been designed as a low-stress abrasion test to avoid comminution of particles. The low level of contact stress ensures that most of the friction energy

transfer into the abrasion of the targeted materials rather than breakage of thus sand particles. The actual normal force obtained from the field data is huge and as such it should be scaled down to an appropriate value. This is discussed in section 5.3.2.

5.3 Abrasion Test Specimen and Parameters

5.3.1 Test specimen

Material hardness has a significant influence on degree of abrasive wear and it is the major selection criteria for materials. Four of metals with different hardness were selected for the tests (Figure 5-1): Aluminum 6063-T6, Aluminum 6061-T6, Mild Steel, and Stainless Steel. These materials were chosen because they represent a hardness range, measured using a Shore Sclerometer and need to indicate HV (Vickers hardness number).

Table 5-1: Properties of metal specimen

Metal	Standard Number	Density	Average Shore Number	Vickers Hardness
Aluminum 6063-T6	ASTM B-221	2.7 g/cm^3	-	83
Aluminum 6061-T6	ASTM B-209	2.7 g/cm^3	-	107
Mild Steel A36	ASTM A36	7.85 g/cm^3	32	213
Stainless Steel 17-4SS	ASTM A693	7.85 g/cm^3	40	279

5.3.2 Test parameters

Normal Force

Normal force applied to samples is one of the most important parameters. Calculation results show that actual normal resistance applied to teeth surfaces is in the range of 400 kN to 1600 kN (Figure 4-14). Keeping the same contact stress, the applied normal load

held perpendicular to samples in tests could range from 390 N to 1380 N, corresponding to 400 kN and 1600 kN in the field data. This load range is much higher than the instrument limits. Hence a scale factor was taken into consideration to actual normal resistance into acceptable lab normal loads through equation (5-1).This was based on the ratio of the teeth area to the coupon contact area for the test.

$$SF = \sqrt{\frac{A_{Teeth}}{A_{Contact}}} = 12 \qquad \textbf{(5-1)}$$

Table 5-2: Conversion among actual normal resistance, lab normal force, and weights

Weights (LBS)	**Lab Normal Loads** (Weights + Lever Weight) x Lever Arm Ratio (2.75) (N)	**Normal Resistance** (Lab Contact Force x SF^3) (kN)
0	32	454
1	44	625
2	57	797
3	69	969
4	82	1140
5	94	1312
6	106	1483
7	118	1655
8	131	1826

Table 5-3 shows the conversion from actual normal resistance obtained from the field data, to lab normal loads, and to weights. After scaling, the lab normal loads ranged from 32 N to 130 N, which falls within an acceptable range for operation of the designed experimental tools.

Rotation Speed

Another important parameter is the rotation speed. Its determination is related to the field data. From Figure 4-6, the actual digging velocities of the teeth surfaces were evaluated

and found to vary from 0 m/s to 1.09 m/s, with a large proportion falling in the range of 0.2 m/s and 0.8 m/s. Since the actual digging velocity was not high, and the velocity with no scaling required has deemed. The conversion from the actual digging velocities to rotation speed is shown in Table 5-3.

Table 5-3: Conversion between actual digging velocities and rotation speed

Real Digging Velocity (m/s)	**Rotation Speed** (RPM-Revolution per Minutes)
0.2	25
0.4	50
0.6	75
0.8	100

Abrasive Media

The sand used in the abrasion tests were derived from oil sands stripped of bitumen being solely the quartz components of oil sand. This is assumed approximate as the predominant abrasive media in oil sand is the hard quartz particles occupying the largest proportion of the total solids (Llewellyn, 1997). The size distribution for the sand is shown in Figure 5-3, where 100% of particles passed 2000 μm (No.10 U.S Standard Sieve) and nearly 80% pass 850 μm (No.20 U.S Standard Sieve). The sub-angular particles are loose and totally dried (Figure 5-4).

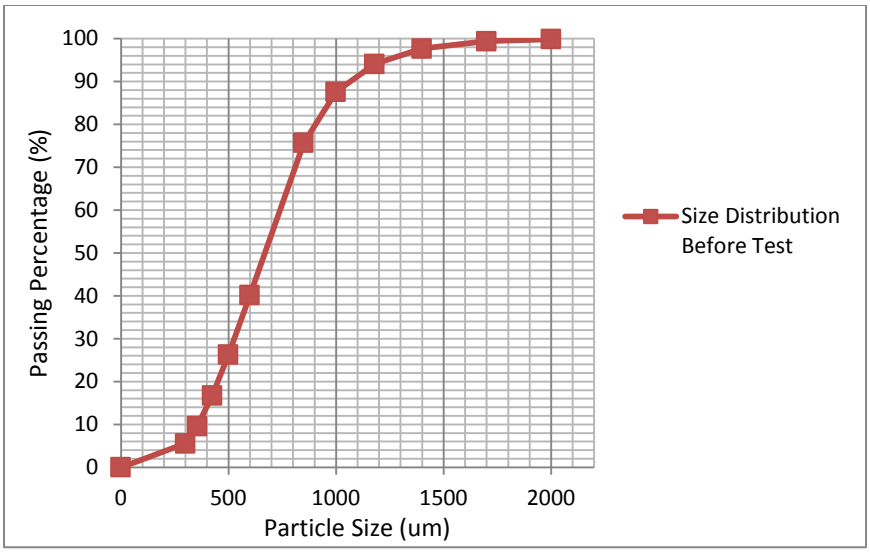

Figure 5-3: Grain size distribution of tested sands in MRWAT

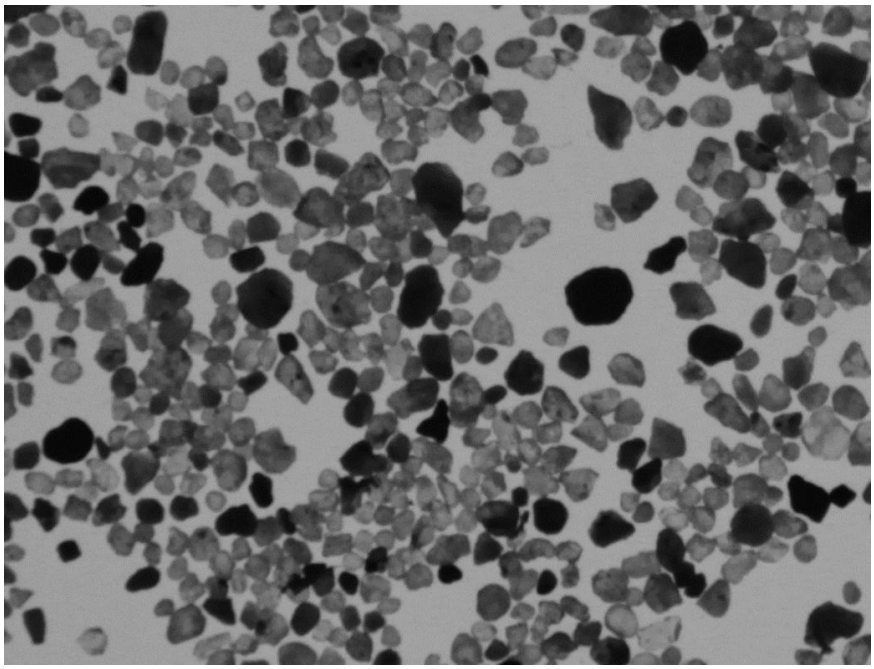

Figure 5-4: Shape of abrasive media used in MRWAT

Time and Flow Rate

As discussed previously, specific energy is defined as the friction energy experienced to volume loss of materials or the friction power experienced to volume loss rate; such that

specific energy is normalized with respect to time and any change of time has no influence on it. However; measurements in a short time leads to inaccurate estimation of volume loss; while long time duration measurement may be likely time consuming. In other words, test duration of 4 minutes was selected although this is somewhat as arbitrary decision. The flow rate of the abrasive media was matches to the rotation speed of the wheel so as clearly mimic the actual abrasive conditions.

5.4 Abrasion Test Procedure

The procedure for MRWAT is similar to that of the standard ASTM G65:

1. Clean the metal specimen and weigh with a precision to 0.0001g.
2. Place the specimen in the holder and add the specified weights to the lever arm.
3. Set the prescribed rotation speed.
4. Load the field representative abrasive media to the hopper and ensure establishment of a steady flow.
5. Start the wheel rotation, while lowering the lever arm to position the specimen against the rubber wheel.
6. Record the start time. After 4 minutes lift the lever arm away from the specimen and stop the wheel revolutions.
7. Remove the specimen.
8. Clean and reweigh the specimen with the same precision.
9. Recoat the wheel with abrasive media as parts of the wheel surface are found without coverage.
10. Set up the next iterative test run.

6 Interfacial Shear Test

6.1 Introduction

The friction coefficient between the abrasive media (sand) and coupon material has the same bearing on determination of the material/media specific energy as for the abrasive media characteristics and hardness of this coupon material. Friction can be considered as equivalence to interfacial shear strength between two different materials. Measurement of the friction coefficient in this research was carried out through an interfacial shear test (IST) developed using a conventional direct shear test system.

6.2 Interfacial Shear Test Apparatus

A schematic diagram of the interfacial shear box is shown in Figure 6-1, which follows the standard DST setup illustrated in ASTM D5321. Metal samples are placed between the upper and lower box and are fixed to the lower box with clamping crews. A photograph of the experimental setup of the IST apparatus is shown in Figure 6-2.

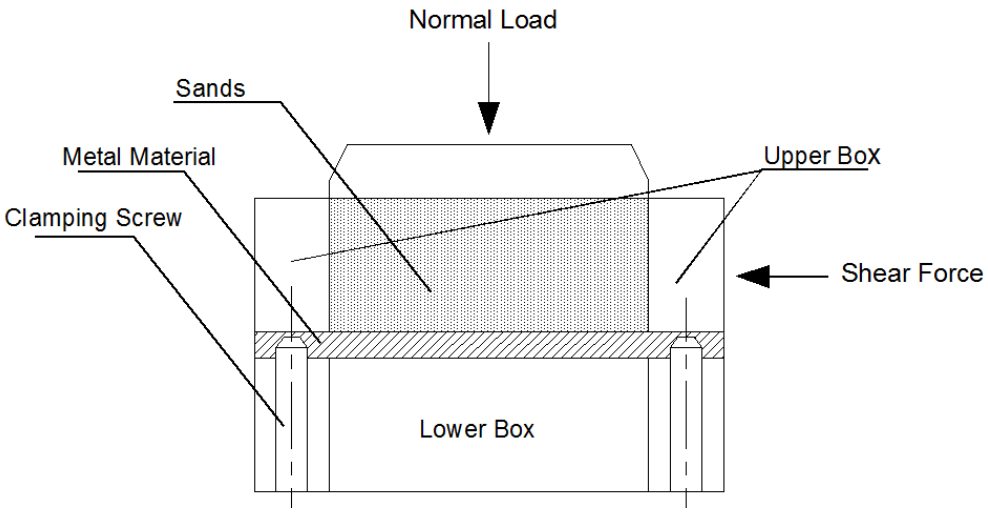

Figure 6-1: Schematic diagram of the interfacial shear box

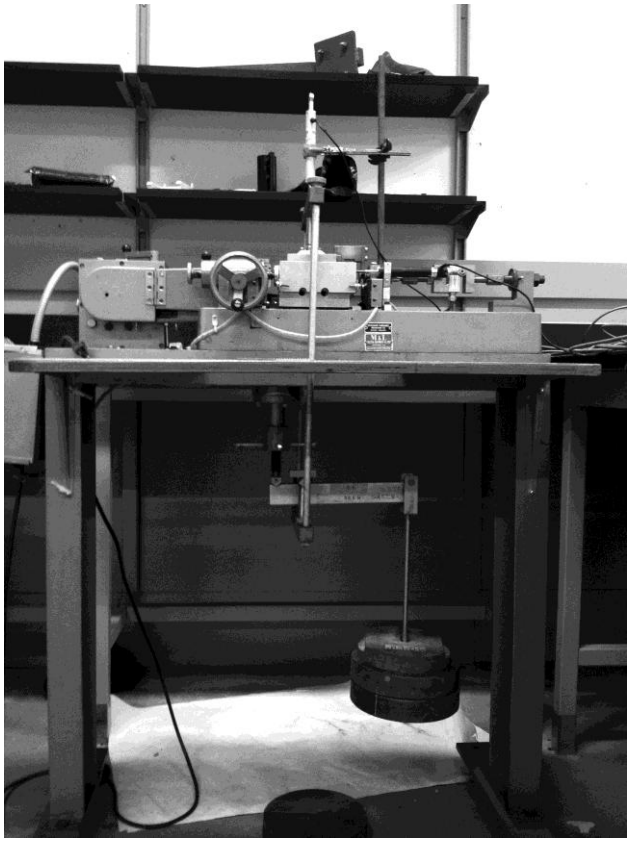

Figure 6-2: Photograph of the IST apparatus

The abrasive media used in the MRWAT were placed into the upper box, which was rigid enough as not to distort during shearing. When a shear force is applied, the upper box is moved while the lower box and the fixed material remained stationary. Contrast to the direct shear test, the shear area between the abrasive media and material remained constant at all time. The friction coefficient (the interfacial friction angle) was defined as the slope of the shear stress to normal stress plot via equation (6-1).

$$\phi_{external} = \tan^{-1}(\tau/\sigma) \quad \textbf{(6-1)}$$

Additionally, the horizontal and vertical displacements were recorded during the tests, which were analyzed to the slip mechanism.

6.3 Interfacial Shear Test Specimen and Parameters

6.3.1 Test Specimen

The interfacial shear test (IST) is an auxiliary test designed to determine the friction coefficient between abrasive media and the surface of materials used in MRWAT. Thus, the metal specimens tested in IST were the same as those used in MRWAT (Table 5-1). However sand/sand slip may accompany sand/metal slip during the shear test, giving rise to false interfacial friction angles. Brumund and Leonards (1973) demonstrated that the sand/sand slip will occur when the internal friction angle of sand was equal or less than the interfacial friction angle between the sand and material. A direct shear test was also conducted for the abrasive media without the coupon present so as to exclude the influence of sand/sand slip on the sand/material slip data.

6.3.2 Test Parameters

Normal Stress

An interfacial area is 3600 mm^2 and 4 representative normal stresses were selected: 150 kPa, 250 kPa, 350 kPa, and 450 kPa. These stresses were held constant and uniformly applied to the specimens during the tests.

Abrasive Media

The sand used in the IST was the same as those adopted in the MRWAT. Since these sands were loose and totally dried, there was no need to consider consolidation and drainage, as was the requirement of a conventional ASTM D3080.

Displacement Rate

Heerema (1979) and Lemos (1969) conducted interfacial shear tests at a displacement rate of 0.0038 mm/min to 133 mm/min and 0.7 mm/s to 600 mm/s respectively. Both

concluded that sand/steel interfacial friction was independent of velcoity. In accordance with ASTM D5321-12, the displacement rate was recommended at least 0.025 mm/min to 6.35 mm/min. In this research, 0.6 mm/min was set as the displacement rate, which is in the middle of the standard sepecificid range.

6.4 Direct Shear Test Procedure

The procedure for Metal/Sand interfacial shear test was similar to that in ASTM-D5321-12.

1. Fix the metal coupons in the lower box with screws.
2. Place the upper box into position.
3. Fill the upper box with sand, then compact until dense.
4. Apply a normal load and position the horizontal and vertical displacement LVDT.
5. Apply a shear force with the specified displacement rate.
6. Record the shear force, horizontal displacement, and vertical displacement.
7. Remove the normal stress and disassemble the device when the test is completed.

7 Results and Discussion

7.1 Nomenclature

An abbreviation was given to each metal sample: Al 63 for Aluminum 6061-T6, Al 61 for Aluminum 6061-T6, MS for mild steel A36, and SS for stainless steel 17-4 PH.

7.2 Direct Shear Test-Friction Coefficient Analysis

The relationship between shear stress and horizontal displacement for the DST is shown in Figure 7-1. For each level of normal stress, a typical curve of the dense coarse-grained sands with a peak shear stress was existed. These traces reflect that the initial sand/sand

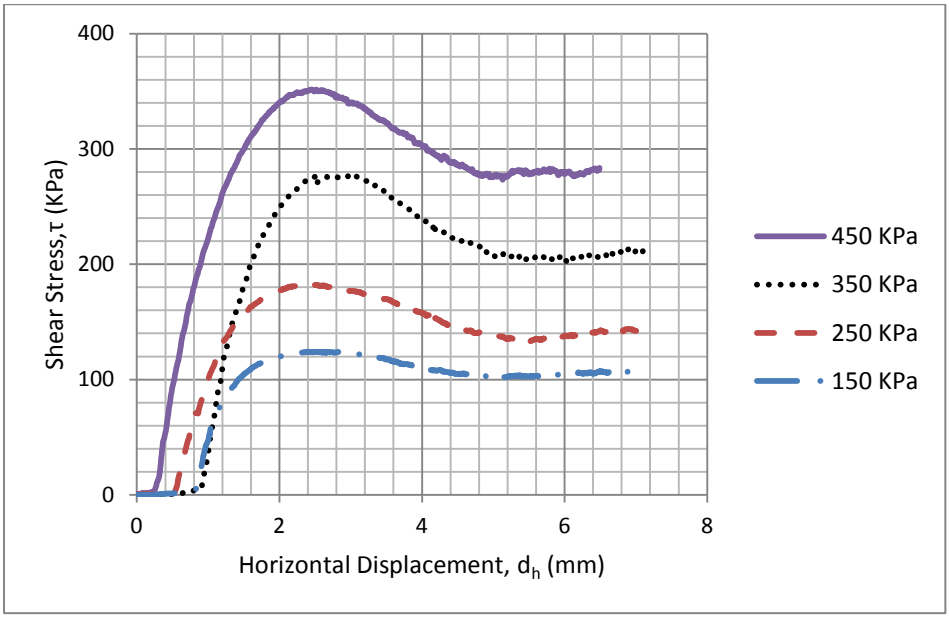

Figure 7-1: Shear stress vs. horizontal displacement relationship for sands

slip is resisted by interlocking particles. The degree of interlocking leads to an increase in apparent frictional resistance until a peak shear stress is reached. Beyond the peak stress, the interlocking is progressively overcome such that the shear stress decreases and finally reaches a residual value known as the residual shear strength. The peak shear strength is

the frictional resistance required to overcome interlocking. The residual shear strength is known as a critical state and reflects a critical friction angle which is to be considered as the internal friction angle of sand particles.

The interfacial shear test (IST) results presented in Figures 7-2 to 7-5 shows the shear stress-horizontal displacement relationship between the abrasive media and each metal sample. All metal/sand curves achieve a stable level of shear stress over large horizontal displacement. This suggests that there are few incidents of particle rearrangements (interlocking between particles) occurring during the IST, which in turn shows that slippage between sand particles is unlikely to occur with the interfacial sand/metal motions.

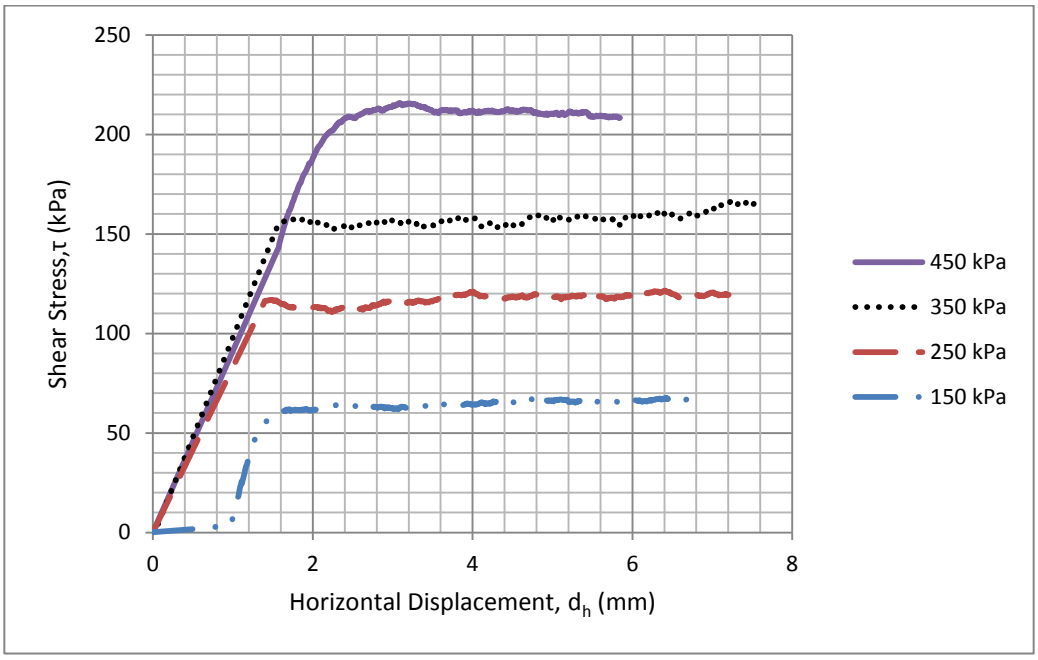

Figure 7-2: Shear stress vs. horizontal displacement relationship between sand and Al61

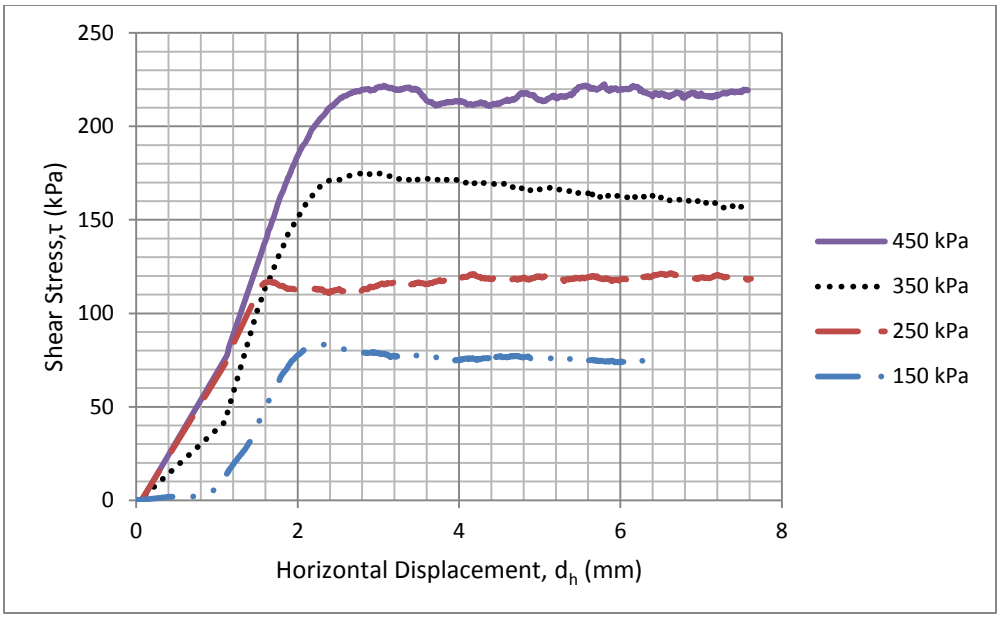

Figure 7-3: Shear stress vs. horizontal displacement relationship between sand and Al63

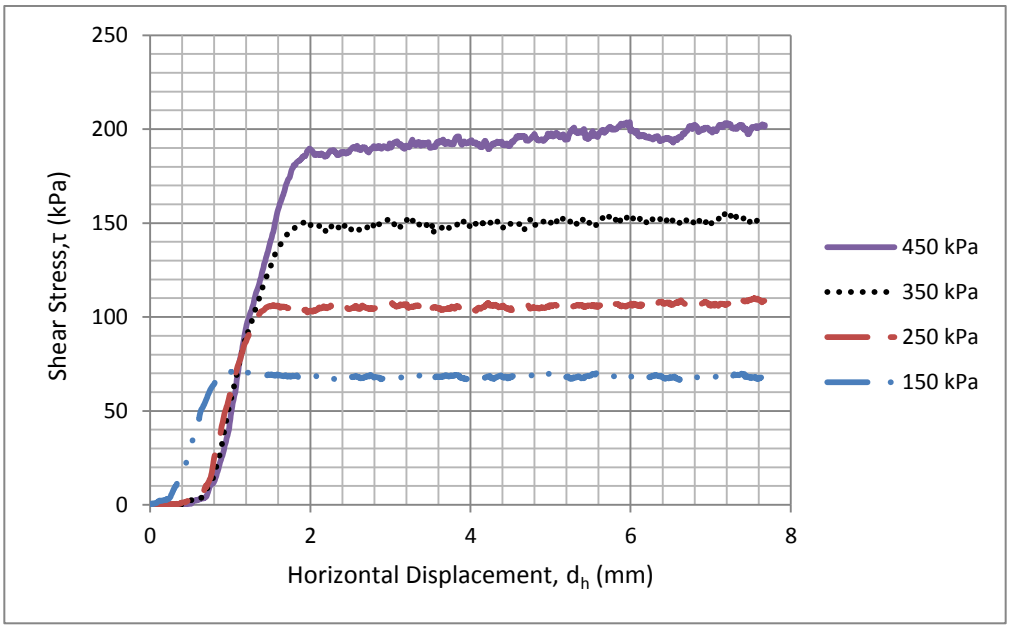

Figure 7-4: Shear stress vs. horizontal displacement relationship between sand and MS

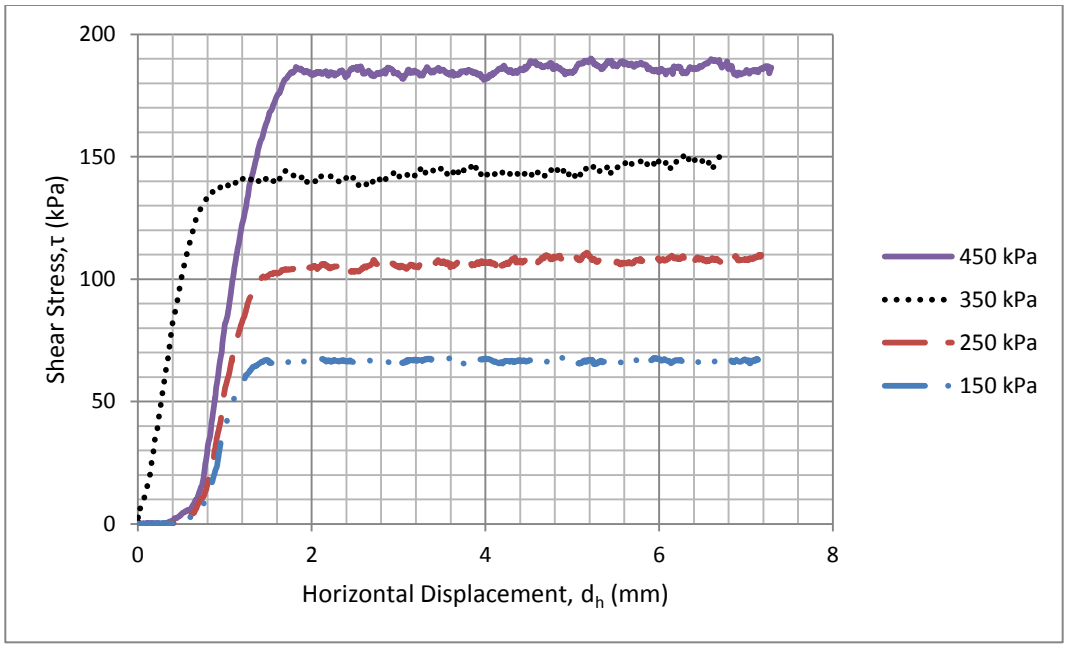

Figure 7-5: Shear stress vs. horizontal displacement relationship between sand and SS

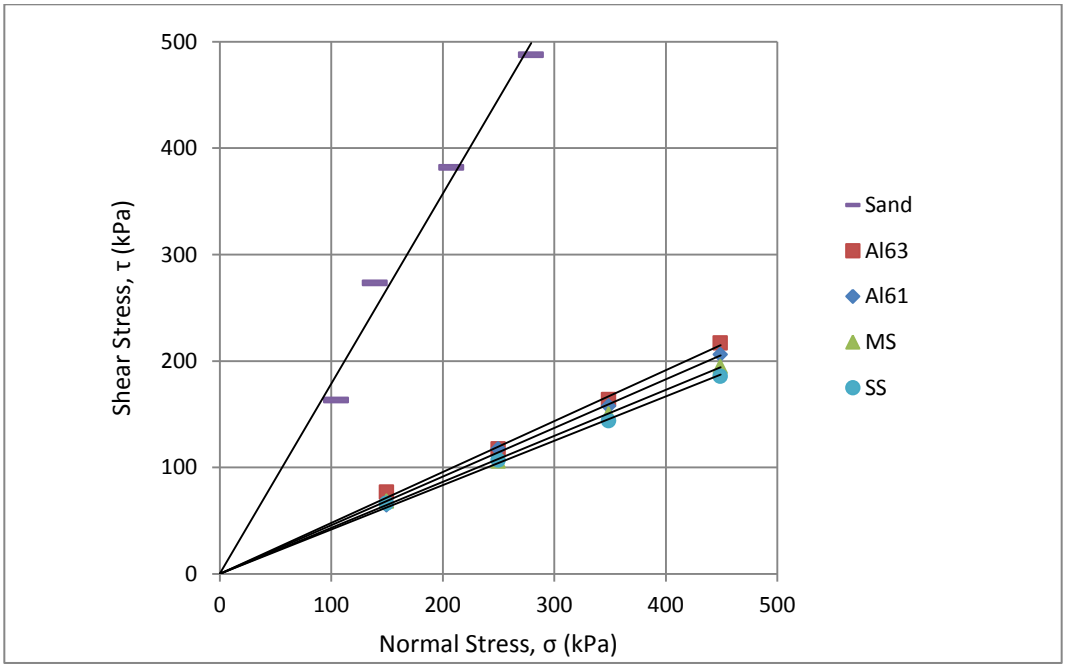

Figure 7-6: The relationship between residual shear stress vs. normal stress

The shear versus normal behaviour (τ-σ plot) is shown in Figure 7-6. It can be seen that for all shear tests conducted there is a highly credible linear relationship between shear and normal stress. All the τ-σ correlations pass through the origin such that there is no cohesion, which is in accordance with the characteristics of sands and the behaviour of interfacial slides. The slope of sand-sand test is much higher than that of any sand-metal test as would be expected. The friction angles corresponding to each slope are given in Table 7-1.

Table 7-1: Comparison of internal friction angle and each interfacial friction angle

Test	**Correlation Coefficient** (R^2)	**Friction Angle** (Degree)
Sand	0.98	60.7
Sand-Al63	1	25.6
Sand-Al61	1	24.6
Sand-MS	1	23.4
Sand-SS	1	22.6

It can be seen that all interfacial friction angles are much less than the internal friction angle of sand, which implies the interfacial shear stress is not large enough to overcome the internal frictional resistance to rearrangement of sand particles. That is, the interfacial sand-metal slip will accompany the internal slippage of the sands. In terms of interfacial angles, a slight trend to decrease with increase in hardness of material was observed. This behavior is attributed to the degree of indentation of interfacial particles on a material surface. A harder material surface would effectively resist the plowing of angular particles, giving rise to small interfacial frictional resistance as well as small friction angles.

The plot of volumetric strain versus horizontal strain is shown in Figure 7-7. The dilatancy represented by the volumetric strain in the IST is smaller than the dilatancy in the DST. This is due to the rearrangement of particles near an interface surface rather than the interlocking of sand particles during the IST (Frost and Han, 1999). Angular sands near the interface surface will penetrate and plow along the contact surface under application of shear stress and normal load. Due to the roughness of material surface, these interfacial particles move up or overcome the rough surface asperities, leading to dilation adjacent to interface surface. This is however, smaller than the dilation caused by the sand-sand test.

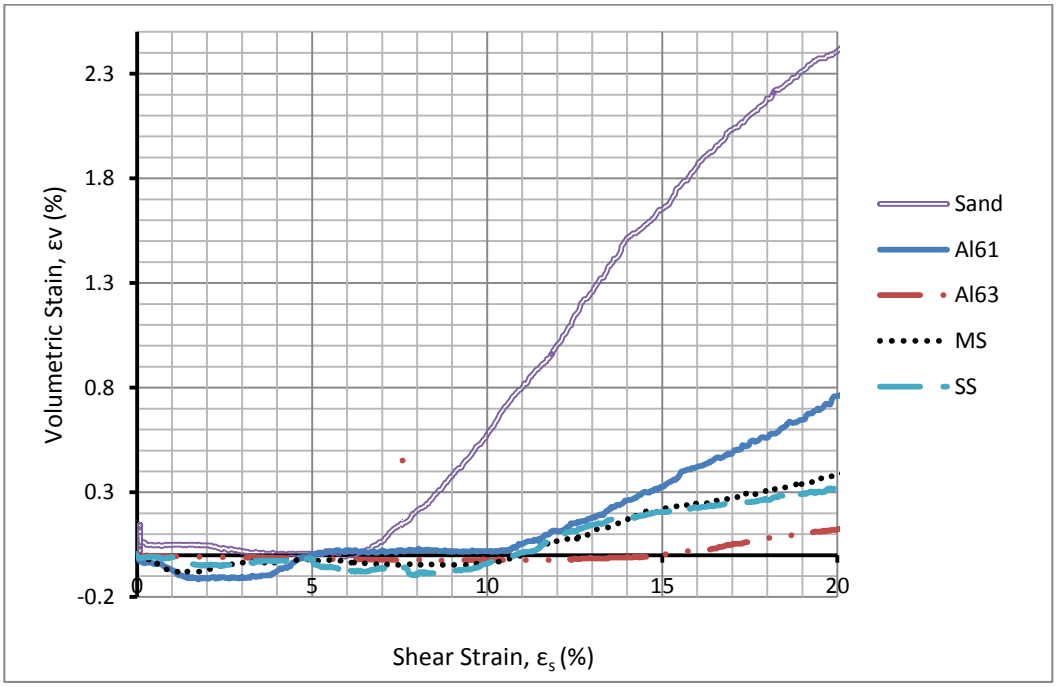

Figure 7-7: Relationship between volumetric strain and shear strain (normal stress 450 kPa)

The interfacial slippage mechanism can be summarized as follows: under onset of an applied normal load and shear load, both the internal sand/sand contacts and the interfacial sand/metal contacts are subjected to deformation. However, because interfacial

friction angles are much less than internal friction angles, shear forces must first increase to a critical sand/metal slip condition, to permit driving the interfacial sand over the metal surface. Once the relative motion between the sand and metal commences, the shear force will remain stable, meaning internal sand/sand contacts are only subjected to deformation with little occurrence of slippage. As a result the shear stress in the IST is primarily influenced by the interfacial resistance, and it is unrelated to the internal resistance between sand/sand contacts. The interfacial friction angle obtained from the IST can be considered as the skin friction angle between the abrasive media and material.

7.3 Modified Rubber Wheel Abrasion Test

7.3.1 Size distribution

The grain size distribution before and after the abrasion tests is shown in Figure 7-8. Even though the post-test curve shows a small decrease in particle size, there is no significant difference.

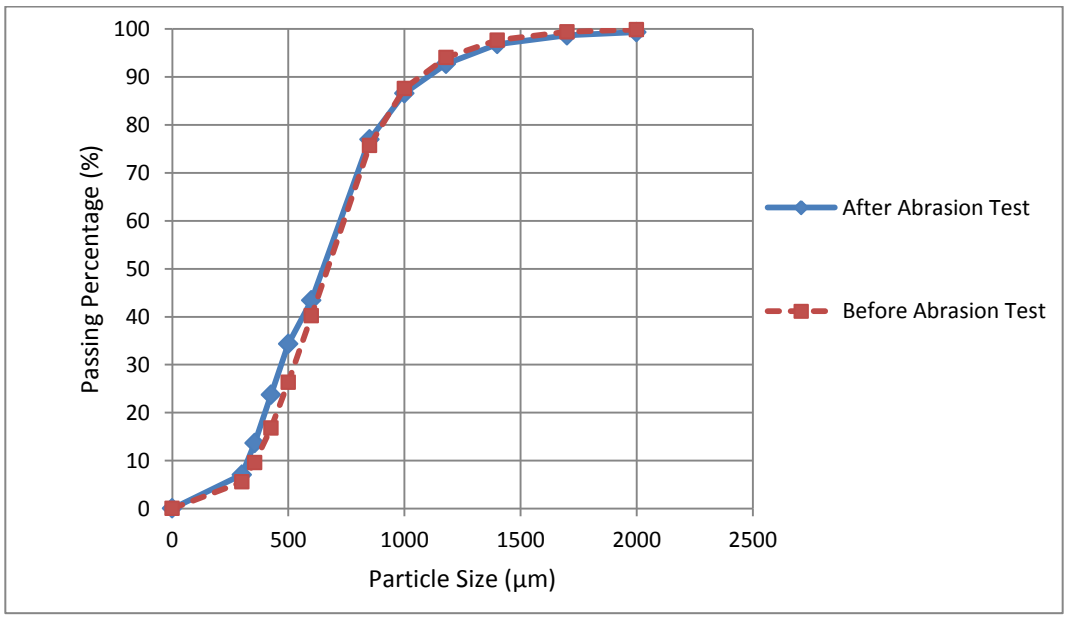

Figure 7-8: Comparison of grain size distribution

Both curves show a 80% particles pass 850 μm. This behaviour is attributed to the low contact stresses applied between the rubber wheel and metal samples, allowing abrasive media to penetrate and slide over a surface but not sufficient to crush particles. The application of a rubber wheel instead of a steel wheel also precludes occurrence of particle breakage (Lafleur, 2011). Therefore it can be assumed that the majority of friction energy translates into abrasive wear of the material tested in the MRWAT.

7.3.2 Abrasion test results

The modified rubber wheel abrasion test was designed to measure specific energy of materials in the mimic abrasive condition that happened to shovel teeth working in oil sands. From $V/t = (1/E_S) \cdot \mu Fv$ (equation (3-8)) the specific energy is seen equal to the reciprocal value of the slope of a volume loss rate verses friction power relationship. The test results for four metals are presented from Figure 7-9 to Figure 7-12. For all materials tested there is a strong linear relationship between volume loss rate and friction power, with the smallest correlation coefficient of 0.97.

The hardness, friction coefficient, and specific energy of each material tested are summarized in Table 7-2. Hardness is defined as the mean pressure to cause materials to undergo a plastic deformation. The harder the material, the lower deformation of the materials under the same stress. The Vickers hardness number can be converted to units of pressure (MPa) by multiplying 9.81.

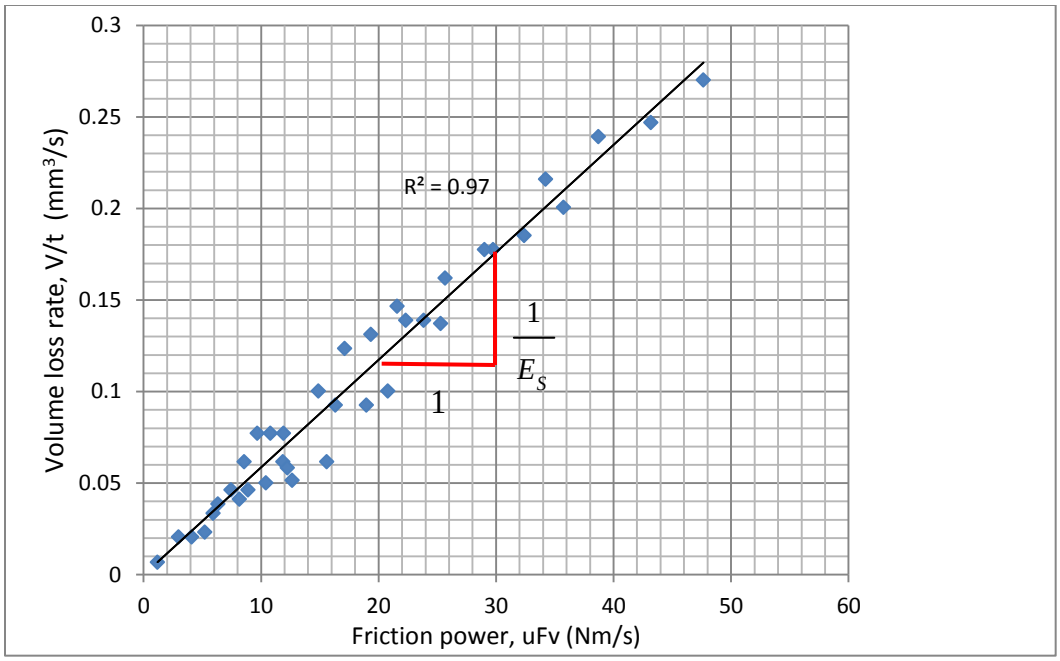

Figure 7-9: Relationship between volume loss rate and friction power for Al 61

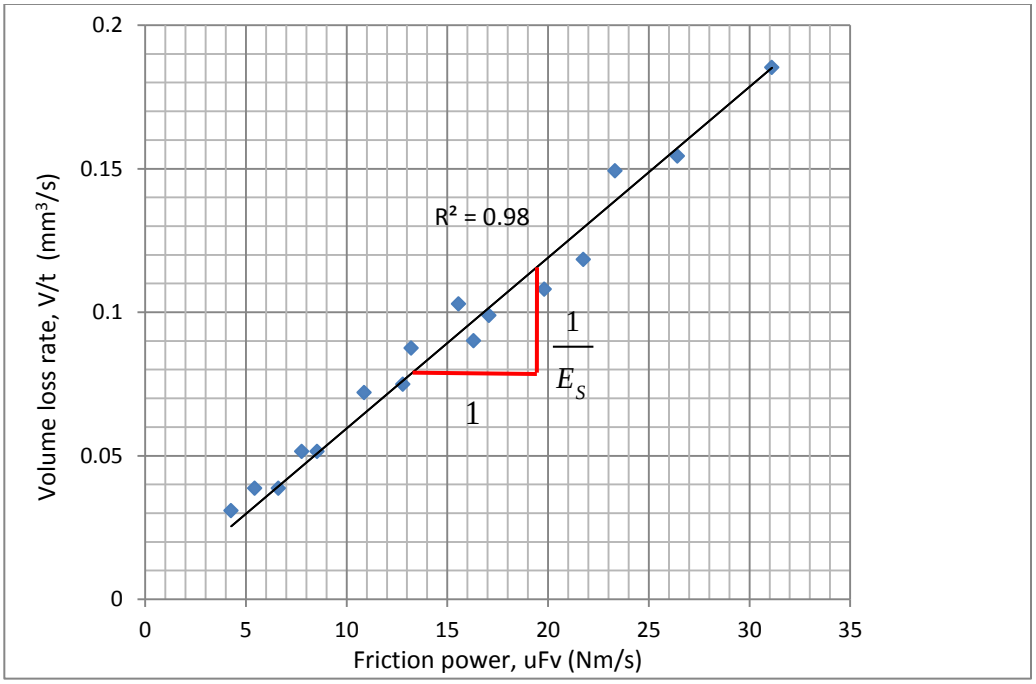

Figure 7-10: Relationship between volume loss rate and friction power for Al 63

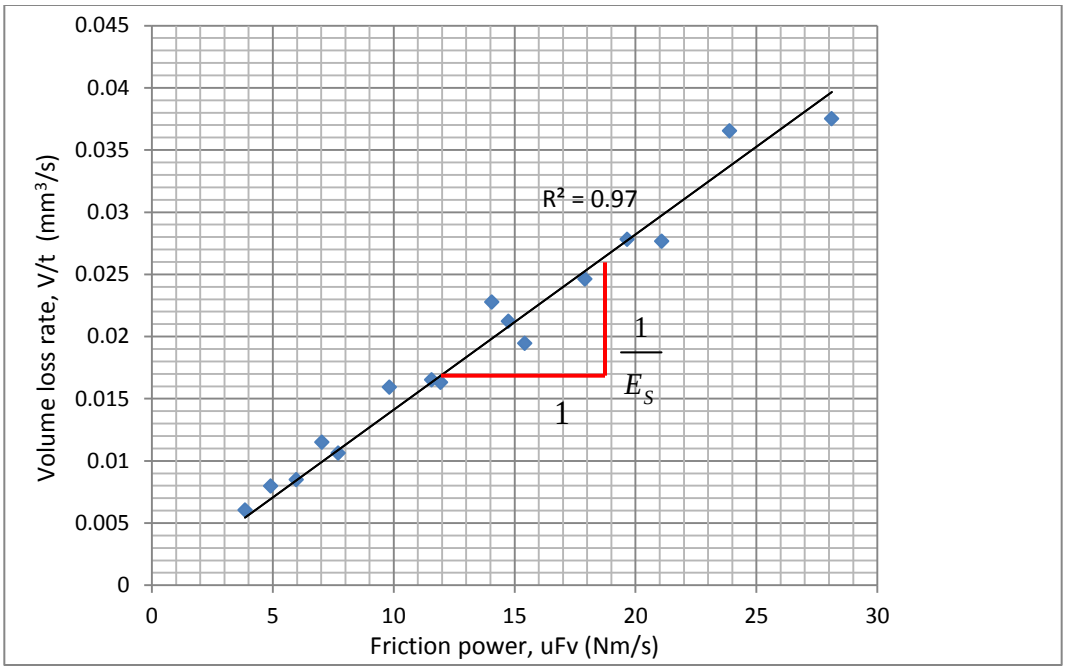

Figure 7-11: Relationship between volume loss rate and friction power for MS

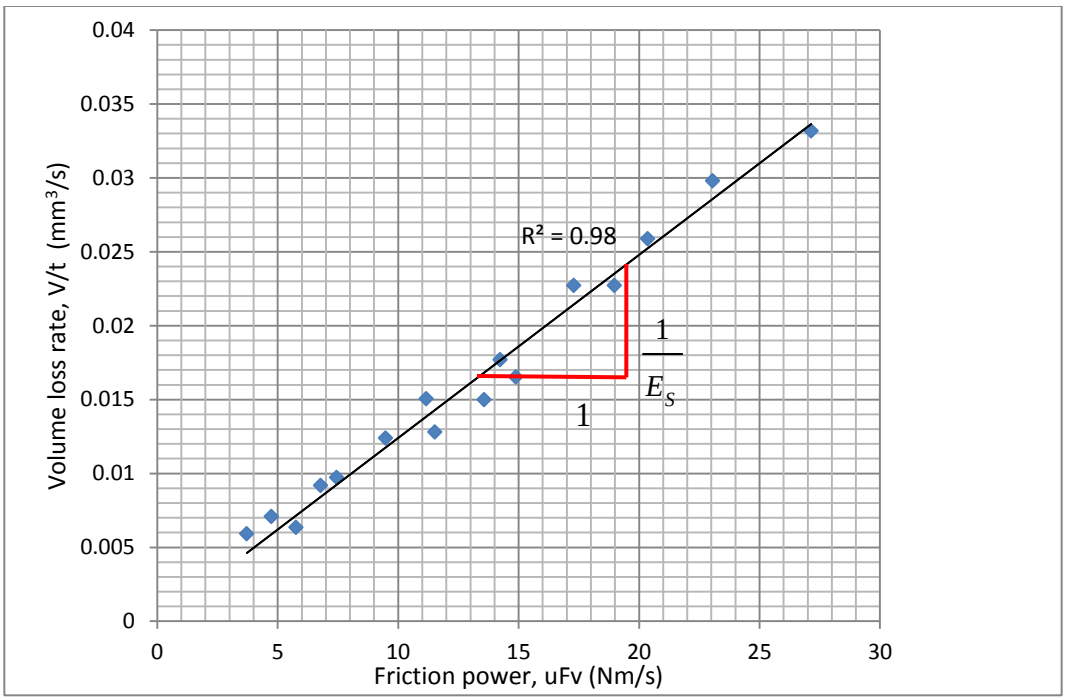

Figure 7-12: Relationship between volume loss rate and friction power for SS

Table 7-2: Hardness, friction coefficient, and specific energy of each material tested

Material	Hardness	Hv Number	Hardness Pressure (MPa)	Friction Coefficient	Es ($\times 10^2$ GPa)
Al 63	Very Soft	83	814	0.48	1.69
Al 61	Soft	107	1050	0.46	1.70
MS	Medium Hard	213	2090	0.43	7.09
SS	Hard	279	2737	0.42	8.07

From Table 7-2 it can be seen that specific energy increases with increasing hardness of materials. For example the specific energy of medium hard stainless steel is roughly 5 times than that of very soft Al63. In accordance with the definition of specific energy, such that friction energy causes a unit volume loss, soft materials with low specific energy require lower friction energy to cause the same volume loss as hard materials. Namely soft materials are much easily worn out. Therefore the specific energy can be used to rank resistance of materials to abrasive wear under the same abrasive conditions.

7.3.3 Specific energy vs. scale factor

Since specific energy is that ratio of friction energy to its corresponding volume loss, an increase in volume loss caused by greater applied force or higher velocity in effect results from a rise in friction energy. Regardless of the change in force and velocity, the specific energy for a pure material can be considered as a constant. That is, specific energy is independent of scaling. In MRWAT, only normal forces were scaled while other parameters keep the same values as the filed data. According to Equation $E_S = E/V = (F/V)\cdot \mu vt$, the scale force (F) in an abrasion test is the major factor bringing about the volume loss (V) which is also scaled as follows:

$$F_{actual} = \left(\frac{\sqrt[3]{F_{actual}}}{SF} \right)^3 = \frac{F_{actual}}{SF^3}$$
$$V_{scale} = \left(\frac{\sqrt[3]{V_{actual}}}{SF} \right)^3 = \frac{V_{actual}}{SF^3} \qquad \textbf{(7-1)}$$

Substituting equation (7-1) into $E_S = E/V = F/V \cdot vt$, then:

$$E_{S(scale)} = \frac{F_{scale}\ \cancel{\mu vt}}{V_{scale}\ \cancel{\mu vt}} = \frac{F_{actual}/\cancel{SF^3}}{V_{actual}/\cancel{SF^3}} = \frac{F_{actual}}{V_{actual}} = E_{S(actual)} \qquad \textbf{(7-2)}$$

Such that:

$$E_{S(\text{scale})} = E_{S(actual)} \qquad \textbf{(7-3)}$$

Equation (7-3) illustrates that the specific energy is independent of scaling. Derived from a typical abrasive model, the specific energy formula ($E_S = \frac{\pi \mu H \tan\theta}{2A}$, equation (3-7)) also demonstrates that *Es* is not influenced by scale factors, and it is merely determined by material hardness (*H*), particle size (*A*), particle angularity (θ), and contact condition (μ), The particle size, particle angularity, and contact condition are collectively named as the abrasive conditions. The specific energy in effect may be regarded as an index reflecting performance of a material with hardness (*H*) working under a specific abrasive conditions characterized by particle size (*A*), particle angularity (θ), and contact condition (μ).

7.3.4 Specific Energy vs. Friction

The relationship between specific energy and friction is a major interest in verifying the specific energy as an independent abrasion index. The abrasion function ($V/t = (1/E_s)\cdot \mu F v$, equation (3-8)) illustrates that the volume loss rate (V/t) is a bivariate function of friction (μF) and velocity (v) while specific energy (Es) acts as a function coefficient. When the variable μF is fixed, it essentially exists as a linear relationship between V/t and v with a slope of $\mu F/Es$.

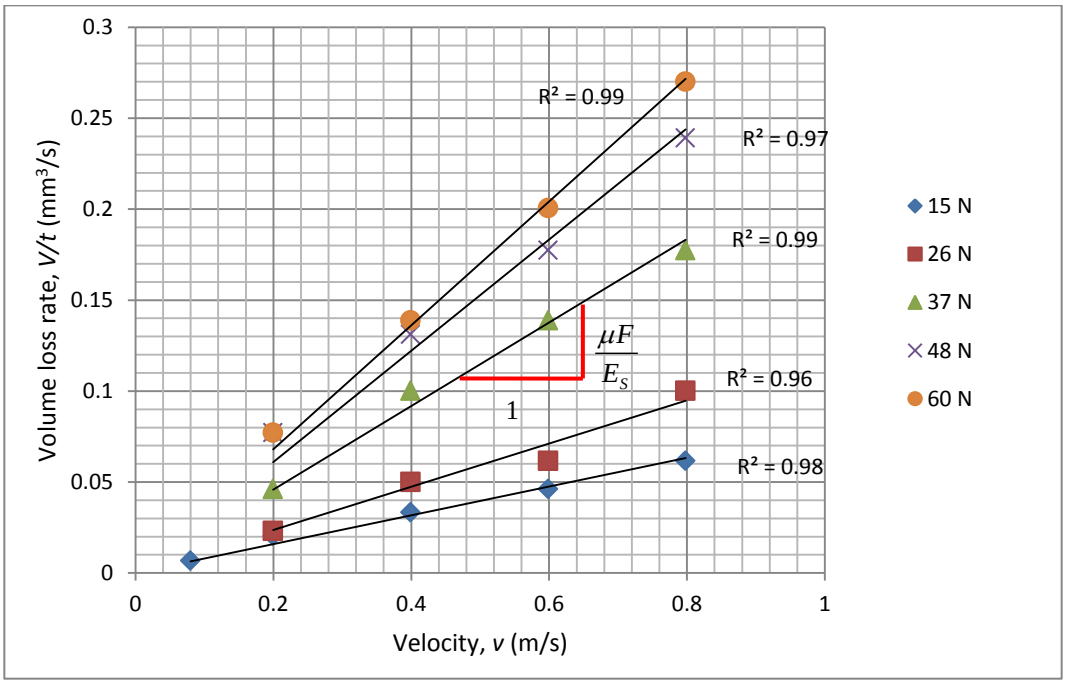

Figure 7-13: Volume loss rate versus velocity for Al61

Figure 7-13 provides the relationship between volume loss rate (V/t) and velocity (v) for Al61. There always exists an obvious linear relationship between volume loss rate (V/t) and velocity (v) regardless of friction level. In accordance with the abrasion function ($V/t = (\mu F/E_s)\cdot v$, equation (3-8)), $\mu F/Es$ is a slope of the V/t versus v plot. In Figure 7-13 the slope of the V/t versus v plot ($\mu F/Es$) becomes increasingly steeper with

increasing friction (μF), which implies that μF most likely contributes to the increase in slope ($\mu F/Es$). In order to further study the relationship between $\mu F/Es$ and μF, the graph of $\mu F/Es$ versus μF for material Al61 is given in Figure 7-14. Here a linear relationship between $\mu F/Es$ and μF illustrates that an increase in $\mu F/Es$ is attributed to the growth of friction (μF). The specific energy (Es) remains constant and its reciprocal value ($1/Es$) serves as the slope of $\mu F/Es$ versus μF plot.

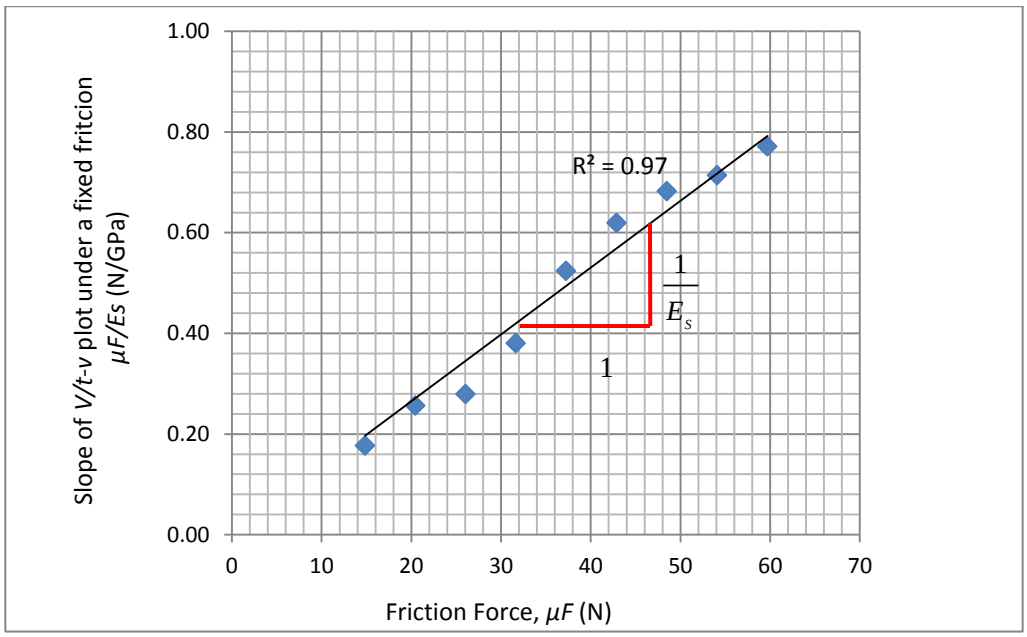

Figure 7-14: Relationship between slope of *V/t* versus *v* plot ($\mu F/Es$) and friction (μF) for Al61

The $\mu F/Es$ versus μF behaviour for Al63, MS, and SS are also depicted in Figure 7-15. Here a significant linear relationship between $\mu F/Es$ and μF exibits for all materials tested, suggesting a change in $\mu F/Es$ results from friction (μF), while specific energy (Es) remains.

Figure 7-16 shows that the μF/Es versus μF plot for Al63 has the steepest slope. This phenomenon is considered due to the different specific energy of materials; such that

Al63 being the softest material with the lowest specific energy, MS is the second with medium specific energy, and SS is the hardest with largest specific energy. If friction is constant, the value of $\mu F/Es$ for the softest material Al63 will be largest, making its $\mu F/Es$ versus μF slope steepest. The value of $1/Es$ is equal to the slope of $\mu F/Es$ versus μF plot, such that the higher specific energy (E_S), the lower $1/Es$, and the gentler the $\mu F/Es$ versus μF slope.

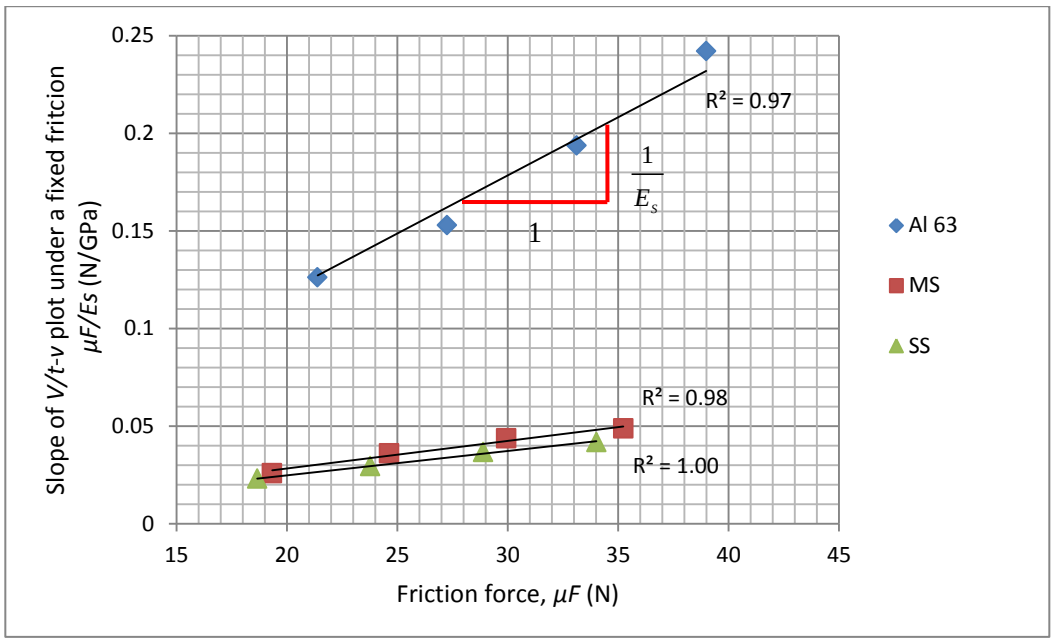

Figure 7-15: Relationship between slope of *V/t* versus *v* plot ($\mu F/Es$) and friction (μF) for Al63, MS, and SS

The graph of specific energy versus friction for Al61 is given in Figure 7-16. Even though specific energy under different frictions varies, they are distributed around a relatively constant value of specific energy. From the perspective of statistics the Critical Pearson' Correlation Coefficient (R, the square root of correlation coefficient R^2) for 9 samples in a 95% confidence level is 0.67. The Pearson' Correlation Coefficient R here is

0.57 which is less than 0.67, suggesting no significant relationship between specific energy and friction.

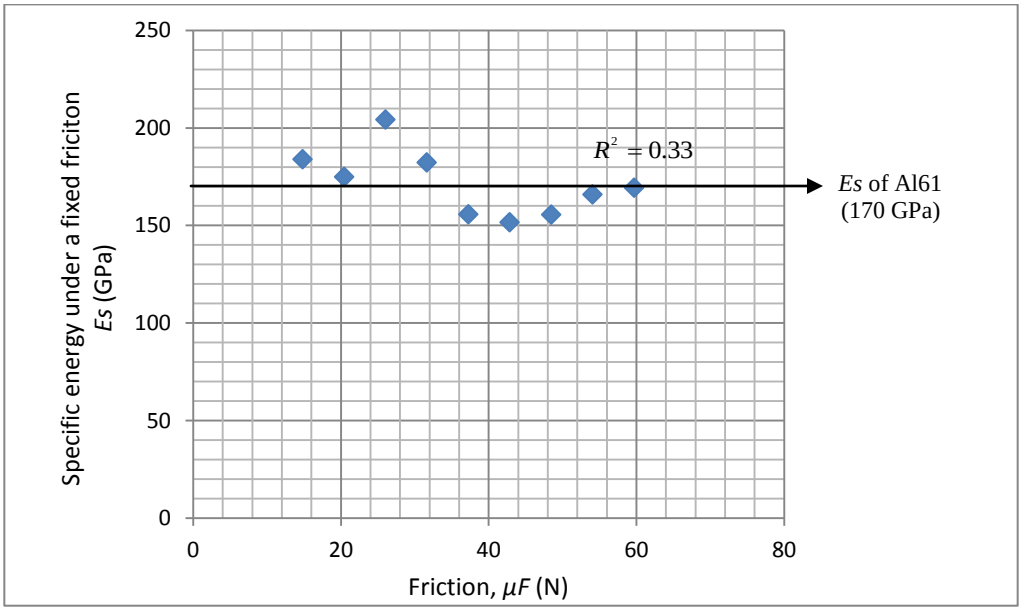

Figure 7-16: Specific energy vs. friction for Al61

This no significance between specific energy and friction is also seen for other all metals tested (Figure 7-17). All specific energy points for each material are distributed around its constant value. The sample sizes in Figure 7-17 are 4 for a critical Pearson' value (*R*) for 95% confidence level of 0.95. In Figure 7-17 even the highest Pearson value (*R*) is 0.59, which is much less than the critical value, suggesting specific energies for Al 63, MS, and SS are unrelated to friction.

As the specific energy is a ratio of the friction energy input to the corresponding volume loss, an increase in friction would merely result in a rise in friction energy, which would accelerate volume loss. However the ratio of increasing friction to increasing volume loss

remains constant; therefore specific energy is unchanged, it could be considered independent of friction.

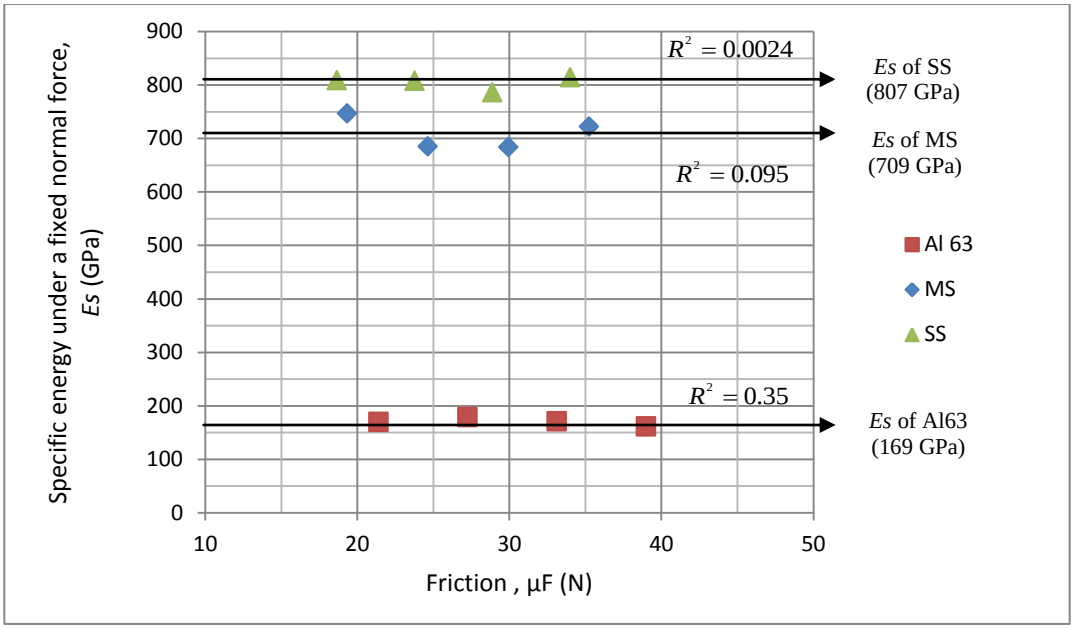

Figure 7-17: Specific energy versus friction for Al63, MS, and SS

7.3.5 Specific Energy vs. Velocity

Another focus is the relationship between specific energy and velocity. Based on the abrasion function ($V/t = (1/E_S)\cdot \mu F v$, equation (3-8)), one variable of volume loss rate (V/t) is velocity (v) and the other is friction (μF). When the velocity (v) is fixed, the volume loss rate (V/t) should be a univariate function of friction (μF) with a coefficient (v/Es). Figure 7-18 yields linear relationships between volume loss rate (V/t) and friction (μF) for Al61 when the velocity is fixed. The correlation coefficient (R^2) for low velocity is smaller than that at high velocity. This behaviour can be explained in terms of particle motion under different wheel speeds. When the speed is low, the particles are most likely to be retained between the wheel and samples, leading to a lots of friction energy, since there is no sufficient shear force to cause the particle to slide over surface. However at high speeds, particles are rejected from contact areas, inducing lower mass loss of

samples. There is an appropriate speed range under which good linear behaviours between volume loss rate and friction can be seen.

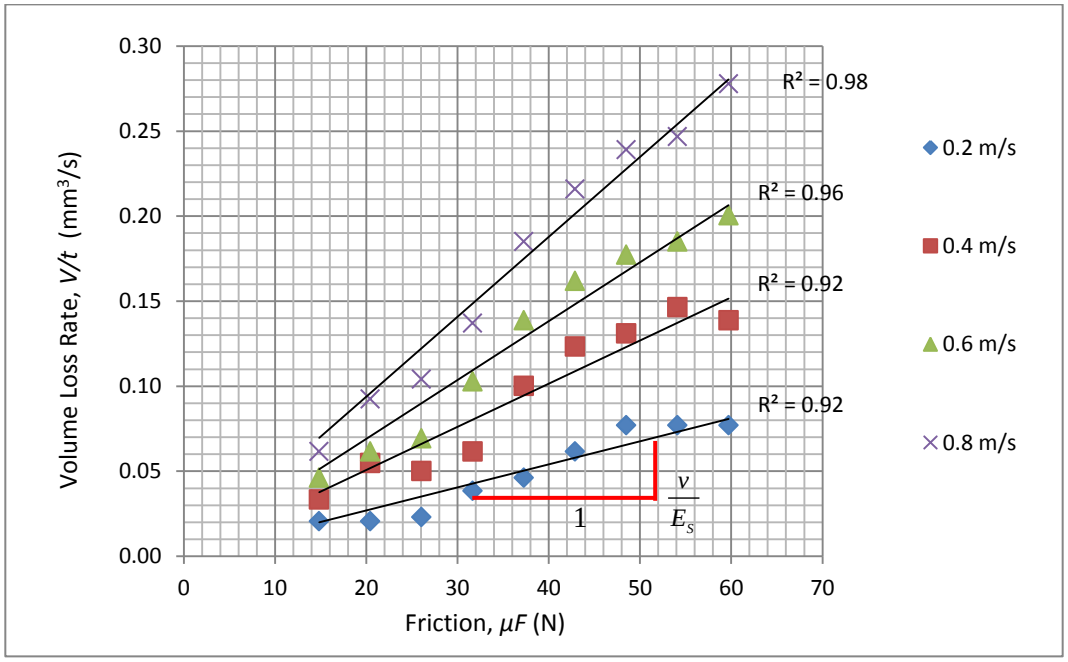

Figure 7-18: Volume loss rate versus friction for Al 61

In Figure 7-18 *v/Es* is the slope of *V/t* versus μF relationship which increases with increasing velocity (*v*), suggesting that increase in *v* results in increasing *v/Es*, while specific energy has no influence on *v/Es*. The graph of *v/Es* versus *v* for Al61 is given in Figure 7-19, where it can be seen that *v/Es* is a linear function of velocity (*v*) with a slope of *1/Es*, which proves that specific energy remains constant regardless of change in velocity. A similar linear behaviour exists between *V/t* and μF which was also shown for the other tested materials, including Al63, MS, and SS (Figure 7-20). Here the specific energy for each material seems unrelated to velocity. It is evident that the *v/Es* versus *v* relationship for the Al63 had a steeper slope than that for other hard materials. This phenomenon was due to the presence of a different specific energy relative to the materials tested.

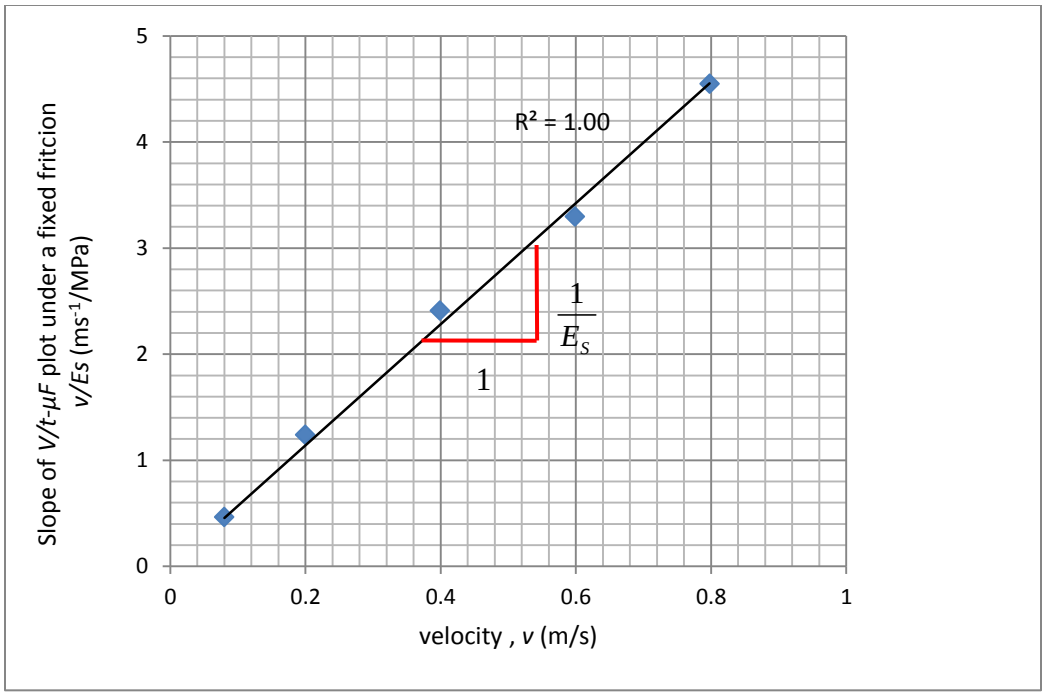

Figure 7-19: Relationship between slope of *V/t* versus *μF* plot (*v/Es*) and velocity (*v*) for Al61

In order to visually illustrate that specific energy is independent of velocity, the *Es* versus *v* plot for Al61 is shown in Figure 7-21. The specific energy by velocity is effectively steady at a constant value of specific energy. According to a critical value for Pearson' correlation (*R*) for a sample size of 5, the critical value 95% confidence is 0.88. The *R*-value here is 0.57, which is much smaller than 0.88, confirming no significant relationship between specific energy and velocity. Specific energy is independent of velocity. For the other materials tested, including Al63, mild steel, and stainless steel, this independence is also clarified (Figure 7-22).

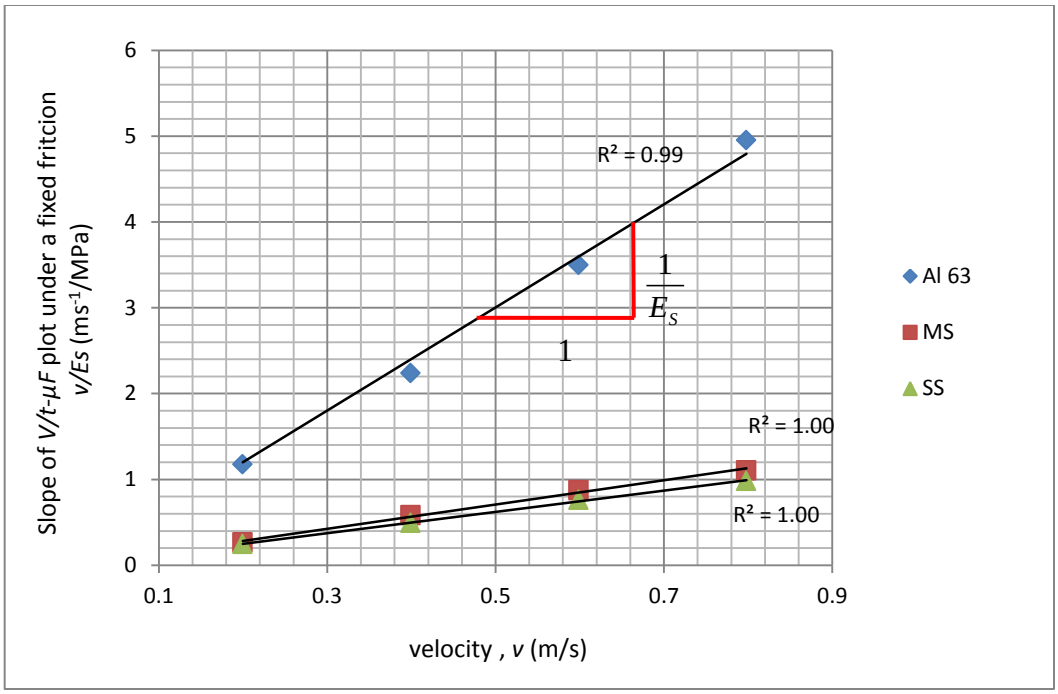

Figure 7-20: Relationship between slope of *V/t* versus *μF* plot (*v/Es*) and velocity (*v*) for Al63, MS, and SS

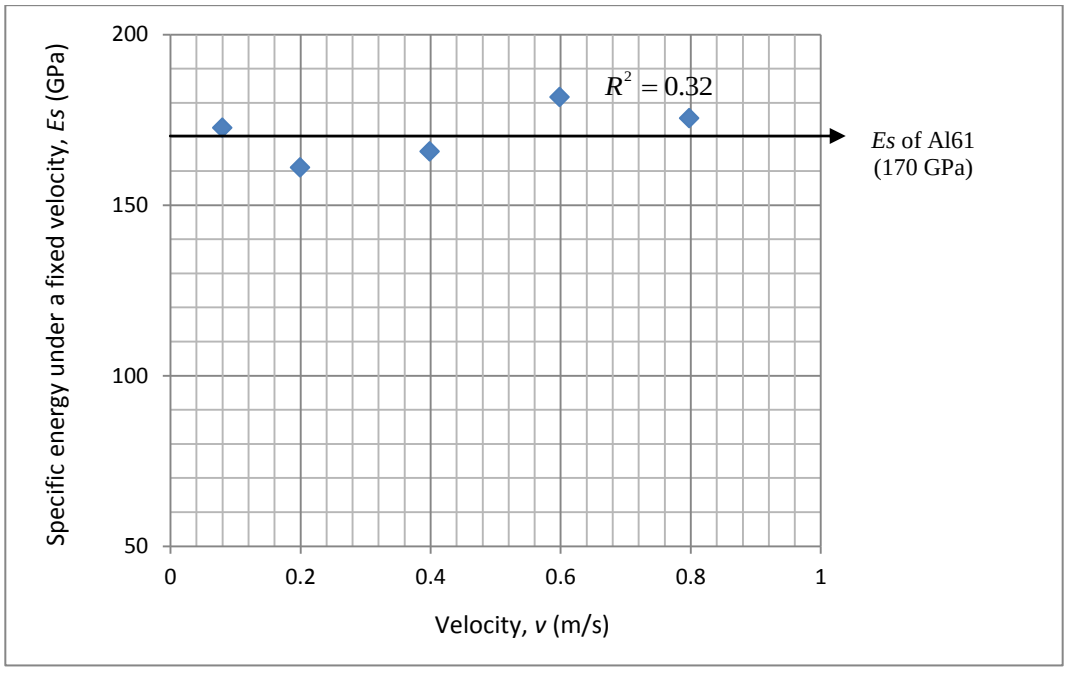

Figure 7-21: Specific energy versus velocity for Al 61

Alike to influence of friction on abrasion, an increase in velocity results in an increase in both friction energy input and the corresponding volume loss. However, the ratio of increasing friction energy to its increasing volume loss seems to remain unchanged. As a result specific energy can be regarded as an index which is independent of velocity.

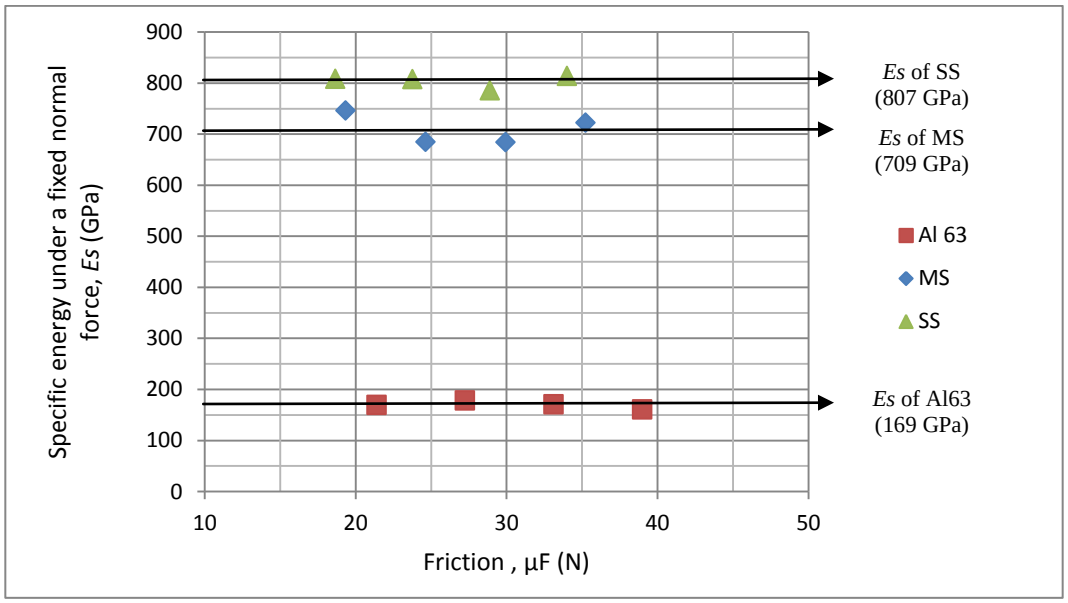

Figure 7-22: Specific energy versus velocity for Al63, MS, and SS

7.3.6 Abrasion Function

Since specific energy (*Es*) is independent of velocity and friction, the formula $V/t = (1/E_s)\mu Fv$ (equation (3-8)) may be considered as an abrasion function. When the specific energy and friction coefficient are known, the volume loss rate of material is a bivariate function of normal force and velocity. Figure 7-23 shows the relationship for volume loss rate, normal force, and velocity with respect to mild steels commonly used to manufacture shovel teeth. It can be seen that the volume loss rate increases with increase in normal force or velocity. The faster the velocity or the greater the normal force, the larger the volume loss rate.

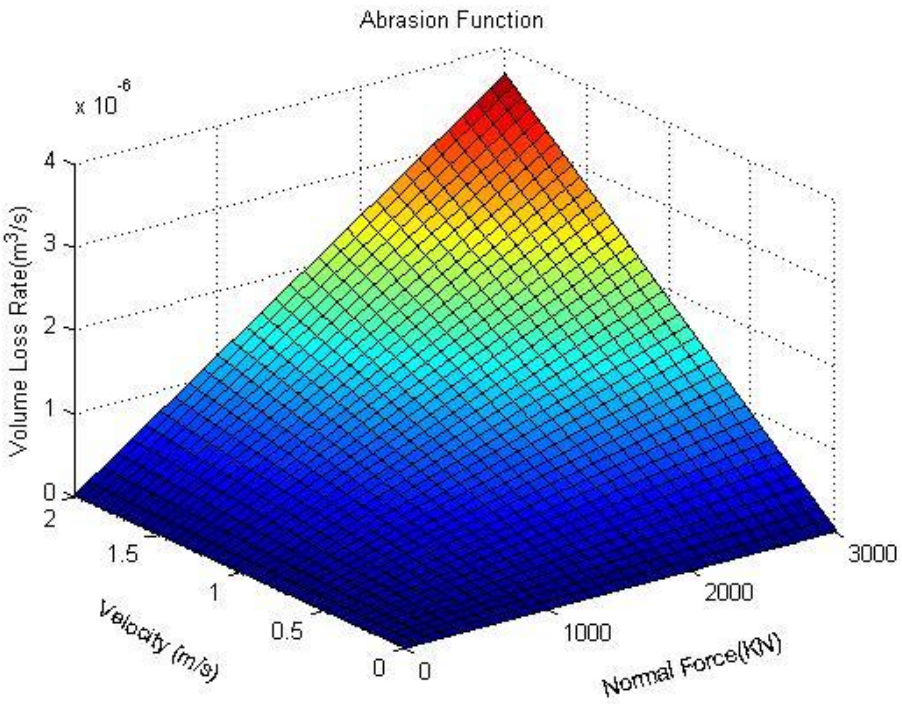

Figure 7-23: 3-D Graph of normal force versus velocity versus volume loss rate for Mild Steel (μ=0.43)

In the case of shovel teeth, even though there is no optimal combination of force and velocity, abrasive wear can still be effectively reduced when both digging velocity and hoist force are at low level. Practically, cable shovels are suggested for operating at high hoist forces but low digging velocities to keep production up, while decreasing abrasive wear on ground engaging tools.

7.4 Verification of Specific Energy

7.4.1 Specific energy vs. hardness

In accordance with $E_S = (\pi\mu H \tan\theta)/(2A)$ (equation (3-7)), when the particle characteristics (size coefficient A and shape parameter θ) and contact condition (friction coefficient μ) keep constant, the specific energy (Es) should be proportional to hardness (H) in the form of equation (7-4).

$$E_S = BH \tag{7-4}$$

In equation (7-4), B is named as the specific energy coefficient and is equal to $(\mu\pi \tan\theta)/(2A)$. The hardness as previously defined is the mean pressure acting on material to evoke fully plastic deformation, and its Vickers hardness number (HV) can be converted to pressure units Pascal (Table 7-2) as mentioned previously. In this thesis, all the abrasion tests were performed using the same abrasive media; such that a liner relationship between specific energy (*Es*) and hardness pressure (*H*) exists. Figure 7-24 shows the relationship between specific energy and hardness.

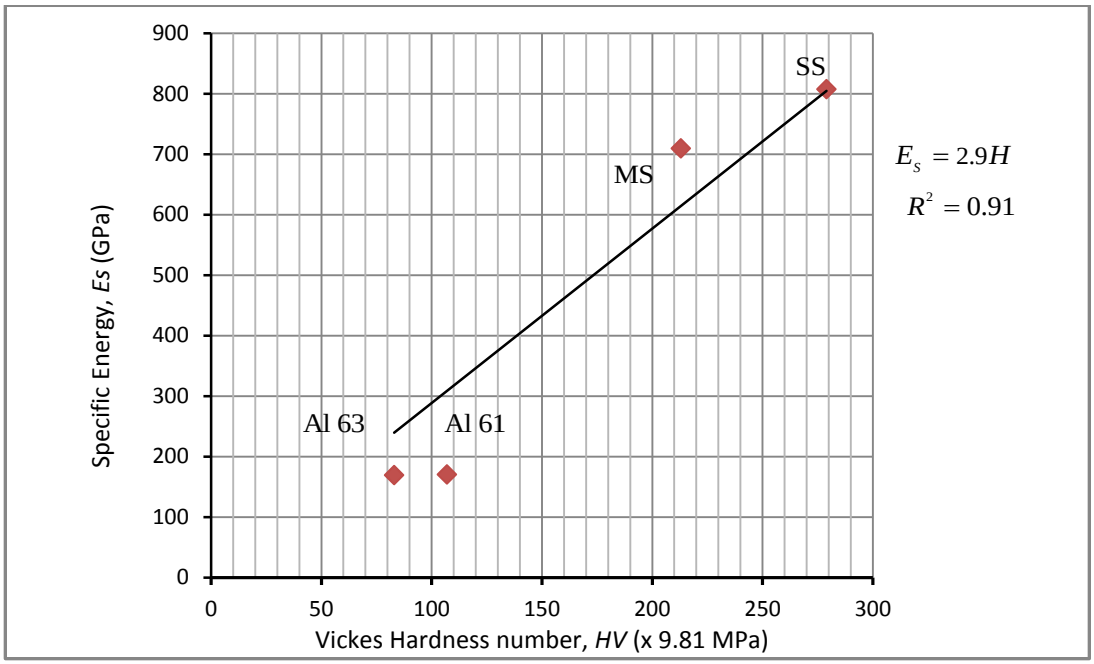

Figure 7-24: Specific energy versus hardness

From the table of critical values for Pearsons' correlation, the critical coefficient (R) at a 95% confidence level is 0.95 with a sample size of 4. In Figure 7-24 the R-value for *Es* and H is 0.95, which is equal to 0.95, meaning there is a 95% confidence considering that

Es is proportional to *H*. This linear relationship is consistent with the equivalent conversion of specific energy unit from J/m^3 or Nm/m^3 to Pa. This equivalence relationship between specific energy and hardness may verify the existence of specific energy.

Even though the relationship between wear and hardness becomes somewhat more complicated when the microstructure of materials like alloys are taken into consideration, the formula *Es=BH* may be expected to estimate the specific energy of other pure metals subjected to the same abrasive conditions. The specific energy coefficient *B* is determined by the abrasive conditions in the form of $(\mu \cdot tan\theta)/2A$. The *B*-value of 2.9 shown in Figure 7-24 is obtained from the abrasive conditions designed in the laboratory to mimic the abrasive wear that occurred on the shovel teeth, such that it is only available for materials which are subjected to this identical abrasive condition. When either the particle characteristics or the contact condition between the particles and material is changed, the specific energy coefficient *B* would need to be calibrated. Again *B* should be evaluated from a group of samples tested in the same abrasive conditions.

7.4.2 Estimation for particle angle range

An alternative method to verify specific energy is to estimate the particle angle range through equation (7-5):

$$\tan\theta = \frac{2A}{\pi\mu} \cdot \frac{E_S}{H} \qquad \textbf{(7-5)}$$

The particle size used in this work was set at 1 mm, and the order of size coefficient *A* was selected in the range of 10^{-2} to 10^{-3} (Table 3-1). 2θ was the angle of the particles (Figure 3-1), and its value depends on the ratio of the specific energy to hardness

(equation (7-5)). If the specific energy does not match the hardness, the particle angle, 2θ, will approach to 180^o (such that specific energy is much higher than hardness) or 0^o (specific energy is much smaller than hardness). In other words the value of 2θ may illustrate the relationship between specific energy and hardness. Table 7-3 shows estimation results of particle angle ranges.

Table 7-3: Estimation results of particle angle range

Material Tested	**Hardness**	**Particle Angle Range, 2θ (Degree)**	
		Min	**Max**
Al63	Very soft	30.9	140.2
Al61	Soft	25.4	132.2
MS	Medium Hard	53.1	157.4
SS	Hard	48.5	154.9

Each material has a different estimate for particle angle range, even though abrasive media tested are the same. This behaviour can be explained with regard to the abrasive mechanism. When contacting with a hard surface, particles are more likely to break and loss their asperities, giving rise to higher angles for hard materials like MS and SS than for soft materials like Al63 and Al61. However hard materials will also prevent penetration of particles, and thus cause these particles to rotate over the material surface rather than slide. The decrease in effective sliding distance finally leads to small particle angles such as for SS to MS or Al61 to Al63. Regardless of a difference on estimation results, all particle angles fell in a rational range from 25.4^o to 157.4^o, verifying that specific energy of each material essentially matches its hardness.

7.4.3 Specific Energy vs. Field Data

One of the most important applications of specific energy is to predict GET performance through the estimation for its life expectancy. Equation (7-6) can be adopted to predict the operating time for GET when specific energy is known.

$$t = \frac{E_S}{\mu F v} V \tag{7-6}$$

V is the maximum volume loss before failure. F, v, and μ are the normal force, velocity, and friction coefficients respectively, and their product (μFv) is the friction power. Time (t) is the total time for the materials under continuous abrasion to failure. The value of specific energy (Es) can be obtained through abrasion tests or evaluated from the formula $Es=BH$ for pure metals.

Based on equation (7-6), for shovel teeth working in oil sands, the prediction for their actual operating hours is expressed as:

$$T = \frac{E_S}{E_C} V \cdot T_C \cdot A' \cdot U \tag{7-7}$$

Where:

Ec	Friction energy per digging cycle per shovel tooth
Tc	Duty cycle time
V	Volume loss of a shovel tooth before its failure
A'	Availability
U	Utilization

According to the field data represented by two failed shovel teeth measured in the laboratory: one medium wear with a volume of loss of 0.0021 m^3 (16.56 kg loss), the

other by severe wear with a volume loss of 0.0046 m^3 (36.34 kg loss). Since mild steel is extensively used to manufacture shovel teeth, the mild steel tested in this thesis was the same as the material used for shovel teeth. The friction coefficient between oil sands and shovel teeth was considered as 0.43 (Table 7-2). Other parameters are seen in Table 7-4.

Table 7-4: Field data

E_C	240 kJ per cycle per shovel tooth
T_C	40 seconds per cycle
A'	0.8
U	0.8
E_S	709 GJ/m^3

Table 7-5: Operation time of a shovel tooth (Unit: Hours)

	Prediction	**Field Record**
Medium Wear	44.3	45
Severe Wear	97.3	96

Table 7-5 shows that a comparison of operating hours between the predicted value and filed records. In terms of medium wear the prediction for shovel tooth is around 44.3 hours, only 0.7 hours less than the actual operating time. In the case of severe wear, the shovel tooth is predicted to work for 97.3 hours, around 1% difference from actual hours. As such the performance of GET subjected to abrasive wear under action by oil sand may be predicted through a specific energy evaluated. This result in turn demonstrates the

existence of specific energy and its rationality. The application of specific energy makes it possible to facilitate selection of materials with regard to specific abrasive conditions.

8 Conclusion

8.1 Conclusion

The goal of this thesis was to study the abrasive wear of shovel teeth to facilitate the prediction of performance for ground engaging tools. In order to achieve this goal a methodology was firstly developed based on geometric analysis of a dipper system to analysis field data, generating normal resistance and digging velocity along the teeth surfaces. The principle of specific energy was defined as a friction energy required to cause a unit volume loss of material make it possible to quantify the abrasion of shovel teeth. A modified rubber wheel abrasion test and an interfacial shear test were designed to measure specific energy of materials. Operating hours for shovel teeth were estimated through specific energy matched field data, suggesting that specific energy was useful to predict GET performance. Summarily, some conclusions through this study on abrasive wear of shovel teeth in oil sands can be reached as follows:

1. Field data can be used to determine normal resistance applied to shovel teeth surface and digging velocities along teeth surface (friction velocity) through a methodology developed via a geometric analysis of a dipper system. Calculations show that the normal resistance increased to a relatively stable level, and then decreased with high fluctuation during the actual excavation process. The friction velocity increased during the dig cycle. Changes on normal resistance or friction velocity confirmed the digging process for shovel teeth from penetration, to cut, and to excavation.

2. $V = \frac{2 \cdot A}{\mu \pi H \cdot \tan \theta} \cdot E$ (equation (3-6)) derived from a typical abrasive model illustrated that abrasion by nature results from the friction energy, making it possible to predict abrasion from the point view of specific energy defined as the energy required to case a unit volume

3. Specific energy can be tested through the combination of a modified rubber wheel abrasion test (MRAT) and an interfacial shear test (IST). MRWAT can mimic the actual abrasive conditions occurring between the shovel teeth and oil sands. IST can be employed to measure the interfacial friction coefficient between the material surface and abrasive media

   The specific energy is independent on the scaling, normal force, and velocity. It is merely determined by particle characteristics, material property, and contact condition in the form of $E_S = \frac{2 \cdot A}{\mu \pi H \cdot \tan \theta}$ (equation (3-7)). Specific energy may be considered as an index quantifying the resistance of a material with hardness *H* to abrasion in a specific abrasive condition characterized by the particle size coefficient (*A*), particle angularity (2θ), and contact condition (μ). However, specific energy is not an inherent property of materials, since it is influenced by abrasive conditions.

4. A linear relationship between specific energy and hardness exists (Figure 7-24), which is consistent with the equivalent conversion of specific energy units from J/m^3 or Nm/m^3 to N/m^2 or Pa. *Es*=*BH* (equation (7-4)) may be used to estimate the specific energy of other pure metals. The specific energy coefficient *B* should

be evaluated from a group of pure metals tested in the same abrasive conditions, and it is only available for other pure metals subjected to this identical abrasive conditions.

5. The operating time predicted via specific energy match the field data represented by two failed shovel teeth measured in laboratory; as such it is possible to facilitate the prediction of performance of ground engaging tools via specific energy.

8.2 Recommendations

Even though in this research, specific energy was tested and employed to predict the performance of shovel teeth, several modifications have to be made as follows:

1. The determination for specific energy coefficient *B* is a major interest to study the relationship between specific energy and material hardness. In current works only four pure metals whose hardness are not over than 300 HV are tested. In the future works, the abrasion tests have to expand to harder materials.

   Additionally, the wear rate is influenced by the microstructure of materials. This research only focuses on pure metals, and the relationship between the specific energy and materials hardness is not yet much clear. In the future works, alloys have to be taken into consideration.

2. Specific energy obtained in current works is only available for the dry abrasive conditions. Since the wet and lubricant environments also have significant

influence on abrasive wear, it is necessary to investigate the specific energy in wet and lubricant abrasive conditions.

3. The principle of specific energy is applicable for all cases of abrasive wear. Current works merely concentrates on the pure abrasive wear caused by fine particles under lower stress with little particle breakage. However in the case of, for example, crusher liners which are subjected to the gouging-impact abrasion under larger contact stress with frequent occurrence of comminution, the specific energy obtained from the rubber wheel abrasion test is unavailable, and new tests have to be designed to determine the specific energy in that wear condition.

9 List of Reference

1. ASTM D5321 Standard Test Method for Determining the Shear Strength of Soil-Geosynthetic and Geosynthetic-Geosynthetic Interfaces by Direct Shear. In *Book of Standards* (Vol. 04.13). ASTM International.
2. ASTM G65-04 Standard Test Method for Measuring Abrasion Resistance Using the Dry Sand/Rubber Wheel Apparatus. In *Book of standards* (Vol. 03.02). ASTM International.
3. ASTM G81 Standard Test Method for Jaw Crusher Gouging Abrasion Test. In *Book of Standards* (Vol. 03.02). ASTM International.
4. Blouin, S. (2001). Review of resistive force models for earthmoving process. *Journal of Aerospace Engineering*, 102-111.
5. Brumund, W. F., & Leonards, G. A. (1973). Experimental study of static and dynamic friction between sand and typical construction materials. *Journal of testing and evaluation, 1*(2), 163-165.
6. Cross, C., & Olson, D. L. (1992). Friction and wear in the mining and mineral industries. In P.J.Blau, *ASM Handbook, Volume 18: Friction, Lubrication, and Wear Technology* (pp. 649-655). ASM International.
7. Darling, P. (2011). *SME mining engineering handbook (3rd edition).* Society for Mining, Metallurgy, and Exploration(SME).
8. Dusseault, M. B., & Morgenstern, R. N. (1978). Shear strength of Athabasca oil sands. *Can Geotech. J.*, 216-238.
9. *ESCO Corporation*. (2013). Retrieved from A&S Machinery Co.,Ltd.: http://www.tradeeasy.com/supplier/663585/products/p1135748/esco-bucket-teeth.html
10. Eyre, T. S. (1976). Wear characteristics of metals. *Tribology international*, 204-212.
11. Frimpong, S. (2005). Mechanics of cable shovel-formation interactions in surface mining excavations. *Journal of Terramechnics, 42*, 15-33.

12. Frimpong, S., & Hu, Y. (2004). Parametric simulation of shovel-oil sands interactions during excavation. *International Journal of Surface Mining, Reclamation, and Environment, 18*(3), 205-219.
13. Frost, J. D., & Han, J. (1999). Behavior of Interfaces Between Fiber-Reinforced Polymers and Sand. *Journal of Geotechnical and Geoenviromental Engineering*, 633-640.
14. Stachowiak, G.B.& Stachowiak, G.W. (2001). The effects of particle characteristics on three-body abrasive wear. *wear*, 201-207.
15. Gate, J. D., & Gore, G. J. (2007). The meaning of high stress abrasion and its applicaiton in white cast irons. *wear*, 6-35.
16. Hawk, J. A. (2000). Abrasive wear testing. In H. Kuhn, & D. Medlin, *ASM Handbook, Volume 8: Mechanical Tesing and Evaluation* (pp. 325-337).
17. Hawk, J. A., & R.D.Wilson. (2000). Chapter 35: Tribology of earthmoving, mining, and minerals processing. In *Modern Tribology Handbook.* CNC Press LLC.
18. Heerema, E. P. (1979). Relationship between wall friction, displacement, velocity, and horizontal stress in clay and in sand,for pile driveability analysis. *Ground Engineering, 12*(9), 55-60.
19. Hemami, A. (1994, October). Motion rajectory study in the scooping operation of an LHD-Loader. *IEEE Transactions on industry application, 30*(5), 1333-1338.
20. Hrebar, M. (1997, Mar). Large wheel loaders vs. cable shovels. *Mining Engineering, 49*(3), 58-64.
21. Joseph, T. G., & Hansen, G. W. (2002, September). Oil sands reacton to cable shovel motion. *CIM Bulletin, 95*(1064), 62-64.
22. Joseph, T. G., & Shi, N. (2011). Simulation of cable shovel and dippers in mining applications. *CIM Journal, 2*(3), 1-8.
23. Joseph, T. G., & Shi, N. (2012). A revised dipper-ground equilibrium derivation for shovels operating in oil, sand, and soft ground. *CIM Journal, 3*(1), 1-7.
24. Kato, K., & Adachi, K. (2000). Chapter 7: Wear mechanisms. In *Modern Tribology Handbook.* CNC Press LLC.

25. Lafleur, J. P. (2011). *A study of abrasion in steel during comminution.* (Msc., McGill University (Canada)). *ProQuest Dissertations and Thesis*.(908921581).
26. Li, Y. D., Elalem, K., Anderson, M. J., & Chiovelli, S. (1999). A microscale dynamical model for wear simulation. *Wear*, 380-386.
27. Llewellyn, R. (1996, July/August). Materials for controlling wear in surface mining. *CIM Bulletin, 89*(1002), 76-82.
28. Llewellyn, R. (1997). Resisting wear attack in oil sands mining and processing. *CIM Bulletin, 89*(1002), 75-82.
29. Llewellyn, R. (1997). Resisting wear attack in oil sands mining and processing. *CIM Bulletin*, 75-82.
30. Marinescu, I. D., W, B. R., Dimitrov, B., & Ohmori, H. (2013). *Tribology of Abrasive Maching Processes.* Waltham: Elsevier.
31. McKee, B. (1997). An overview of wear-resistant alloys for the mining industry. *CIM Bulletin, 90*(1012), 71-74.
32. McKyes, E. (1985). Soil cutting and tillage. *Elsevier*.
33. Misra, A., & Finine, I. (1983). An experimental study of three-body abrasive wear. *wear*, 57-68.
34. Misra, A., & Finnie, I. (1981). Some observation on two-body abrasive wear. *wear*, 41-56.
35. Morgenstern, R. N., & Scott, D. J. (1997). Shear strength of Athabasca Oil Sands. *Geotechnical News, Special Commemorative Edition, 15*(4), 102-109.
36. Murray, S. F. (1988). Wear resistant coatings and surface treatments. In E. R. Booser, *Handbook of lubrications: Theory and Practice of Tribology* (pp. 623-643). CRC Press.
37. Norman, T. (1980). Wear in ore processing machinery. In M. Peterson, & W. Winer, *Wear Control Handbook* (pp. 1009-1051). ASME.
38. Osman, S. M. (1964). The mechanics of soil cutting blades. *Journal of Agriculture Engineering Research*, 313-328.
39. Knights,P.K. (2009). Optimal replacement intervals for shovel dipper teeth. *International Journal of Mining, Reclamation, and Envrionment, 23*(3), 157-167.

40. Patnayak, S., & Tannant, D. D. (2005). Performance monitoring of electric cable shovels. *International Journal of Surface Mining, Reclamation, and Environment, 19*(9), 276-294.
41. Rabinowicz, E. (1980). Wear coefficients - metals. In M. B. Peterson, & W. O. Winer, *Wear Control Handbook* (p. 475). ASME.
42. Ramsey , G., & Homer, R. (2012). *Fundamentals of Tribology.* Imperial College Press.
43. Richardson.R.C. (1968). Wear of metals by relatively soft abrasives. *Wear, 11*, 245-274.
44. Shi, N. (2007). *A new approach to improve cable shovel design for cutting soft rock and soils*.(Ph.D., The University of Alberta (Canada)) *ProQuest Dissertation and Thesis*. (304789980)
45. Singhal, R. (1989, Nov). Canadian surface mining technology. *Mining Magazine, 161*(5).
46. Stephane, B., Ahmad, H., & Mike, L. (2001, July). Review of resistive force modles for earthmoving process. *Journal of Aerospace Engineering*, 102-111.
47. Thakare, M. R., & Wharton, J. A. (2012). Effect of abrasive particle size and the influence of mircrostructure on the mechanisms in wear-resistant materials. *wear*, 16-28.
48. Wyllie, R. J. (1987). World mining congress exhibition provides showcase for mining industry suppliers. *Engineering and mining journal*, 72-85.
49. Yin, Y., Grondin, G. Y., Obaia, K. H., & Elwi, A. E. (2007). Fatigue life prediction of heavy mining equipment. Part 1: Fatigue load and assessment and crack growth rate tests. *Journal of Constructional Steel Research, 63*, 1494-1505.
50. Zelenin, A., Balovnev, V., & Kerov, I. (1985). *Machines for moving the earth* . New Delhi: Amerind Punlishing .
51. Zum, K. H. (1988). Modelling of two-body abrasive wear. *Wear, 124*, 87-103.

Appendices:

Table of Critical Values for Pearson' Correlation Coefficient

Degree of Freedom (N-2)	Proportion in One Tail					
	0.25	0.1	0.5	0.25	0.1	0.05
	Proportion in Two Tails					
	0.05	0.02	0.01	0.5	0.2	0.1
1	0.7071	0.9511	0.9877	0.9969	0.9995	0.9999
2	0.5000	0.8000	0.9000	0.9500	0.9800	0.9900
3	0.404	0.687	0.8054	0.8783	0.9343	0.9587
4	0.3473	0.6084	0.7293	0.8114	0.8822	0.9172
5	0.3091	0.5509	0.6694	0.7545	0.8329	0.8745
6	0.2811	0.5067	0.6215	0.7067	0.7887	0.8343
7	0.2596	0.4716	0.5822	0.6664	0.7498	0.7977
8	0.2423	0.4428	0.5494	0.6319	0.7155	0.7646
9	0.2281	0.4187	0.5214	0.6021	0.6851	0.7348
10	0.2161	0.3981	0.4973	0.576	0.6581	0.7079
11	0.2058	0.3802	0.4762	0.5529	0.6339	0.6835
12	0.1968	0.3646	0.4575	0.5324	0.612	0.6614
13	0.189	0.3507	0.4409	0.514	0.5923	0.6411
14	0.182	0.3383	0.4259	0.4973	0.5742	0.6226
15	0.1757	0.3271	0.4124	0.4821	0.5577	0.6055
16	0.17	0.317	0.4	0.4683	0.5425	0.5897
17	0.1649	0.3077	0.3887	0.4555	0.5285	0.5751
18	0.1602	0.2992	0.3783	0.4438	0.5155	0.5614
19	0.1558	0.2914	0.3687	0.4329	0.5034	0.5487
20	0.1518	0.2841	0.3598	0.4227	0.4921	0.5368
21	0.1481	0.2774	0.3515	0.4132	0.4815	0.5256
22	0.1447	0.2711	0.3438	0.4044	0.4716	0.5151
23	0.1415	0.2653	0.3365	0.3961	0.4622	0.5052
24	0.1384	0.2598	0.3297	0.3882	0.4534	0.4958
25	0.1356	0.2546	0.3233	0.3809	0.4451	0.4869
26	0.133	0.2497	0.3172	0.3739	0.4372	0.4785
27	0.1305	0.2451	0.3115	0.3673	0.4297	0.4705
28	0.1281	0.2407	0.3061	0.361	0.4226	0.4629
29	0.1258	0.2366	0.3009	0.355	0.4158	0.4556
30	0.1237	0.2327	0.296	0.3494	0.4093	0.4487
31	0.1217	0.2289	0.2913	0.344	0.4032	0.4421
32	0.1197	0.2254	0.2869	0.3388	0.3972	0.4357
33	0.1179	0.222	0.2826	0.3338	0.3916	0.4296
34	0.1161	0.2187	0.2785	0.3291	0.3862	0.4238
35	0.1144	0.2156	0.2746	0.3246	0.381	0.4182
36	0.1128	0.2126	0.2709	0.3202	0.376	0.4128
37	0.1113	0.2097	0.2673	0.316	0.3712	0.4076

38	0.1098	0.207	0.2638	0.312	0.3665	0.4026
Degree of Freedom (N-2)	**Proportion in One Tail**					
	0.25	**0.1**	**0.5**	**0.25**	**0.1**	**0.05**
	Proportion in Two Tails					
	0.05	**0.02**	**0.01**	**0.5**	**0.2**	**0.1**
41	0.1057	0.1993	0.2542	0.3008	0.3536	0.3887
42	0.1044	0.197	0.2512	0.2973	0.3496	0.3843
43	0.1032	0.1947	0.2483	0.294	0.3457	0.3801
44	0.102	0.1925	0.2455	0.2907	0.342	0.3761
45	0.1008	0.1903	0.2429	0.2876	0.3384	0.3721
46	0.0997	0.1883	0.2403	0.2845	0.3348	0.3683
47	0.0987	0.1863	0.2377	0.2816	0.3314	0.3646
48	0.0976	0.1843	0.2353	0.2787	0.3281	0.361
49	0.0966	0.1825	0.2329	0.2759	0.3249	0.3575
50	0.0956	0.1806	0.2306	0.2732	0.3218	0.3542